広島大学学位請求論文

Reactivity of Singlet Diradicaloids Embedded in Macrocyclic Skeleton and Non-Aufbau Electronic Configuration of Triplet Diradicals

（マクロ環状骨格を有する一重項ジラジカルの反応性及び三重項ジラジカルの非 Aufbau 電子構造）

２０２２年

広島大学大学院理学研究科
化学専攻

WANG Zhe（王　哲）

目　次

１．主論文

Reactivity of Singlet Diradicaloids Embedded in Macrocyclic Skeleton and Non-Aufbau Electronic Configuration of Triplet Diradicals
（マクロ環状骨格を有する一重項ジラジカルの反応性及び三重項ジラジカルの非 Aufbau 電子構造）
WANG Zhe（王　哲）

２．公表論文

(1) Impact of the macrocyclic structure and dynamic solvent effect on the reactivity of a localised singlet diradicaloid with π-single bonding character.
WANG Zhe, AKISAKA Rikuo, YABUMOTO Sohshi, NAKAGAWA Tatsuo, HATANO Sayaka and ABE Manabu.
Chemical Science, 12(2) (2021) 613–625.

(2) SOMO–HOMO Conversion in Triplet Cyclopentane-1,3-diyl Diradicals.
WANG Zhe, MURATA Ryo and ABE Manabu.
ACS Omega, 6(35) (2021) 22773–22779.

３．参考論文

(1) Extremely Long Lived Localized Singlet Diradicals in a Macrocyclic Structure: A Case Study on the Stretch Effect.
HARADA Yuta, WANG Zhe, KUMASHIRO Shunsuke, HATANO Sayaka and ABE Manabu.
Chemistry – A European Journal, 24(55) (2018) 14808–14815.

(2) 1,3-Diradicals Embedded in Curved Paraphenylene Units: Singlet versus Triplet State and In-plane Aromaticity.

MIYAZAWA Yuki, WANG Zhe, MATSUMOTO Misaki, HATANO Sayaka, ANTOL Ivana, KAYAHARA Eiichi, YAMAGO Shigeru and ABE Manabu.
Journal of the American Chemical Society, 143(19) (2021) 7426–7439.

(3) SOMO–HOMO Conversion in Triplet Carbenes.
MURATA Ryo, WANG Zhe, MIYAZAWA Yuki, ANTOL Ivana, YAMAGO Shigeru and ABE Manabu.
Organic Letters, 23(13) (2021) 4955–4959.

(4) Long-lived localised singlet diradicaloids with carbon–carbon π-single bonding (C–π–C).
WANG Zhe, YADAV Pinky and ABE Manabu.
Chemical Communications, 57(86) (2021) 11301–11309.

(5) Singly Occupied Molecular Orbital–Highest Occupied Molecular Orbital (SOMO–HOMO) Conversion.
MURATA Ryo, WANG Zhe and ABE Manabu.
Australian Journal of Chemistry, 74(12) (2021) 827–837.

(6) New Insights into Bond Homolysis Process and Discovery of Novel Bonding System (C–π–C) by Generating Long-lived Singlet Diradicals.
ABE Manabu, WANG Zhe and AKISAKA Rikuo.
AsiaChem, 2(1) (2021) 32–41.

(7) Impacts of Solvent and Alkyl Chain Length on the Lifetime of Singlet Cyclopentane-1,3-diyl Diradicaloids with π-Single Bonding.
LIU Qian, WANG Zhe and ABE Manabu.
The Journal of Organic Chemistry, 87(3) (2022) 1858–1866.

主論文

Hiroshima University Doctoral Thesis

Reactivity of Singlet Diradicaloids Embedded in Macrocyclic Skeleton and Non-Aufbau Electronic Configuration of Triplet Diradicals

2022

Department of Chemistry,
Graduate School of Science,
Hiroshima University

WANG Zhe

Table of Contents

Chapter 1.

General Introduction

1.1 Open-Shell Species

Open-shell species such as radicals, diradicals, and multi-radicals have unpaired electron(s) on the outer atom/molecular orbital(s) (Figure 1.1b). The open-shell species are generally more active than the closed-shell species, in which all orbitals are fully occupied by the paired two electrons (Figure 1.1a). The open-shell species are important intermediate during bond-formation and bond-breaking processes. Investigation of their chemistry will provide a deeper understanding of the chemical reactions and develop new synthetic methods using radical species.[1–9]

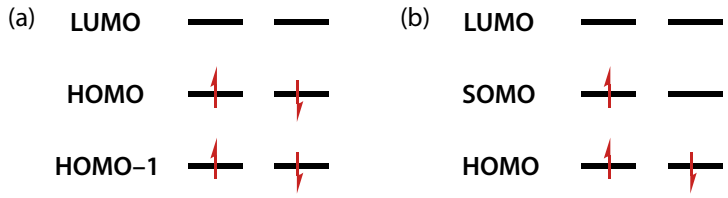

Figure 1.1 Electronic configuration of (a) closed-shell species and (b) open-shell radicals. HOMO: highest occupied molecular orbital; LUMO: lowest unoccupied molecular orbital; SOMO: singly occupied molecular orbital.

1.2 Bond Cleavage

The bond cleavage process of a single covalent bond includes heterolysis and homolysis (Figure 1.2a). The charged species (*i.e.*, cation, anion, or zwitterion) are generated during heterolysis of a neutral molecule, where the generated anion takes both original bonding electrons. On the other hand, the homolytic bond-breaking separates two bonding electrons equally and generates neutral radical species from a neutral molecule. Radicals with one unpaired electron have a doublet state of spin multiplicity, and they could be observed by electron paramagnetic resonance (EPR) measurements (Figure 1.2b).[3]

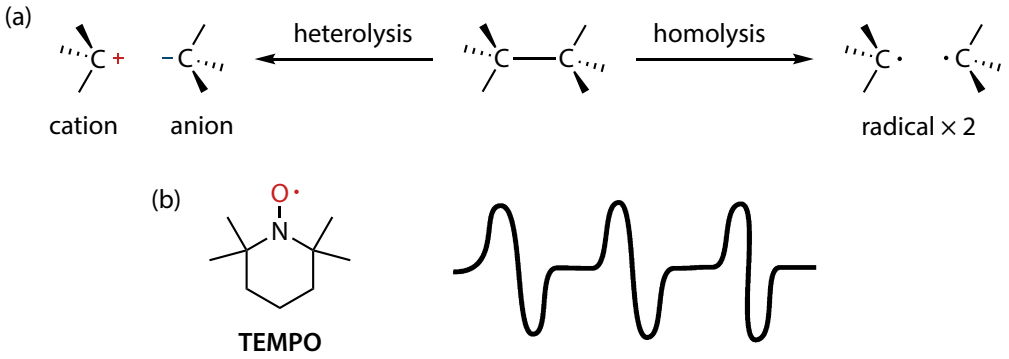

Figure 1.2 (a) Heterolysis and homolysis of C–C single bond. (b) Chemical structure of TEMPO radical and its EPR pattern.

If the homolytic bond-breaking happens in cyclic molecules, the generated species have two unpaired electrons in the same fragment (Figure 1.3a). If a long spacer separates two electrons with sufficient distance, so-called "*biradicals*", the distance-dependent electron exchange interaction (J) close to 0, the EPR spectra of biradicals are similar to those of a pair of radicals (Figure 1.3b).[3] On the other hand, when the electron exchange interaction is large enough ($J > 0$), a significant interaction between two electrons gives singlet (1↓) and triplet (1↑) spin multiplicity of "*diradicals*" according to the spin directions of two electrons. The triplet diradicals are usually stable and long-lived. Due to the ferromagnetic coupling of two electrons, they show great potential in application to magnetic materials, and they could be recorded by EPR spectrometer (Figure 1.3c).[3] On the other hand, singlet diradicals are EPR-silence because the magnetic quantum number (m_s) is zero.

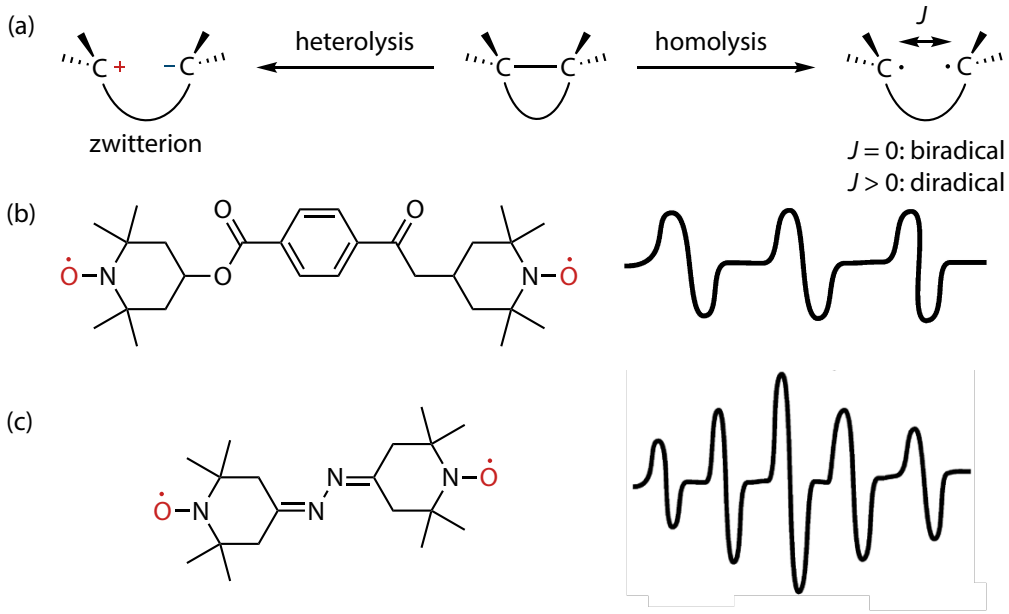

Figure 1.3 (a) Heterolysis and homolysis of C–C single bond in cyclic molecules. Chemical structures and EPR pattern of (b) bis(nitroxide) biradical ($J \approx 0$) and (c) triplet bis(nitroxide) diradical ($J > 0$).

The bond-cleavage process is described as the decrease in the HOMO–LUMO energy gap. In the stable bonding region in Figure 1.4, the HOMO–LUMO gap is significant for the closed-shell species, and the diradical character (y_0) equals zero. The diradical character y_0 is defined by the

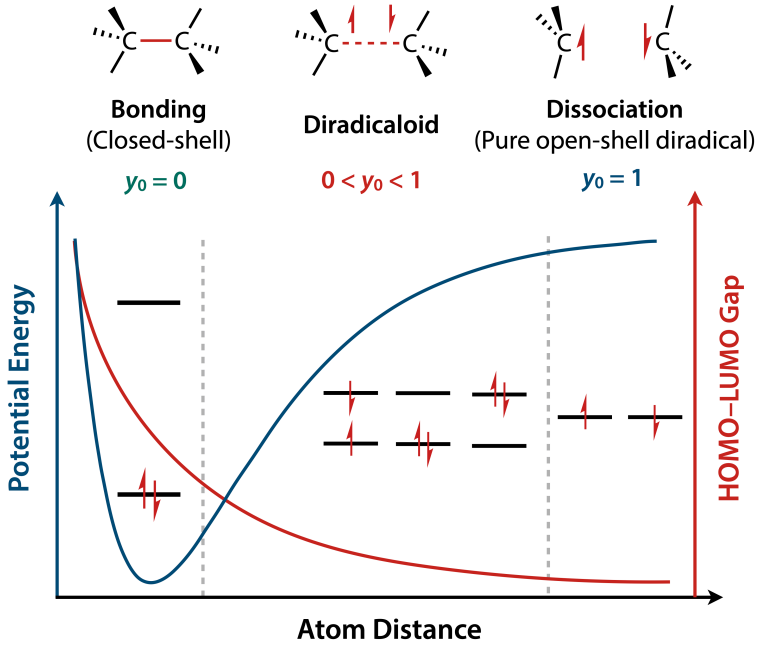

Figure 1.4 Bond dissociation process of a C–C bond, where the variations of the HOMO and LUMO level are shown as a function of atom distance.

occupation number of LUMO (n_{LUMO}). Thus, the value '$1 - y_0$' indicates an effective bond order.[10] When the atom distance is long enough, a pure open-shell diradical is assigned by the diradical character $y_0 = 1$. The term "*diradicaloids*" is defined in the $0 < y_0 < 1$ region, indicating the singlet diradicals with closed-shell characters.

1.3 References

1 *Reactive Intermediate Chemistry*, ed. R. A. Moss, M. S. Platz and M. Jones Jr., John Wiley & Sons, Hoboken, **2004**.

2 *Reviews of Reactive Intermediate Chemistry*, ed. M. S. Platz, R. A. Moss and M. Jones Jr., John Wiley & Sons, Hoboken, **2007**.

3 M. Abe, Diradicals, *Chem*. *Rev*., **2013**, *113*, 7011–7088.

4 T. Stuyver, B. Chen, T. Zeng, P. Geerlings, F. De Proft and R. Hoffmann, Do diradicals behave like radicals?, *Chem. Rev.*, **2019**, *119*, 11291–11351.

5 T. S. Chambers and G. B. Kistiakowsky, Kinetics of the thermal isomerization of cyclopropane, *J. Am. Chem. Soc.*, **1934**, *56*, 399–405.

6 J. A. Berson, L. D. Pedersen and B. K. Carpenter, Thermal stereomutation of cyclopropanes, *J. Am. Chem. Soc.*, **1976**, *98*, 122–143.

7 L. Salem and C. Rowland, The electronic properties of diradicals, *Angew. Chem. Int. Ed.*, **1972**, *11*, 92–111.

8 *Diradicals*, ed. W. T. Borden, Wiley Interscience Publication, New York, **1982**.

9 R. Hoffmann, Trimethylene and the addition of methylene to ethylene, *J. Am. Chem. Soc.*, **1968**, *90*, 1475–1485.

10 M. Nakano, Electronic structure of open-shell singlet molecules: diradical character viewpoint, *Top. Curr. Chem.*, **2017**, *357*, 47.

Chapter 2.

Reactivity of Singlet Diradicaloid Embedded in Macrocyclic Skeleton

2.1 Chapter Introduction

2.1.1 Carbon–Carbon π-Single Bond (C–π–C)

Chemical reactivity is always associated with the highest occupied molecular orbital (HOMO) and lowest unoccupied molecular orbital (LUMO).[1] The σ-bond and π-bond are very fundamental concepts in organic chemistry. Generally, σ-bonding systems display a large energy gap between bonding and anti-bonding molecular orbital (Figure 2.1a), while a π-bond provides a smaller energy gap due to the weaker coupling of two atomic orbitals than that in σ-bonding systems (Figure 2.1b). Therefore, as in ethylene molecule, a π-bond usually conjugates with a lower lying σ-bond in multi-bonding systems.

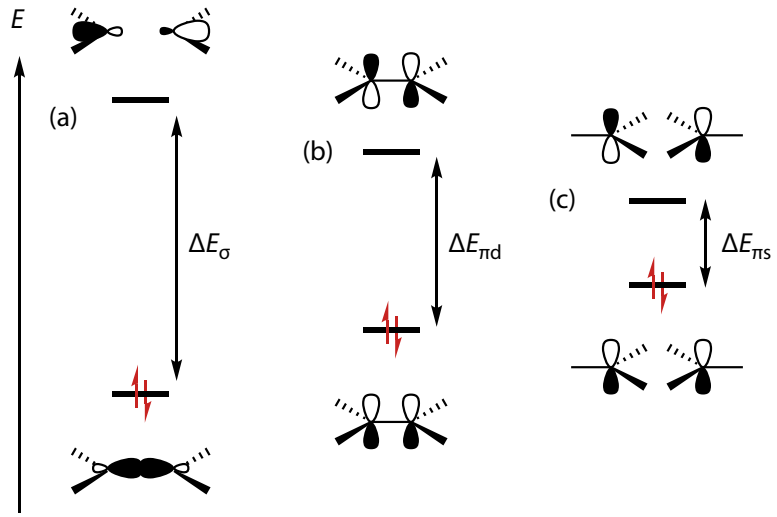

Figure 2.1 Bonding and anti-bonding energy gaps (ΔE) of (a) σ-bonding, (b) π-bonding with a low-lying σ-bonding and (c) π-single bonding systems.

Several singlet diradicaloids containing heteroatoms or metallic atoms with bonding character in the HOMO were reported in the past two decades.[2–4] Although some of these species show considerable diradical reactivity, the π-single bonding character is possessed in these species

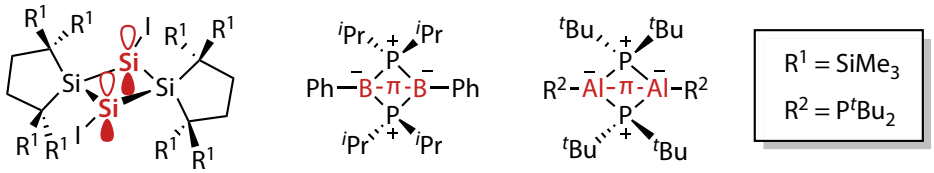

Scheme 2.1 Reported species with π-single bonding.

(Scheme 2.1). If carbon–carbon π-single bond (C–π–C without low lying σ-bond) is possible, they are expected to show an extremely small HOMO–LUMO gap, providing high redox activity and new optical properties from the unique electronic character (Figure 2.1c).[1]

2.1.2 Spin-Control of Cyclopentane-1,3-Diyl Diradicals

The cyclopentane-1,3-diyl diradicals are considered excellent candidates for carbon-based π-single bonding species due to the increased strain energy during the formation of σ-bonded bicyclic products bicyclo[2.1.0]pentane. Thus, the stabilization energy of cyclopentane-1,3-diyl diradicals decreased by the formation of σ-bond, compared with that of propane-1,3-diyl diradicals (Figure 2.2).[5,6]

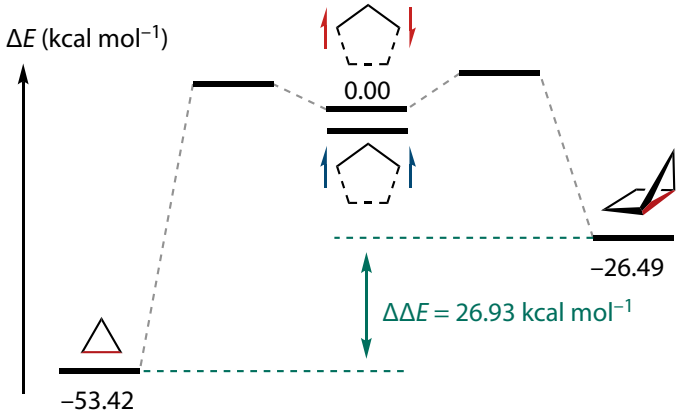

Figure 2.2 Energy profile for the σ-bond-formation processes of singlet propane-1,3-diyl diradical (left) and singlet cyclopentane-1,3-diyl diradical (right), calculated at CASSCF(2,2)/6-31G(d) level of theory.

Although singlet ground states are necessary for creating π-single bonded species, the ground state spin preferences of propane/cyclopentane-1,3-diyl diradicals are triplet. In the period of 1998–2000, the ground state spin-control of cyclopentane-1,3-diyl diradicals was reported by the substituents effect at the C2 carbon atom.[7–9] The ground state spin preference is determined by the balance between through-space (TS) interaction and through-bond (TB) interaction. The through-space interactions between two p orbitals at C1 and C3 carbon generate two non-bonding molecular orbitals, symmetric ψ_{TS}^{+}, and asymmetric ψ_{TS}^{-} (Figure 2.3).

If electron donating groups (EDG) are attached at the C2 position, the through-bond interaction between ψ_{TS}^{+} and σ_{CX} destabilizes the LUMO

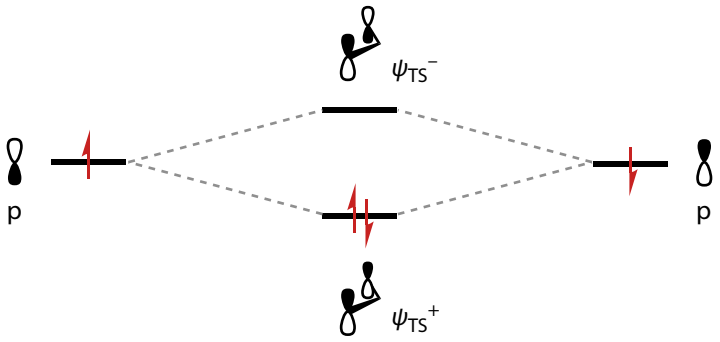

Figure 2.3 Through-space interaction between two p orbitals.

(ψ_{TB}^{-}) but makes no change to the energy of ψ_{TS}^{-}. Thus, the most stable electronic configuration depends on the energy gap between ψ_{TB}^{-} and ψ_{TS}^{-}: if X is hydrogen or alkyl groups, the HOMO–LUMO gap is small, resulting in a triplet ground state; if X is silyl groups, the singlet is more stable, but this kind of singlet diradicals do not process π-single bonding due to the antibonding character in the ψ_{TS}^{-}, which is the HOMO of these type-II singlet diradicals (Figure 2.4).

On the other hand, if X is an electron withdrawing group (EWG) like fluoro or alkoxyl, the through-bond interaction between ψ_{TS}^{+} and σ_{CX}^{*} stabilize the HOMO (ψ_{TB}^{+}) and make a singlet ground state (Figure 2.4). Since the HOMO orbitals show bonding character, these diradicaloids should have π-single bonding character in the singlet ground states.

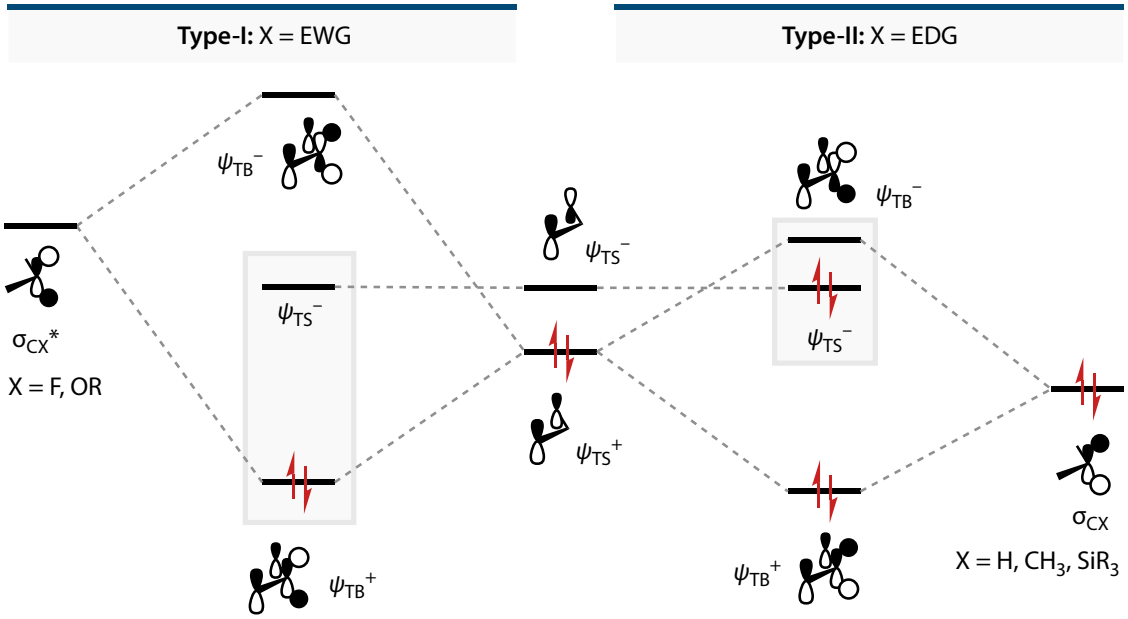

Figure 2.4 Effect of through-bond interaction on the relative energy level of non-bonding molecular orbitals.

2.1.3 Stabilization of Singlet Cyclopentane-1,3-Diyl Diradicaloids

Several approaches were conducted to make longer-lived singlet diradicaloids. Two methods are widely used to stabilize highly reactive species: thermodynamic stabilization and kinetic stabilization.

Thermodynamic stabilization decreases the energy levels of reactive species but makes negligible changes in the energies of transition states and degradation products (Figure 2.5a). The thermodynamic stabilization of cyclopentane-1,3-diyl diradicaloids was reported by introducing phenyl rings to the radical carbon atoms, and the unpaired electrons were stabilized by delocalization (Figure 2.5b).[10,11] Introducing nitrogen atoms at 4,5 positions of the cyclopentane ring also thermodynamically stabilized the singlet diradicaloids by increasing the resonance strcuture (Figure 2.5c).[12–14]

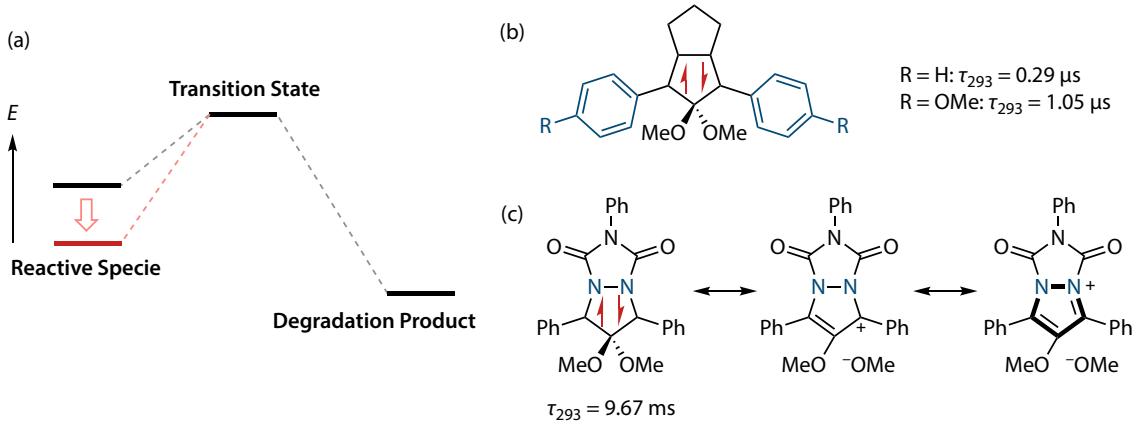

Figure 2.5 (a) Concept of thermodynamic stabilization of reactive species. Reported thermodynamically stabilized singlet diradicaloids by (b) electronic delocalization and (c) nitrogen atom effect.

On the other hand, the kinetic stabilization of reactive species does not affect the electronic configuration but destabilizes the transition states and degradation products (Figure 2.6a). As a result, the degradation reaction is inhibited due to an enormous energy barrier and smaller stabilization energy. By introducing bulky groups at 1,3-diphenyl rings and/or the C2 position, the transition states and σ-bonded products were destabilized due to the steric hindrance between the bulky groups (Figure 2.6b). A long-lived singlet diradicaloids using steric effect was investigated, and its lifetime increased to 23.8 μs at 293 K in benzene solution.[15]

In 2012, the stretch effect was proposed as a kinetic stabilization approach by our laboratory.[16] Normally, the singlet diradicaloids have high

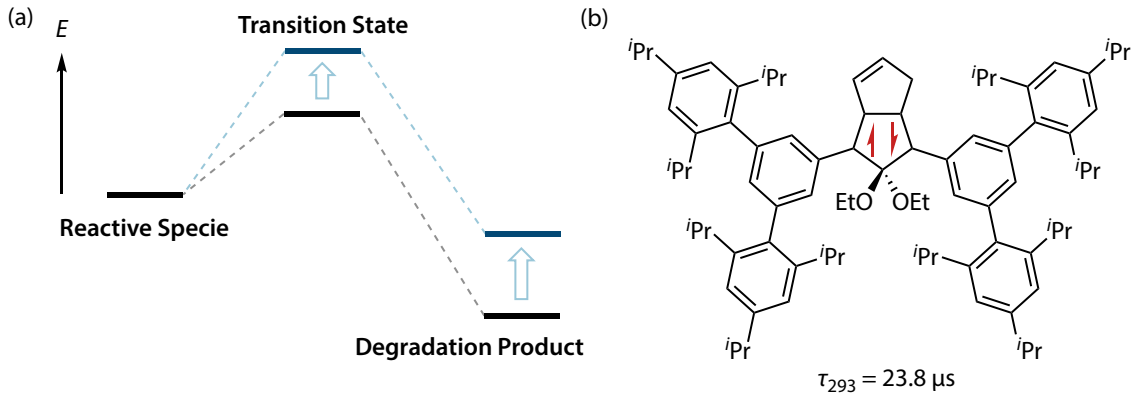

Figure 2.6 (a) Concept of kinetic stabilization. (b) Reported kinetically stabilized singlet diradicaloid using steric effect.

reactivity due to the small energy barrier and considerable stabilization energy in the formation of σ-bond. However, the stretch effect using a macrocyclic skeleton could suppress the σ-bond-formation process by pulling two radical carbon atoms in the opposite direction against σ-bond-formation (Figure 2.7). Therefore, the transition states (**TS**) and ring-closed products (**CP**, *i.e.*, σ-bonded products) are destabilized, and singlet diradicaloids (S-**DR**) could get kinetic stabilization.

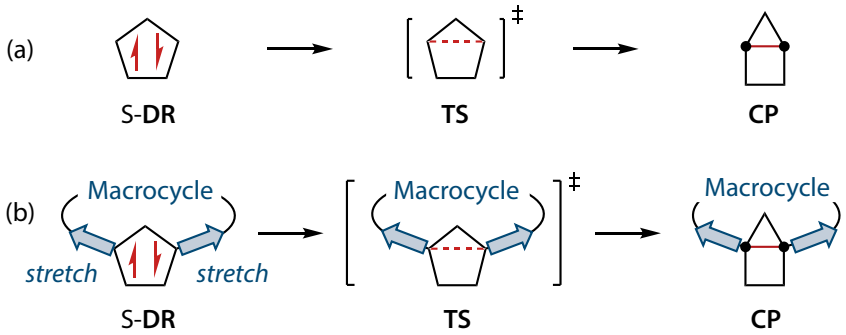

Figure 2.7 (a) Ring-closing process of singlet diradicaloids S-**DR** to ring-closed products **CP**. (b) Stretch effect induced by macrocyclic skeleton.

The first case study of stretch effect was reported in 2018 by our laboratory.[17] A macrocyclic skeleton with alteration of phenyl rings and triple bonds was designed. The lifetimes of singlet diradicaloids S-**DR2a** and S-**DR2b** embedded in macrocyclic skeleton increased to 14.0 and 14.2 μs at 293 K in benzene, which was 70 times longer than that of a non-cyclic parent singlet diradicaloid S-**DR1** (Scheme 2.2). In S-**DR2b**, octyl chains were attached to ensure sufficient solubility. The identical lifetimes of the two

species indicate that the long alkyl chains at macrocyclic skeleton do not affect the reactivity of singlet diradicals.

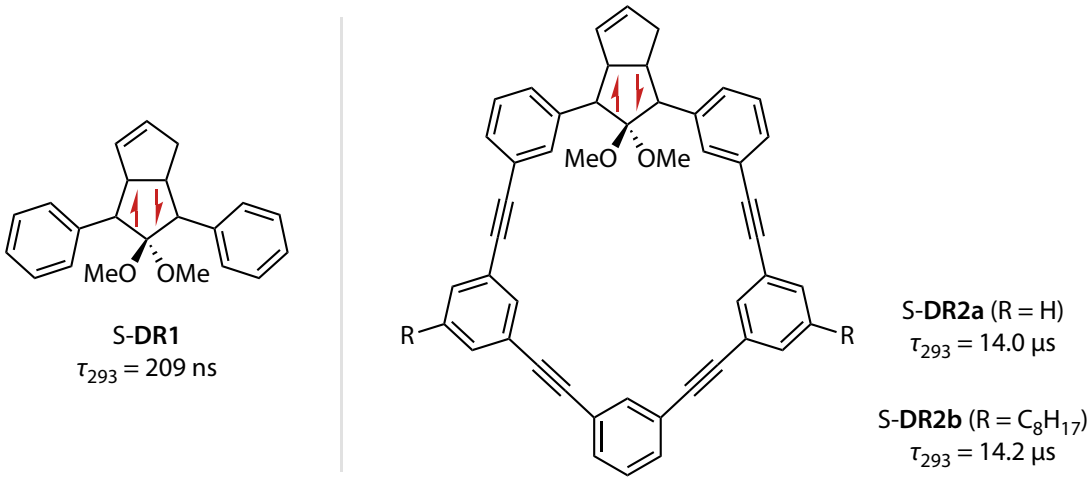

Scheme 2.2 Chemical structures of S-**DR1**, S-**DR2a** and S-**DR2b** and their lifetimes at 293 K in benzene solution at 293 K.

2.2 Results and Discussion

2.2.1 Molecular Design

As discussed in *Section* 2.1, the stretch effect of singlet diradicaloids S-**DR2a**/**b** were fully investigated by computational and experimental studies.[17] This finding inspired us to design a new singlet diradicaloid with a fine-tuned macrocyclic skeleton which shows a more substantial stretch effect by reducing the ring size of macrocycle. Thus, we replaced the 1,3-diethynylphenyl moiety with a naphthyl unit, and the ring size was reduced to 24 atoms of the inner ring of S-**DR2c**/**d** from 26 atoms of S-**DR2a**/**b** (Scheme 2.3).

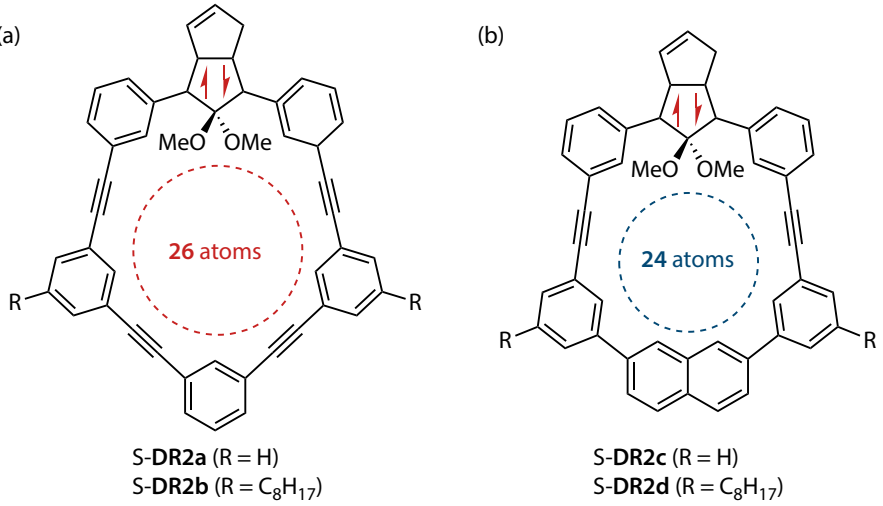

Scheme 2.3 Chemical structures of (a) S-**DR2a**/**b** and (b) S-**DR2c**/**d**.

The stretch effect in the newly designed macrocyclic structure was confirmed by theoretical computations at the (R/U)ωB97X-D/6-31G(d)[18–20] level of theory conducted with *Gaussian 16* program package[21]. All real vibrational frequencies confirmed all the geometries at local minimum points. For singlet diradicaloids, broken-symmetry[22] (BS) approach was applied, and $<S^2>$ values were used to confirm the spin contamination for the open-shell spin-polarized singlet states, whereas the triplet states of diradicals were accessed with unrestricted (U) method.

The singlet ground state of diradicaloid S-**DR2c** was confirmed by computing the singlet-triplet energy gap ($\Delta E_{S-T} = -7.49$ kJ mol^{-1}), which was identical to those of S-**DR1** and S-**DR2a** ($\Delta E_{S-T} = -7.68$ and -7.58 kJ mol^{-1}, Table 2.1), indicating that the macrocyclic skeletons do not affect the singlet-

triplet energy gaps and ground state spin multiplicities. To evaluate the kinetic stabilizations by stretch effect, the thermodynamic stabilizations of singlet cyclopentane-1,3-diyl diradicaloids S-**DR1** and S-**DR2c** derived from delocalization of radical electrons to adjacent phenyl units should be the same. The reaction enthalpy ($\Delta_r H$) of an isodesmotic reaction was calculated to be 1.45 kJ mol^{-1} at the (R/U)ωB97X-D/6-31G(d) level of theory, indicating that the macrocyclic skeleton in S-**DR2c** with the *meta*-connection of the phenyl rings has a negligible influence compared with non-cyclic S-**DR1** (Scheme 2.4). A similar conclusion was also confirmed by the molecular orbital distributions of HOMO and LUMO and the spin densities in S-**DR1** and S-**DR2c** (Figure 2.8). In both cases, the delocalization of radical electrons were limited to the 1,3-diphenyl unit without further delocalization to the macrocyclic skeleton.

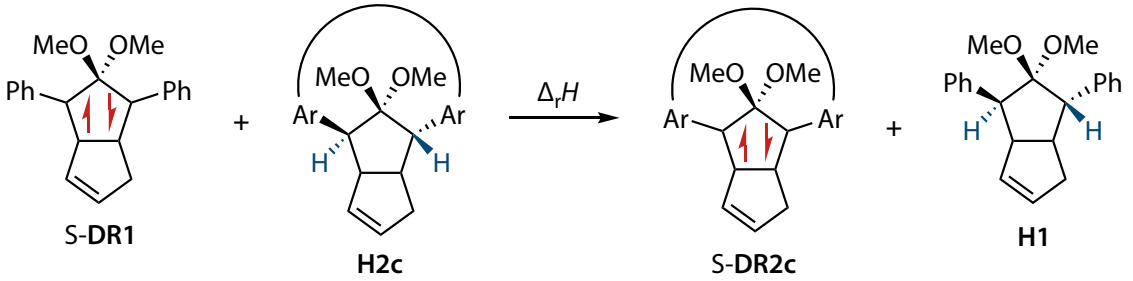

Scheme 2.4 Isodesmotic reaction for estimating thermodynamic stabilization. The *trans* isomers of **H2c** and **H1** are more stable than those *cis* isomers. "Ar—Ar" indicates the macrocyclic skeleton.

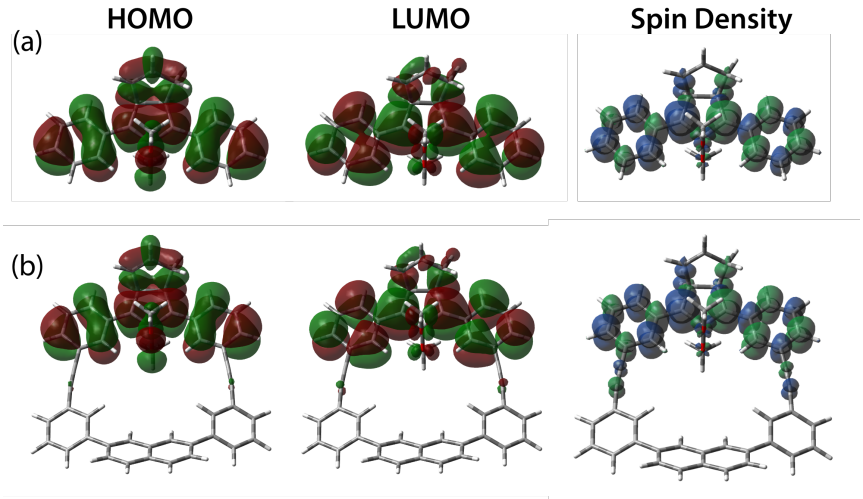

Figure 2.8 HOMO and LUMO distributions and spin density maps for (a) S-**DR1** and (b) S-**DR2c** calculated at (U)ωB97X-D/6-31G(d) level of theory.

The π-single bonding character (*i.e.*, the diradical character y_0) of S-**DR2c** was compared to that of S-**DR1** by calculating the occupation numbers (n) of HOMO and LUMO orbitals at the CASSCF(2,2)/6-31G(d)[23] level of theory. The moderate occupation numbers in S-**DR1** (n_{HOMO} = 1.37, n_{LUMO} = 0.63) and S-**DR2c** (n_{HOMO} = 1.24, n_{LUMO} = 0.76) indicated that both two singlet diradicaloids show moderate π-single bonding character in their singlet ground state.[10]

The transition states **TS** for the ring-closing processes were assessed by computing the imaginary vibrational frequency and intrinsic reaction coordinate (IRC) path. The IRC paths of transition states showed that the bond formation process of singlet diradicaloid towards a metastable ring-closed conformer *par*-**CP** with a face-to-face orientation of the two phenyl rings at 1,3-position (Figure 2.9a). Then, the *par*-**CP** affords the more stable conformer *twi*-**CP** with a nearly perpendicular orientation of two phenyl rings through a barrierless isomerization (Figure 2.9b). On the other hand, the relative position of cyclopentene ring and cyclopropane ring generates *cis*- and *trans*- isomers of **CP**. Thus, 4 conformers of ring-closed products, *cis-par*-**CP**, *cis-twi*-**CP**, *trans-par*-**CP**, and *trans-twi*-**CP** were identified by computations. According to the computational results, the *cis*-**CP** formation was kinetically favored due to a smaller energy barrier, while the *trans*-**CP** was the thermodynamically favored σ-bonded product. Ring-closed products **CP** were calculated with the restricted method, and frequency analyses of optimized geometries showed no imaginary vibrational frequency at these minimal points.

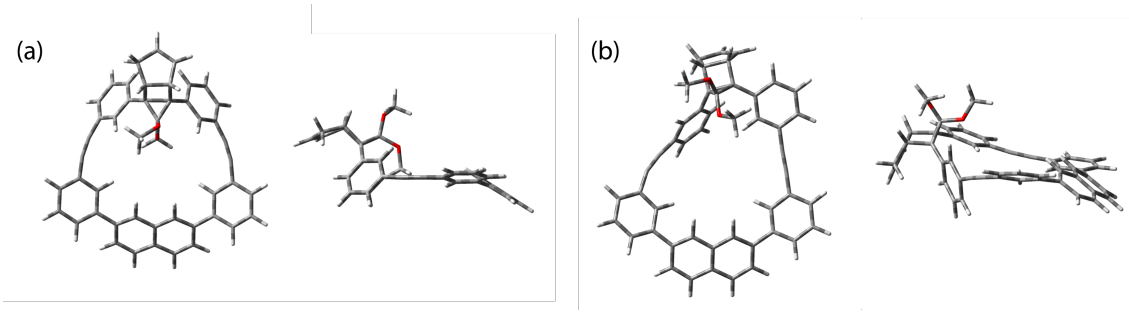

Figure 2.9 Top view and side view of (a) *trans-par*-**CP2c** and (b) *trans-twi*-**CP2c**. Geometries were optimized at (R)ωB97X-D/6-31G(d) level of theory.

The stretch effect in S-**DR2c** was well proved by computations (Figure 2.10). The strained structures of macrocyclic skeleton destabilized the *cis-twi*-**CP2c** and *trans-twi*-**CP2c** ($\Delta\Delta H_{\mathbf{DR-CP}}$) by 35.15 and 37.00 kJ mol^{-1},

respectively, compared with those of non-cyclic *cis-twi*-**CP1** and *trans-twi*-**CP1**. Surprisingly, the energy difference between S-**DR2c** and *cis-twi*-**CP2c** decreased to 3.99 kJ mol^{-1}, suggesting that the significant kinetic stabilization by macrocyclic skeleton of S-**DR2c**. The energy barriers of *cis*- and *trans*-configured ring-closing reactions also increased by 5.91 and 8.60 kJ mol^{-1}, respectively. The kinetic stabilization of S-**DR2c** was strongly enhanced compared with S-**DR2a** by a smaller macrocyclic ring since the **TS2c** and **CP2c** were more labile than the corresponding **TS2a** and **CP2a**. Furthermore, the C1–C3 bond lengths in **CP2c** were slightly elongated compared with those in **CP1**. These effects were most significant in the *par*-**CP2c** (Table 2.1, entries 1–3). The computational results indicated that the macrocyclic skeleton of S-**DR2c** could provide a longer-lived singlet diradicaloid than S-**DR2a/b**.

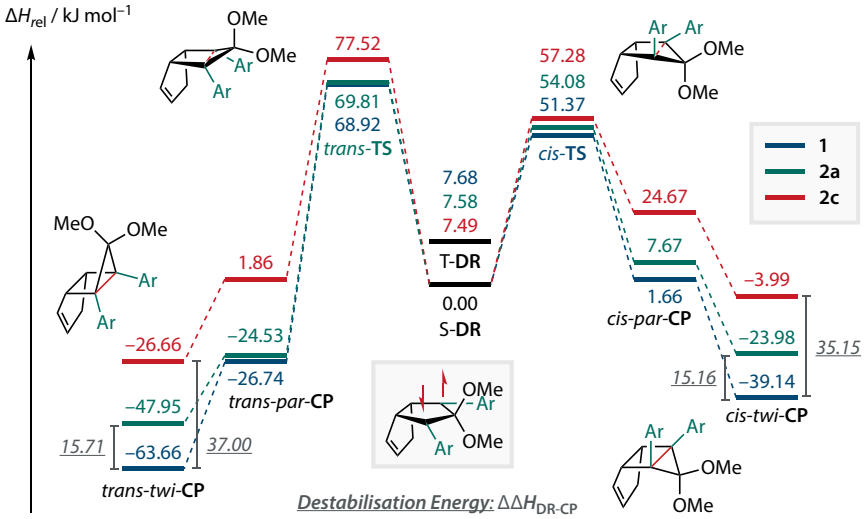

Figure 2.10 Computed energy profiles of the ring-closing reaction of S-**DR1**, S-**DR2a** and S-**DR2c** at (R/U)ωB97X-D/6-31G(d) level of theory.

Similar computations were conducted using different density functionals, including B3LYP,[24] CAM-B3LYP,[25] M06-2X,[26] ωB97[27], and APF-D[28] with 6-31G(d) basis set to check the DFT functionals dependency (Table 2.1). Although the absolute energy values were different, the stretch effect in S-**DR2c** was confirmed by all functionals. The optimized structure of azoalkane **AZ2c**, which is the precursor for singlet diradicaloid S-**DR2c**, was also computed. The computed geometric parameters at (R)ωB97X-D/6-31G(d) level of theory showed the best reproduction of experimental values obtained from X-ray single crystal analysis, so the ωB97X-D functional was used for further computational studies.

Table 2.1 Computational ΔH_{rel} (in kJ mol^{-1}) and [C_1-C_3 distance (in Å)] of the ring-closing reaction of S-**DR1**, S-**DR2a** and S-**DR2c**.

Entry	Functions		S-**DR**	T-**DR**	*cis*-**TS**	*cis-par*-**CP**	*cis-twi*-**CP**	*trans*-**TS**	*trans-par*-**CP**	*trans-twi*-**CP**
1		**1**	0.00	7.68	51.37	1.66 [1.594]	−39.14 [1.585]	68.92	−26.74 [1.576]	−63.66 [1.566]
2	ωB97X-D	**2a**	0.00	7.58	54.08	7.67 [1.600]	−23.98 [1.584]	69.81	−24.53 [1.574]	−47.95 [1.565]
3		**2c**	0.00	7.49	57.28	24.67 [1.622]	−3.99 [1.590]	77.52	1.86 [1.587]	−26.66 [1.567]
4		**1**	0.00	9.43	44.23	24.99 [1.612]	−16.66 [1.608]	65.41	1.48 [1.589]	−37.88 [1.582]
5	B3LYP	**2a**	0.00	9.10	50.35	29.48 [1.630]	−0.30 [1.610]	66.58	1.82 [1.592]	−20.06 [1.583]
6		**2c**	0.00	9.08	55.29	53.25 [1.681]	17.56 [1.623]	76.21	36.81 [1.614]	8.83 [1.585]
7		**1**	0.00	7.22	56.88	17.51 [1.592]	−25.96 [1.586]	76.37	−7.62 [1.572]	−48.20 [1.566]
8	CAM-B3LYP	**2a**	0.00	7.00	61.82	20.99 [1.601]	−9.47 [1.587]	77.38	−8.72 [1.574]	−30.93 [1.566]
9		**2c**	0.00	6.98	66.45	46.07 [1.631]	9.49 [1.596]	84.55	26.08 [1.591]	−10.52 [1.570]
10		**1**	0.00	7.93	40.22	−14.71 [1.590]	−59.63 [1.582]	56.30	−42.02 [1.576]	−81.38 [1.563]
11	M06-2X	**2a**	0.00	7.70	42.08	−8.75 [1.597]	−43.69 [1.581]	58.27	−40.17 [1.572]	−65.51 [1.562]
12		**2c**	0.00	7.72	45.00	6.95 [1.620]	−23.53 [1.588]	68.41	−14.36 [1.583]	−30.43 [1.564]
13		**1**	0.00	6.25	62.27	−6.21 [1.576]	−49.45 [1.569]	80.40	−33.52 [1.560]	−73.87 [1.555]
14	ωB97	**2a**	0.00	6.20	67.11	−1.36 [1.581]	−33.51 [1.570]	81.94	−33.54 [1.562]	−56.65 [1.554]
15		**2c**	0.00	6.13	71.62	21.30 [1.598]	−13.57 [1.575]	87.36	−2.49 [1.572]	−36.07 [1.557]
16		**1**	0.00	8.95	40.57	5.00 [1.593]	−37.86 [1.588]	60.70	−20.17 [1.576]	−59.76 [1.568]
17	APF-D	**2a**	0.00	8.67	42.66	11.92 [1.601]	−23.08 [1.586]	60.33	−19.09 [1.575]	−45.06 [1.566]
18		**2c**	0.00	8.70	45.19	26.61 [1.627]	−3.09 [1.591]	69.16	7.02 [1.587]	−24.57 [1.567]

The stretch effect derived from the molecular strain of the bent structure of macrocyclic skeleton. To get a deeper understanding of the molecular strain, the optimized geometries of S-**DR2c** and **CP2c** were compared. The triple bonds in S-**DR2c** were slightly bent to 173.8–177.9°, while in the *trans-twi*-**CP2c**, the most bent triple bond had a bond angle of 161.1° (Figure 2.11). Also, the naphthyl moiety deviated from the planar structure by 2.42° in S-**DR2c** and up to 5.55° in *trans-twi*-**CP2c**. A similar bent structure was also confirmed in *cis-twi*-**CP2c**. According to the previous report, the bending of a triple bond by 5, 10, 15, and 20° produce 2, 8, 18, and 33 kJ mol^{-1} of strain energy, respectively.[17] Thus, bending the triple bonds and naphthyl moiety provide greater destabilization on **CP2c** than S-**DR2c**.

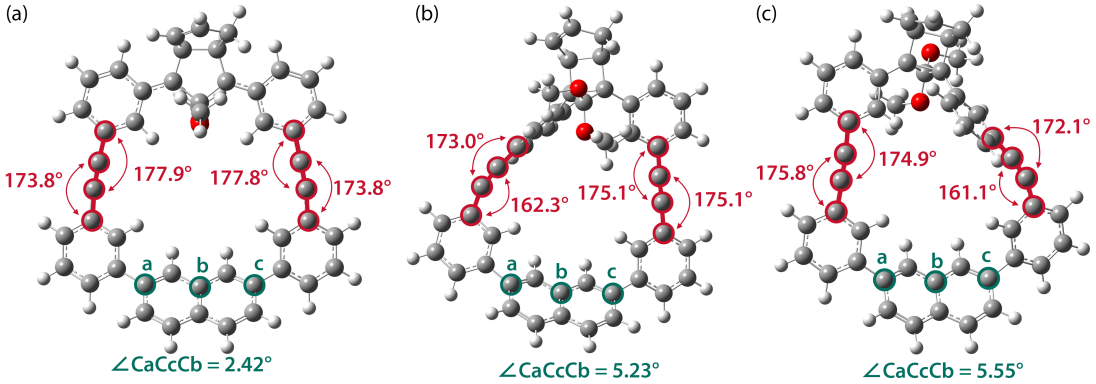

Figure 2.11 Bending angles of triple bonds and naphthyl moieties in (a) S-**DR2c**, (b) *cis-twi*-**CP2c** and (c) *trans-twi*-**CP2c**.

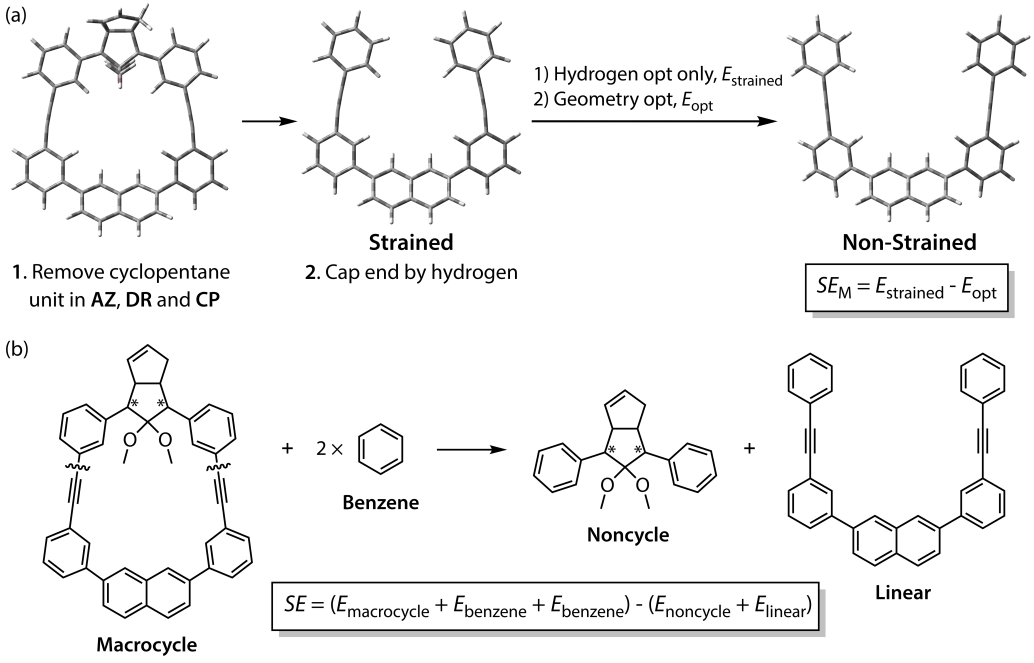

Figure 2.12 Strain energy calculation of (a) SE_M and (b) *SE*.

To understand the relationship between molecular strain and stretch effect, the strain energy of macrocyclic skeleton (SE_M) was estimated by computing the energy difference between the bent macrocyclic skeleton and strain-released macrocyclic skeleton at (R)ωB97X-D/6-31G(d) level of theory (Figure 2.12a). The SE_M values were calculated by subtracting the total electronic energy of the strain-released (*i.e.*, non-strained) macrocyclic skeleton, 2,7-bis(3-(phenylethynyl)phenyl)naphthalene, from the electronic energy of strained macrocyclic skeletons in **AZ2c**, S-**DR2c**, and **CP2c**. The latter were obtained by replacing the azo, diradical, and ring-closing units with two hydrogen atoms, and their electronic energies were accessed by partial optimization of two C–H bonds without any adjustment of other parts. The SE_M were relatively smaller in **AZ2c** and S-**DR2c** than those in **CP2c**, which have more bent triple bonds and naphthyl moieties (Table 2.2 and Figure 2.11).

Table 2.2 Strain energies of the macrocycle (SE_M) and molecular strain energies (SE) calculated at (R/U)ωB97X-D/6-31G(d) level of theory. Energy values in kJ mol^{-1}.

Entry		SE_M	SE	$\Delta\Delta H_{\mathbf{DR–CP}}$
1	**AZ2c**	11.24	17.45 (–)	–
2	S-**DR2c**	16.38	8.92 (0.00)[a]	–
3	*cis-par*-**CP2c**	29.13	32.18 (23.26)[a]	23.01
4	*cis-twi*-**CP2c**	36.26	43.66 (34.74)[a]	35.15
5	*trans-par*-**CP2c**	34.85	36.18 (27.26)[a]	28.60
6	*trans-twi*-**CP2c**	38.56	45.08 (36.16)[a]	37.00

[a] Values relative to S-**DR2c**.

The molecular strain energies (SE) of **AZ2c**, S-**DR2c**, and **CP2c** were estimated by computing the electronic energy difference of isodesmotic reactions at (R/U)ωB97X-D/6-31G(d) level of theory (Figure 2.12b). The SE were larger than the corresponding SE_M due to the ignorance of torsional strain in the computations of SE_M, except S-**DR2c**, since the diradical could be stabilized by delocalization (Table 2.2). The strain energies relative to S-**DR2c** were very similar to the differences between the corresponding $\Delta H_{\mathbf{DR–CP}}$ of **CP1** and **CP2c** ($\Delta\Delta H_{\mathbf{DR–CP}}$), which were calculated from the energy profiles (Figure 2.10). This phenomenon indicates that the molecular strains made a significant contribution to the destabilization of macrocyclic **CP2c** and provided the kinetic stabilization of S-**DR2c**.

2.2.2 Synthesis and Characterization

Since the stretch effect in the newly designed macrocyclic diradical was proved by computational studies, the synthesis of the precursor of singlet diradicaloids S-**DR1** and S-**DR2d**, azoalkanes **AZ1** and **AZ2d**, has been conducted according to Scheme 2.5. It was reported that the quantum yield of this clean photoreaction is nearly 100% to generate singlet diradicaloids.[10] To ensure sufficient solubility of **AZ2c**, octyl chains were attached to the side-phenyl rings. According to a previous study, the alkyl chains have negligible influence on the reactivity of singlet diradicaloids, so S-**DR2d** was expected to show a longer lifetime than S-**DR1**.[17]

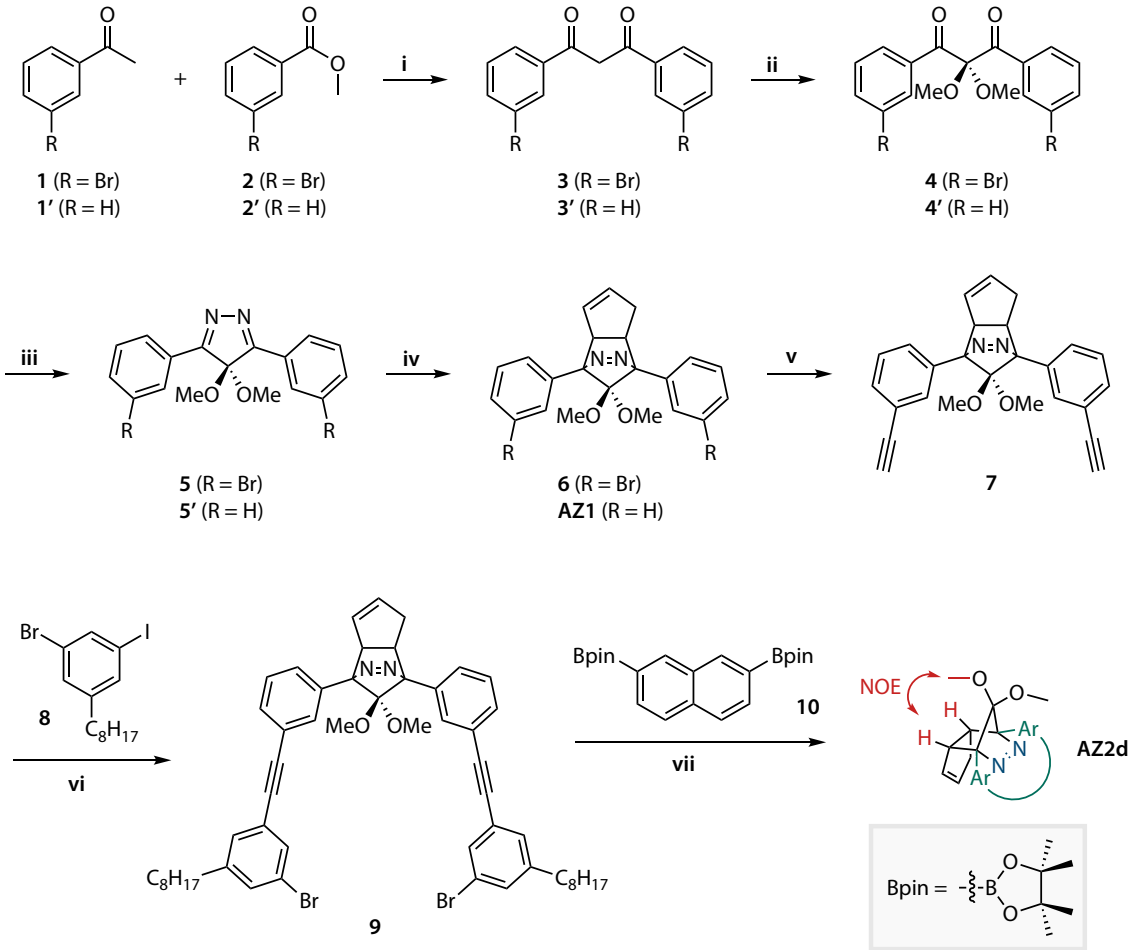

Scheme 2.5 Synthetic routes toward azoalkane **AZ1** and **AZ2d**. (i) NaH, THF, 0°C, 20 h, 87%; (ii) Ph_2Se_2, $(NH_4)_2S_2O_8$, MeOH, 75°C, 3.5 h; (iii) $N_2H_4 \cdot H_2O$, $CHCl_3$, 70°C, 16 h, 29% of 2 steps; (iv) cyclopentadiene, TFA, DCM, 0°C, 1.5 h, 73%; (v) **1**: trimethylsilylacetylene, $Pd(PPh_3)_4$, CuI, TEA, THF, 60°C, 43.5 h; **2**: K_2CO_3, THF, MeOH, r.t., 16.5 h, 82% of 2 steps; (vi) $Pd(PPh_3)_4$, CuI, TEA, THF, 60°C, 39.5 h, 79%; (vii) $Pd(OAc)_2$, SPhos, K_3PO_4, THF, H_2O, 80°C, 21 h, 2.8%.

The synthesis started from Claisen condensation of 3-bromoacetophenone **1** and methyl 3-bromobenzoate **2** in tetrahydrofuran solution with the presence of sodium hydride to give diketone compound **3** in 87% of yield. Then, methoxylation of diketone **3** was conducted in methanol solution by the oxidation with diphenyl diselenide and ammonium peroxodisulfate, leading to compound **4**. Compound **4** was directly used without any purification for the synthesis of pyrazole compound **5**, with the presence of hydrazine monohydride in chloroform solution. Diels-Alder reaction of pyrazole **5** and cyclopentadiene in dichloromethane solution catalyzed by trifluoroacetate acid led to azoalkane **6**. Then, Sonogashira coupling reaction between compound **6** and trimethylsilylacetylene catalyzed by tetrakis(triphenylphosphine)palladium(0) and following with deprotection with potassium carbonate was able to give compound **7**. The Suzuki-Miyaura cross-coupling reaction between compound **7** and 1-bromo-3-iodo-5-octylbenzene **8**, which was synthesized from 4-octylaniline, gave compound **9** in 79% of yield. Then, cyclization by intermolecular Suzuki-Miyaura coupling reaction between compounds **9** and **10** in the presence of palladium(II) acetate and ligand SPhos lead to the target compound **AZ2d** in 2.8% of yield. The compound **10** was synthesized by Miyaura-Ishiyama borylation of 2,7-dibromonaphthalene. The synthesis of **AZ1** followed a similar route, started from acetophenone **1'** and methyl benzoate **2'**.[10]

AZ2d was assigned by ^{1}H, ^{13}C NMR spectra, and mass spectroscopy. The correlation between a methoxy group and the bridgehead protons of cyclopentene-ring was observed by the two-dimensional nuclear Overhauser effect (NOESY) spectrum, confirmed its *endo* configuration (Scheme 2.6). After several attempts, the single crystal suitable for X-ray crystallographic analysis was prepared using chloroform and hexane by the vapor diffusion method. Although atomic disorder was observed for the octyl chains, the macrocyclic structure and *endo* configuration of azoalkane were confirmed (Figure 2.13).

The absorption spectrum of azoalkanes **AZ1** and **AZ2d** were recorded in benzene at 298 K (Figure 2.14). The maximum absorption derived from the n-π* electronic transitions of the azo chromophore (–N=N–) were observed at 358 and 356 nm for **AZ1** and **AZ2d**, respectively. The molar extinction coefficient of **AZ2d** at 356 nm was 517 $dm^3\ mol^{-1}\ cm^{-1}$, which was 4.6 times larger than that of **AZ1** at 358 nm (ε_{358} = 112 $dm^3\ mol^{-1}\ cm^{-1}$).

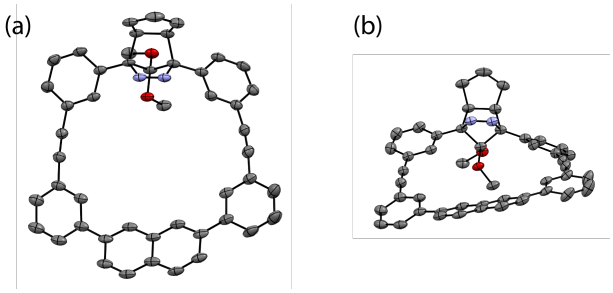

Figure 2.13 ORTEP diagrams of **AZ2d** in (a) top view and (b) front view. Thermal ellipsoids at 50% probability, all hydrogen atoms and octyl chains are omitted for clarity.

Furthermore, a broad absorption band derived from the π-π* electronic transition was recorded up to 450 nm, overlapping with the n-π* electronic transition of the azo unit, resulting in a large molar extinction coefficient of **AZ2d** compared with **AZ1** at ~360 nm. To this end, the photolysis of **AZ2d** with 350~360 nm light not only excites the azo chromophore to generate the singlet diradicaloids but also generates the photo-excited state of the π-conjugation system.

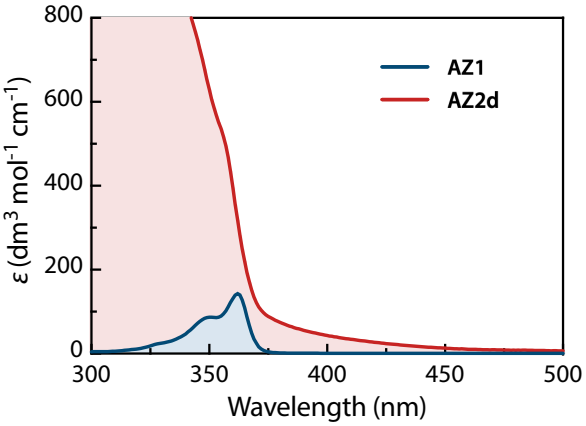

Figure 2.14 UV-vis absorption spectra of **AZ1** (2.87 mM) and **AZ2d** (2.13 mM) in benzene at 298 K.

2.2.3 Product Analyses of Photoreaction

To gain insight into the ring-closing processes of singlet diradicaloids, *in situ* photoreactions of azoalkane **AZ1** and **AZ2d** were carried out in deuterated benzene at 298 K under nitrogen atmosphere with a 365 nm LED lamp. The reaction processes were directly monitored by the ^{1}H NMR spectrum and NOESY measurement.

Photolysis of **AZ1** under nitrogen atmosphere quantitively generated *trans*-**CP1** (Figure 2.15b). The resulted solution was exposed to air

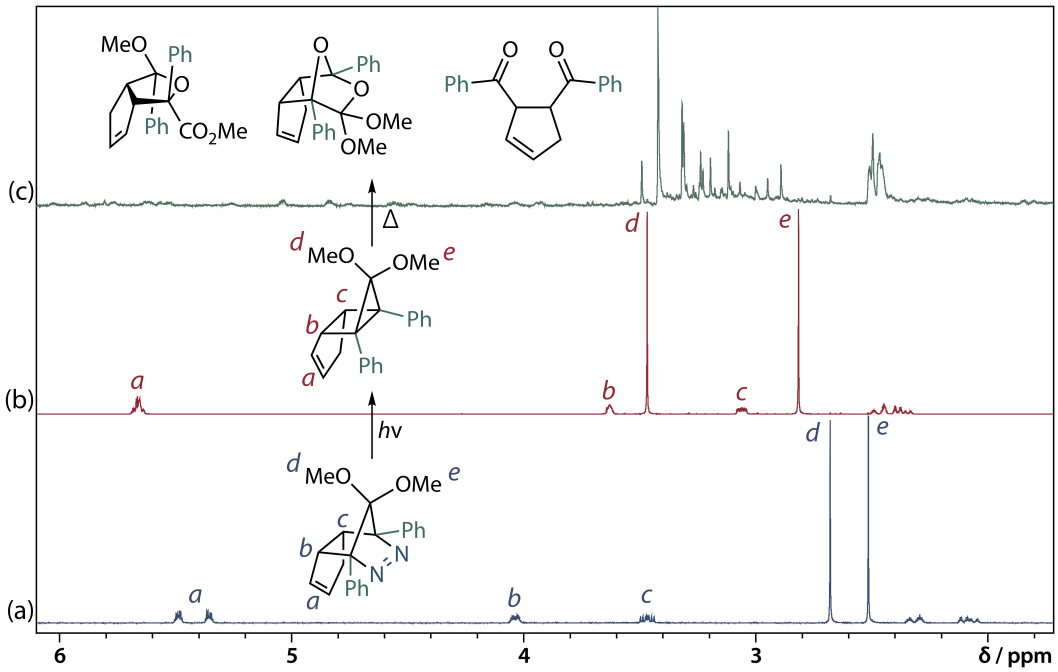

Figure 2.15 *In situ* ^{1}H NMR (400 MHz) analysis of the photoreaction of **AZ1** (6.35 mM in degassed C_6D_6). ^{1}H NMR spectrum of (a) **AZ1** before irradiation; (b) *trans*-**CP1** after irradiation with a 365 nm LED lamp for 180 s at 298 K under nitrogen atmosphere; (c) *trans*-**CP1** decomposition upon heating to 60°C under air atmosphere for 1 h.

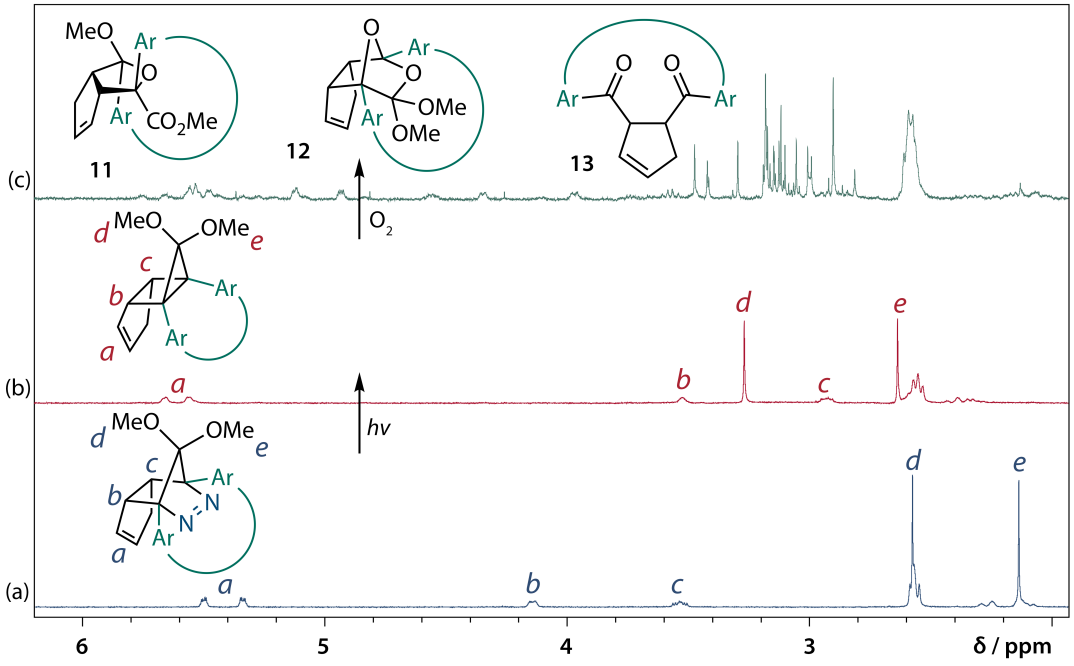

Figure 2.16 *In situ* ^{1}H NMR (400 MHz) analysis of the photoreaction of **AZ2d** (4.47 mM in degassed C_6D_6). ^{1}H NMR spectrum of (a) **AZ2d** before irradiation; (b) *trans*-**CP2d** after irradiation with a 365 nm LED lamp for 90 s at 298 K under nitrogen atmosphere; (c) *trans*-**CP2d** decomposition upon exposure to air for 3 min.

atmosphere for one day, and no change was observed in the ^{1}H NMR spectrum, indicating the air stability of *trans*-**CP1**.

On the other hand, *trans*-**CP2d** was quantitively formed during photolysis of **AZ2d** under nitrogen atmosphere (Figure 2.16b). This sensitive product decomposed immediately after exposure to air by removing NMR tube cap within second (Figure 2.16c). The fast decomposition of macrocyclic ring-closed product is likely due to the stretch effect, which destabilized the ring-closed product (*i.e.*, *trans*-**CP2d**). According to previous studies, the similar decomposition was confirmed for *trans*-**CP2b** at room temperature under air, and *trans*-**CP1** under air at 60°C (Figure 2.15c). The proposed mechanism for decomposition involved the endoperoxide, which is generated from the reaction between oxygen and triplet diradicals (Scheme 2.6).[9]

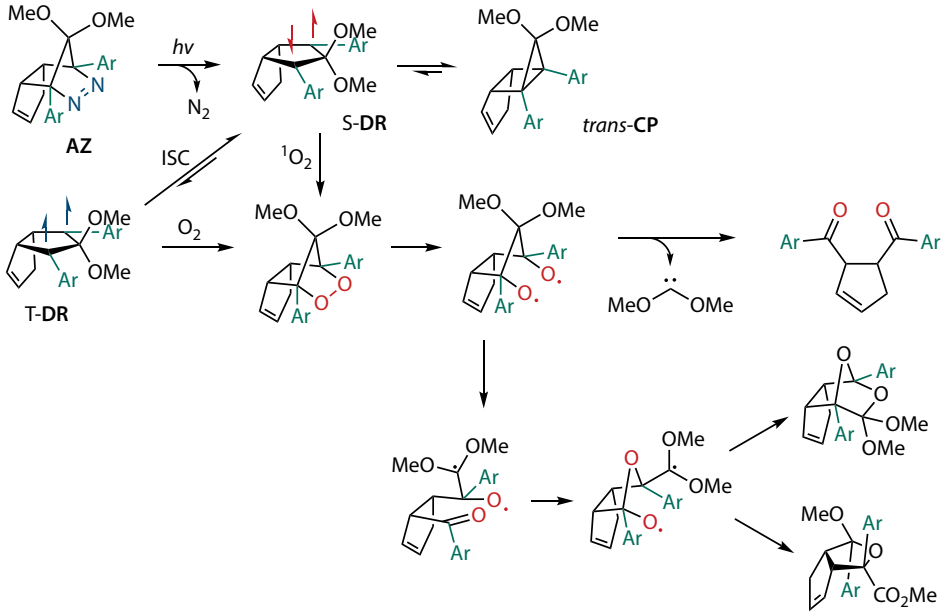

Scheme 2.6 Proposed mechanism for decomposition of ring-closed products.

The exclusive formation of *trans*-**CP2d** was confirmed during the photoreaction of **AZ2d** at room temperature, although the calculated energy barrier for the formation of *cis*-**CP2d** was smaller than that for the *trans*-**CP2d**. Thus, the isomerization from *cis*-**CP2d** to *trans*-**CP2d** occurred at room temperature, and it might be inhibited at low temperature by larger activation energy (>70 kJ mol^{-1} from S-**DR2d** to *trans*-**CP2d** at 199 K). To identify the primary product of the photoreaction at 199K, the photolysis with a 355 nm Nd:YAG laser (30 mJ/pulse) of **AZ2d** in deuterated toluene was conducted under argon atmosphere. The vinylic protons on the double

bond of cyclopentene ring were monitored during *in situ* ^{1}H NMR experiments. After irradiation of 20 minutes, new signals *c* and *d* derived from *trans*-**CP2d** were observed alongside unreacted **AZ2d** (signals *a* and *b*, Figure 2.17). The exclusive formation of *trans*-**CP2d** could be explained by the existence of puckered singlet diradicaloid *puc*-^{1}**DR2d**, which is generated from denitrogenation. The *puc*-^{1}**DR2d** could give the *trans*-**CP2d** directly by bond formation through a negligible energy barrier (Scheme 2.7).

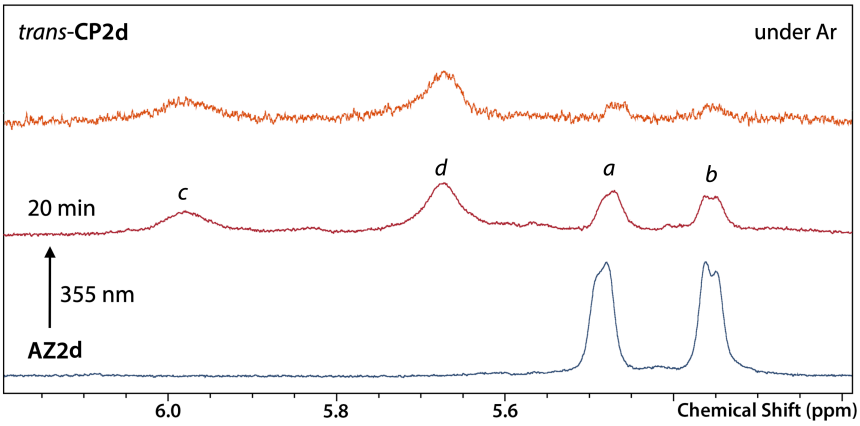

Figure 2.17 *In situ* ^{1}H NMR (400 MHz) analysis of the direct irradiation of **AZ2d** (6.49 mM) in degassed d_8-toluene at 199 K with Nd:YAG 355 nm (30 mJ) laser.

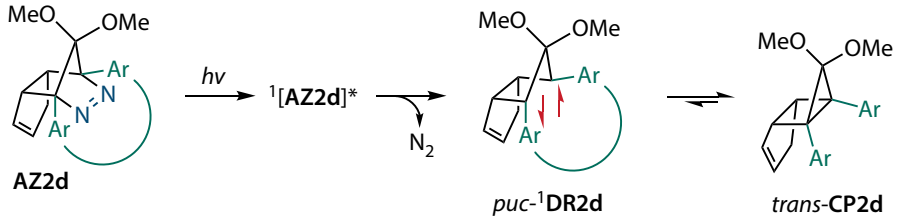

Scheme 2.7 Proposed mechanism of exclusive formation of *trans*-**CP2d** at 199 K.

Using the same experimental setup, a degassed deuterated toluene solution of **AZ2d** with 15 equivalent of triplet sensitizer benzophenone was irradiated with 355 nm laser under argon atmosphere at 199 K. Interestingly, after 15 minutes of irradiation, new signals *e* and *f* were observed beside *trans*-**CP2d** (signals *c* and *d*) and **AZ2d** (signals *a* and *b*, Figure 2.18). The signals *e* and *f* gradually converted to *trans*-**CP2d** under dark condition. Thus, the new signals should be derived from an intermediate between **AZ2d** and *trans*-**CP2d**, and its lifetime should be long enough to be recorded by NMR spectrometer at 199 K (about 6 minutes for one measurement). Hence, the new signals *e* and *f* corresponded to *cis*-**CP2d**, which subsequently isomerized to the more stable *trans*-**CP2d**. The formation of *cis*-**CP2d**

included the triplet diradical with a planar structure *pl*-^{3}**DR2d**, which is generated from the energy transfer from triplet excited state of benzophenone (Scheme 2.8). Then, intersystem crossing occurred to form the planar singlet diradicaloids *pl*-^{1}**DR2d** (*i.e.*, S-**DR2d**), making it possible to go to *cis*-**CP2d**.

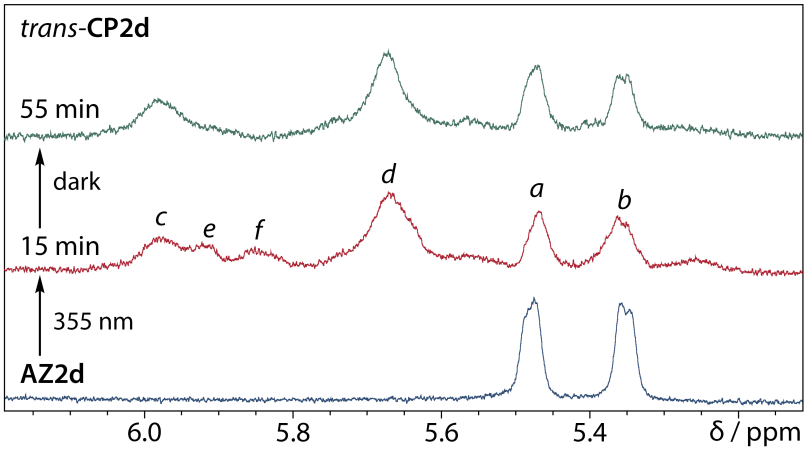

Figure 2.18 *In situ* ^{1}H NMR (400 MHz) analysis of the irradiation of **AZ2d** (0.60 mM) in the presence of benzophenone (9.32 mM) in degassed d_8-toluene at 199 K with Nd:YAG 355 nm (30 mJ) laser.

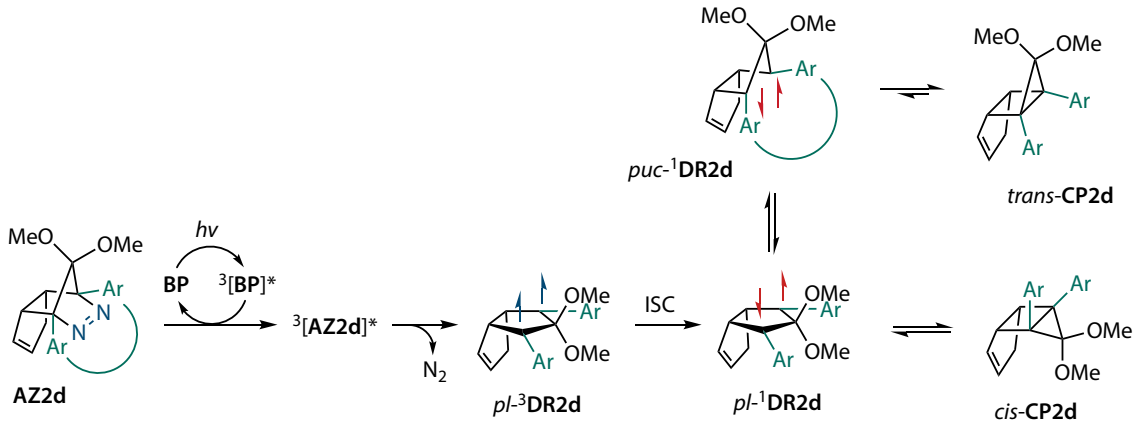

Scheme 2.8 Proposed mechanism of formation of *cis*-**CP2d** at 199 K. ISC: intersystem crossing.

2.2.4 Direct Observation of Singlet Diradicaloid

Sub-microsecond transient absorption spectroscopy was conducted to monitor the laser flash photolysis of **AZ2d** in degassed benzene at 293 K using a Nd:YAG 355 nm laser (7 mJ, 5 ns/pulse). Two strong transient absorption bands were detected at 460 and 580 nm (Figure 2.19a). For the 460 nm absorption band, it had a lifetime τ_{293} of 3.08 ± 0.02 μs under nitrogen, while it was quenched to τ_{293} = 426 ± 4 ns under air atmosphere by molecular

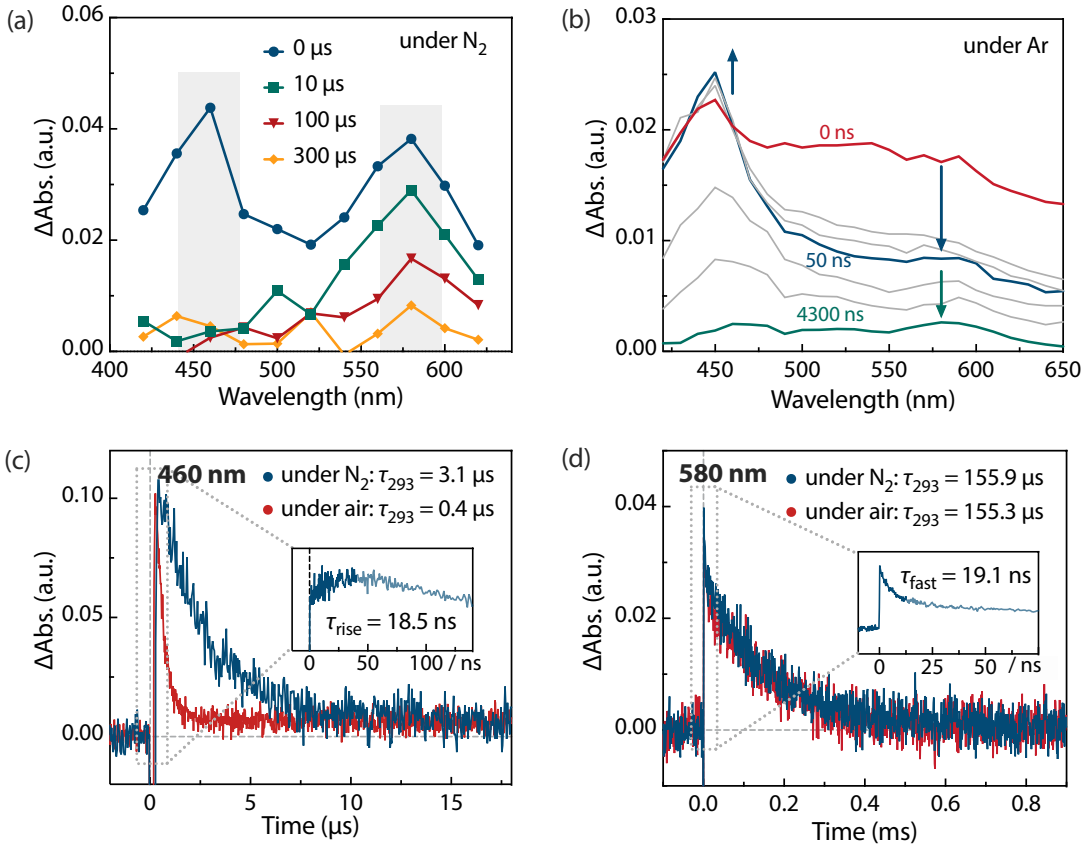

Figure 2.19 Transient absorption spectra during the laser flash photolysis of **AZ2d** (λ_{exc} = 355 nm) at 293 K in benzene. (a) Sub-microsecond transient absorption spectra of **AZ2d** (2.68 mM, Abs_{355} = 0.72) under nitrogen atmosphere; (b) Sub-nanosecond transient absorption spectra of **AZ2d** (7.19 mM, Abs_{355} = 0.77) under argon atmosphere; time profile monitored at (c) 460 nm under nitrogen and air atmosphere; inset: time delay from –15 to 140 ns under argon; and at (d) 580 nm under nitrogen and air atmosphere; inset: time delay from –10 to 75 ns under argon.

oxygen with a quenching rate constant $k_q(O_2) = 1.10 \times 10^9$ M^{-1} s^{-1} (Figure 2.19c). Thus, the 460 nm absorption derived from a triplet specie. On the other hand, the transient specie with 580 nm absorption showed a dual decay process (Figure 2.19d). Sub-nanosecond transient absorption spectroscopy using a randomly interleaved pulse train (RIPT)[29] method was conducted to monitor the fast decay process at 580 nm under argon atmosphere (Figure 2.19b). The fast decay process was attributed to the depletion of singlet excited state of **AZ2d** since the fall rate constant of fast decay at 580 nm (k_f = 5.24 × 10^7 s^{-1}) was consistent with the rise rate constant (k_r = 5.41 × 10^7 s^{-1}) of the triplet specie at 460 nm (inset of Figure 2.19c,d). The slow decay

process at 580 nm was long-lived to τ_{293} = 155.9 ± 3.3 μs under nitrogen atmosphere, and it showed an identical lifetime (τ_{293} = 155.3 ± 2.7 μs) under air atmosphere. According to the previous report, the π-π* (HOMO–LUMO) electronic transitions of π-single bonding systems have maximum absorption in the range of 500–600 nm.[1] Hence, the slow decay process at 580 nm corresponds to the ring-closing reaction from S-**DR2d** to *cis*-**CP2d**. As predicted by computations, the stretch effect elongated the lifetime of S-**DR2d** to 155.9 μs in benzene at 293 K, which was approximately 750- and 11-fold longer than that of S-**DR1** and S-**DR2a**/**b**, respectively.[10,17]

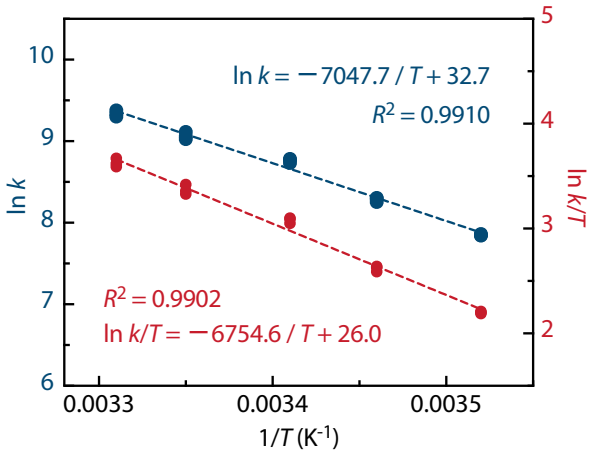

Figure 2.20 Arrhenius plot (blue) and Eyring plot (red) of ring-closing process of S-**DR2d** recorded in benzene under nitrogen atmosphere.

Table 2.3 Lifetime τ_{293} of singlet diradicaloids S-**DR** at 293 K and activation parameters (E_a, log A, $\Delta H^{\ddagger}$, $\Delta S^{\ddagger}$ and $\Delta G^{\ddagger}_{293}$) of the ring-closing process in benzene.

S-**DR**	**1**	**2b**	**2d**
τ_{293} / μs	0.21 ± 0.01	14.2 ± 0.8	155.9 ± 3.3
E_a / kJ mol^{-1}	30.5 ± 0.4	52.3 ± 0.4	58.4 ± 1.1
log (A / s^{-1})	12.1 ± 0.1	14.1 ± 0.1	14.2 ± 0.2
$\Delta H^{\ddagger}$ / kJ mol^{-1}	28.0 ± 0.4	49.7 ± 0.4	56.0 ± 1.1
$\Delta S^{\ddagger}$ / J K^{-1} mol^{-1}	–21.5 ± 0.8	17.1 ± 1.2	18.1 ± 2.3
$\Delta G^{\ddagger}_{293}$ / kJ mol^{-1}	34.2 ± 0.8	44.7 ± 0.4	50.7 ± 1.1

Variable temperature laser flash photolysis (VT-LFP) measurements were conducted for **AZ2d** under nitrogen atmosphere at five temperatures in the range of 273–303 K. The activation parameters E_a, log A, $\Delta H^{\ddagger}$, $\Delta S^{\ddagger}$, and $\Delta G^{\ddagger}_{293}$ of the ring-closing process of S-**DR1** and S-**DR2d** in benzene were determined from Arrhenius and Eyring plots (Figure 2.20 and Table 2.3). The

activation energy and activation enthalpy of the ring-closing reaction of S-**DR2d** were increased by 28 kJ mol^{-1} compared with corresponding values for S-**DR1**. Different from the negative activation entropy of the ring-closing process of S-**DR1**, a positive value was associated with S-**DR2d**. Although the decay processes of S-**DR1** and S-**DR2d** are the same, the transition states of these reactions should be similar. Indeed, the computed activation entropy at ωB97X-D/6-31G(d) level of theory was –22.04 J mol^{-1} K^{-1}.

To directly observe the singlet diradicaloid S-**DR2d**, low-temperature UV absorption measurements were conducted for **AZ2d** in a 2-methyltetrahydrafuran (MTHF) matrix at 90 K under argon atmosphere. **AZ2d** in MTHF matrix was irradiated using a xenon lamp (λ_{exc} = 360 ± 10 nm). During irradiation, two strong absorption bands showed up at 460 and 580 nm, which were similar to those observed in transient absorption measurements (Figure 2.21a). However, once irradiation stopped, the 460 nm absorption band decayed within second, while the 580 nm absorption band persisted for more than 3 hours under dark condition (Figure 2.21b). Thus, the 460 nm absorption band derived from a photo-excited state, and the 580 nm absorption band derived from a long-lived intermediate.

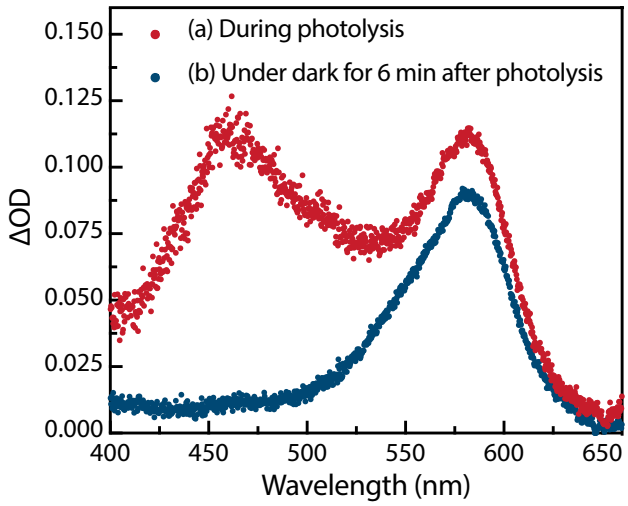

Figure 2.21 Low-temperature UV-vis absorption spectra (a) during photolysis of **AZ2d** (2.46 mM) and (b) under dark for 6 min after photolysis in a degassed 2-methyltetrahydrofuran (MTHF) matrix at 90 K.

To confirm the spin multiplicities of transient species associated with the absorption bands at 460 and 580 nm, electron paramagnetic resonance (EPR) measurements were carried out at 80 K in MTHF matrix under

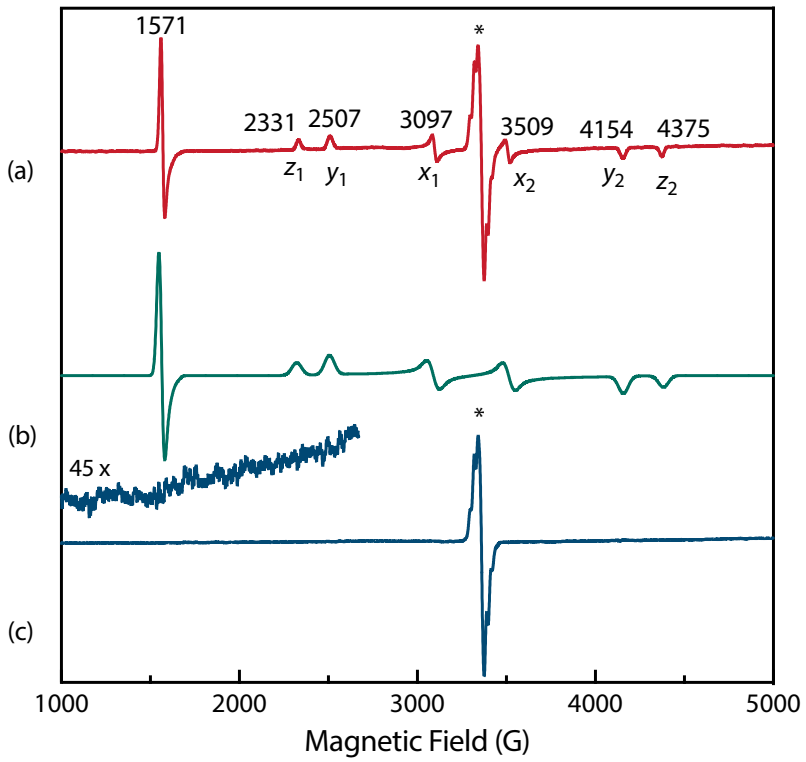

Figure 2.22 Experimental EPR spectra of **AZ2d** (4.92 mM in a MTHF matrix at 80 K) (a) during photolysis and (c) under dark condition after irradiation; inset: enhanced view from 1000–2670 G. (b) EPR spectrum simulated using $|D/hc| = 0.096$ cm^{-1} and $|E/hc| = 0.019$ cm^{-1}. The asterisk indicates signals that correspond to doublet impurities in MTHF.

vacuum condition. During the photolysis of **AZ2d** in MTHF matrix with a Hg lamp ($\lambda_{exc} > 250$ nm), EPR signals of typical triplet species were observed at 2331 (z_1), 2507 (y_1), 3097 (x_1), 3509 (x_2), 4154 (y_2), and 4375 Gauss (G) (z_2) corresponding to the allowed transition ($|\Delta m_s| = 1$) at 9.4 GHz resonance frequency. In addition, the half-field signal ($|\Delta m_s| = 2$) was detected at 1571 G (Figure 2.22a). Signals from doublet impurities in MTHF solvent were detected at approximately 3400 G, which were also observed in a control experiment by MTHF irradiation under the same conditions. The zero-field parameters (*zfs*) of observed triplet species were determined to be $|D/hc| = 0.096$ cm^{-1} and $|E/hc| = 0.019$ cm^{-1}, and the simulated spectrum using $|D/hc| = 0.096$ cm^{-1} and $|E/hc| = 0.019$ cm^{-1} confirmed the obtained *zfs* (Figure 2.22b). The experimental *zfs* were very similar to those of the triplet excited state of 2-phenylnaphthalene molecule ($|D/hc| = 0.0963$ cm^{-1} and $|E/hc| = 0.0274$ cm^{-1}),[30] and different from those of reported triplet 1,3-diphenylcyclopentane-1,3-diyl diradicals, which were $|D/hc| = 0.045$ cm^{-1}

and $|E/hc| = 0.0010$ cm^{-1}.[5,31] When the irradiation was cased at 80 K, the EPR signals for triplet species disappeared, indicating that the diradical **DR2d** has singlet ground state, and singlet diradicaloid S-**DR2d** is associated with the absorption band at 580 nm (Figure 2.22c). The EPR signals for triplet species lived for 2 s at 80 K by monitoring the decay profile at 1562 G, and the lifetimes were nearly the same in the temperature range of 5–80 K. The temperature-independency of the decay process support that the EPR signals were assigned to the triplet excited state of naphthyl moiety. The absorption band at 460 nm in low-temperature UV absorption measurements and transient absorption measurements were derived from T–T absorption of naphthyl moiety. Indeed, computation of a model molecule with TD-DFT method at the ωB97X-D/6-31G(d) level of theory predict the maximum absorption of T–T absorption appear at 460 nm, which well reproduced the experimental results (Figure 2.23).

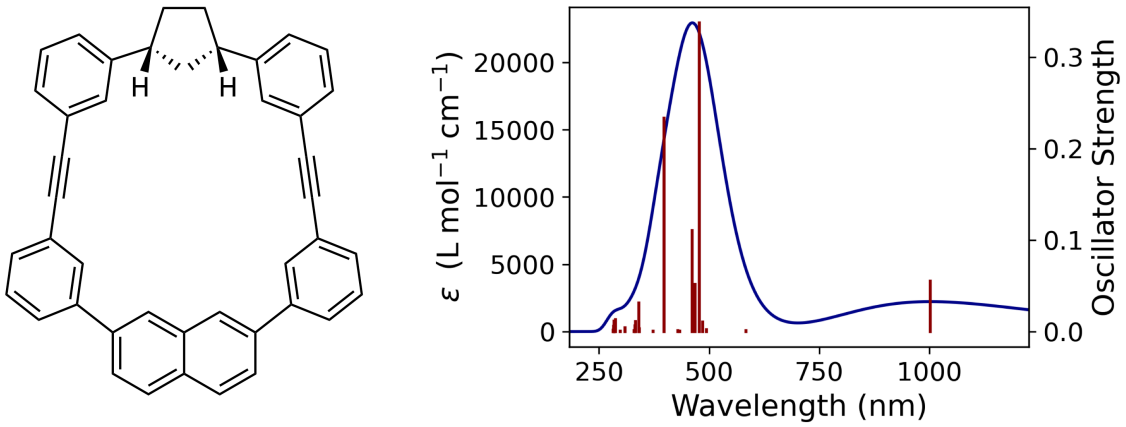

Figure 2.23 Model molecule used for TD-DFT calculation and calculated absorption spectrum at ωB97X-D/6-31G(d) level of theory.

Theoretical computation of *zfs* parameters for triplet diradicals T-**DR1** and T-**DR2c** were conducted with ORCA 5.0.3 program package[32,33] at the (RO)BP86/EPR-II[34,35] level of theory (Table 2.4). The reliability of computational results was confirmed by computing the *zfs* parameters of reported triplet 1,3-diyl diradicals **14**–**16**.[31] Although the $|E/hc|$ values differ greatly, the calculated $|D/hc|$ values showed great agreements with the experimental values of triplet diradicals **14**–**16**. The $|D/hc|$ value of T-**DR2d** predict by computation was 0.057 cm^{-1}, rather than the observed $|D/hc|$ of 0.096 cm^{-1} during the photolysis of **AZ2d** at 80 K.

Table 2.4 Experimental and computed *zfs* parameters, |*D*/*hc*| and |*E*/*hc*| of triplet state of **DR1**, **DR2c**, **14**, **15** and **16**.

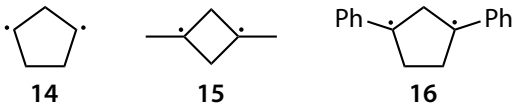

14 **15** **16**

Entry		Experimental (computed) *zfs* parameters / cm^{-1}	
		|*D*/*hc*|	|*E*/*hc*|
1	**DR1**	*N.D.* (0.0593)	*N.D.* (0.0076)
2	**DR2c**	*N.D.* (0.0576)	*N.D.* (0.0098)
3	**14**	0.084 (0.0853)	0.0020 (0.0030)
4	**15**	0.112 (0.1069)	0.0050 (0.0035)
5	**16**	0.045 (0.0421)	0.0010 (0.0011)

2.2.5 Solvent Effect on the Reactivity of Singlet Diradicaloids

Singlet diradicaloids with electron withdrawing groups at the C2 position have zwitterion character in their resonance form (Scheme 2.9).[9] Thus, the intramolecular radical–radical coupling reaction is supposed to be inhibited in the polar solvent. To investigate this relationship and the influence of the stretch effect on the stability of singlet diradicaloids in solution, laser flash photolysis measurements of **AZ1** and **AZ2d** were carried out in 13 solvents, including carbon tetrachloride, diethyl ether, ethyl acetate, toluene, benzene, 1,4-dioxane, acetone, glycerin triacetate (GTA), chloroform, dichloromethane, 1,2-dichloroethane, hexane, and dimethyl sulfoxide, with a broad range of solvent polarity and viscosity. The Kamlet-Abboud-Taft π* scale for solvent polarity was used in this study since it was found to more suitably describe the solvent polarity effect on the lifetime of singlet diradicaloid S-**DR1** than the other parameters such as $E_T(30)$ and dielectric constant ε_r (Figure 2.24). [36–39]

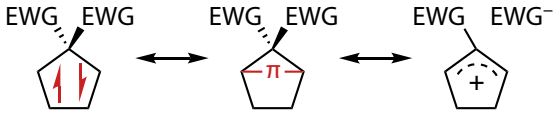

Scheme 2.9 Resonance structures of singlet diradicaloids with EWG at the C2 position.

The lifetimes of S-**DR1** and S-**DR2d** in these solvents at 293 K were determined by monitoring the time profile of laser flash photolysis at 580 nm (Table 2.5). A good correlation was found between lifetimes of S-**DR1** and

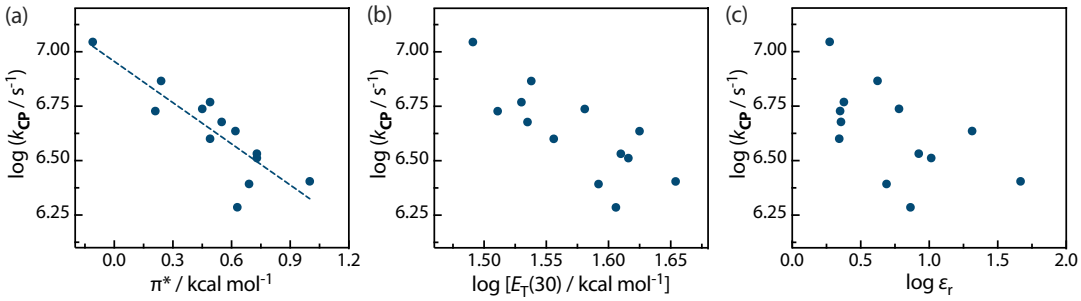

Figure 2.24 Correlations between the rate constant log $k_{\mathbf{CP}}$ and solvent polarity parameters: (a) Kamlet-Abboud-Taft π* scale; (b) $E_T(30)$; (c) dielectric constant ε_r.

solvent polarity π*, although no correlation was observed for S-**DR2d**. In low viscous solvents, the most extended lifetime of S-**DR2d** was determined in benzene, which was 5-fold than that in acetone, although acetone is a polar solvent than benzene (Table 2.5, entries 7,8). Among these solvents, acetone (Ac) and GTA have identical polarities ($\pi^*_{Ac} = 0.62$, $\pi^*_{GTA} = 0.63$), but the lifetime of S-**DR2d** in GTA was 2.5 and 13 times longer than that in acetone and benzene, respectively (Table 2.5, entry 9). The variable temperature laser flash photolysis measurements were conducted in these solvents, and activation parameters were determined from Arrhenius and Eyring plots. The activation energy in GTA was larger than those in other solvents, and the activation entropy significantly increased to 57.5 J mol^{-1} K^{-1}. On the other hand, the smallest activation entropy was determined for diethyl ether (η = 0.24 cP, $\Delta S^{\ddagger}$ = 8.5 J mol^{-1} K^{-1}), which is the lowest viscous solvent among these 13 solvents. These observations indicated that the solvent polarity was not the only factor that affects the reactivity of singlet diradicaloids, the solvent viscosity also influenced their lifetimes.

As the intramolecular radical–radical coupling reaction in S-**DR2d** strongly depends on the solvent viscosity, the dynamic solvent effect should be included in the ring-closing reactions of S-**DR** to **CP**.[40–44] Dynamic solvent effect was reported in the isomerization of azobenzene in viscous solvents, it is described using a two-dimensional reaction coordinate model. In this model, the reaction system and solvent are described by two independent steps using equation (1):

$$\mathrm{Z} \underset{k_{-f}}{\overset{k_f}{\rightleftharpoons}} \mathrm{M} \overset{k_{\mathrm{TST}}}{\rightarrow} \mathrm{E} \qquad (1)$$

Table 2.5 Lifetime τ_{293} of singlet diradicaloids S-**DR1** and S-**DR2d** at 293 K in different solvents encompassing a wide range of polarity (π*) and viscosity (η). The numbers in parentheses indicate the ascending order of the values in each column.

				τ_{293} / μs	
Entry	Solvent	π* / kcal mol^{-1}	η (20°C) / cP	S-**DR1**	S-**DR2d**
1	*n*-hexane	−0.11 (1)	0.31 (2)	90.1 (1)	*N.D.*
2	Tetrachloride carbon	0.21 (2)	0.97 (10)	187.1 (5)	17.2 (1)
3	Diethyl ether	0.24 (3)	0.24 (1)	136.3 (2)	46.8 (5)
4	Ethyl acetate	0.45 (4)	0.46 (5)	182.6 (4)	73.1 (8)
5	Toluene	0.49 (5)	0.59 (7)	170.4 (3)	116.5 (10)
6	1,4-Dioxane	0.49 (5)	1.18 (11)	250.6 (8)	61.4 (6)
7	Benzene	0.55 (7)	0.65 (8)	210.0 (6)	155.9 (11)
8	Acetone	0.62 (8)	0.32 (3)	231.4 (7)	27.9 (3)
9	Glycerin triacetate	0.63 (9)	23.00 (13)	517.1 (13)	400.2 (12)
10	Chloroform	0.69 (10)	0.58 (6)	404.8 (12)	65.4 (7)
11	Dichloromethane	0.73 (11)	0.44 (4)	294.0 (9)	46.6 (4)
12	1,2-Dichloroethane	0.73 (11)	0.79 (9)	307.6 (10)	22.8 (2)
13	Dimethyl sulfoxide	1.00 (13)	2.24 (12)	393.5 (11)	95.1 (9)

The solvent thermal fluctuation determines the first step from initial state **Z** to intermediate state **M**, and the fluctuation-limited rate constant k_f depends on the solvent viscosity. The chemical change from intermediate state **M** to final state **E** follows transition state theory (TST). Thus, the observed rate constant k_{obs} is examined by equation (2):

$$1/k_{obs} = 1/k_f + 1/k_{TST} \quad (2)$$

According to equation (2), in high viscous solvents, the k_f becomes the rate-determining step ($k_f << k_{TST}$), the dynamic solvent effect presents and TST is no longer valid. On the other hand, in low viscous solvents, the conversion from **M** to **E** is the rate-determining step ($k_f >> k_{TST}$) following TST, and the observed k_{obs} is nearly equal to k_{TST}.

Since acetone (Ac) and GTA have identical polarities and significant differences in viscosities, we assumed that the dynamic solvent effect was invalid in acetone and solvent thermal fluctuation in acetone was sufficiently fast due to its low viscosity. Thus, in GTA, $k_{obs} = k_{GTA}$ and $k_{TST} = k_{Ac}$, and k_f could be estimated by $k_f = (1/k_{GTA} - 1/k_{Ac})^{-1}$. The strong correlation between estimated k_f and viscosity of GTA proved the validity of dynamic solvent

effect in the ring-closing process of S-**DR1** and S-**DR2d** in GTA (Figure 2.25).[45]

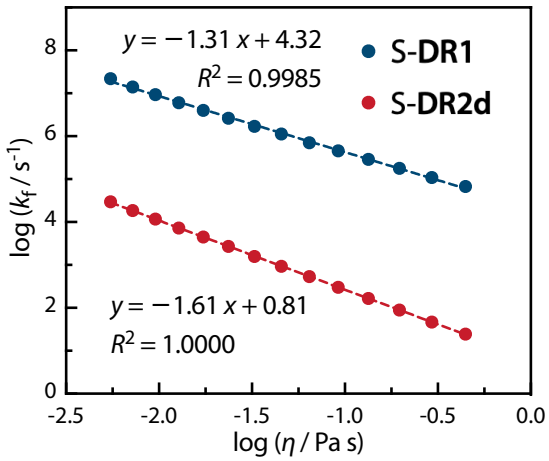

Figure 2.25 Dependence of the solvent fluctuation rate constant log k_f calculated by equation (1) on the viscosity of GTA. k_{Ac} and k_{GTA} were calculated from the Eyring plots.

The effect of solvent polarity and viscosity on the rate constant for ring-closing reaction of singlet diradicaloids S-**DR1** and S-**DR2d** were examined using equation (3) by performing regression analyses:

$$\tau_{293} = A\pi^* + B\eta + C \qquad (3)$$

where A and B were coefficients for solvent polarity and viscosity, respectively, and C was a compound-dependent constant. The constant term C indicated a predicted lifetime of singlet diradicaloids in the gas phase when both solvent polarity and viscosity are equal to 0.

Table 2.6 Regression analyses for fitting the observed lifetime τ_{293} to equation (3).

	S-**DR1**	S-**DR2d**
A / μs mol kcal^{-1}	0.278	15.99
B / μs cP^{-1}	0.011	14.94
C / μs	0.089	45.79
τ_{293} in hexane / μs	0.090	*N.D.*

According to the results of regression analyses, the solvent polarity was the dominant factor for determining the lifetime of S-**DR1**, as the polarity coefficient was much larger than the corresponding viscosity coefficient (ration A/B = 25.27). In contrast, both polarity and viscosity coefficients showed similar magnitude for S-**DR2d**, indicating that both solvent polarity

and viscosity were essential factors in the ring-closing process of S-**DR2d** (ration A/B = 1.07, Table 2.6). To check the validity of regression analyses, the experimental lifetime values τ_{293} were plotted against the predicted lifetime using equation (3). Good linear correlations were observed in both cases (R^2 = 0.86), despite the slight deviations of the data points corresponding to benzene, toluene for S-**DR2d** and chloroform for S-**DR1** (Figure 2.26).

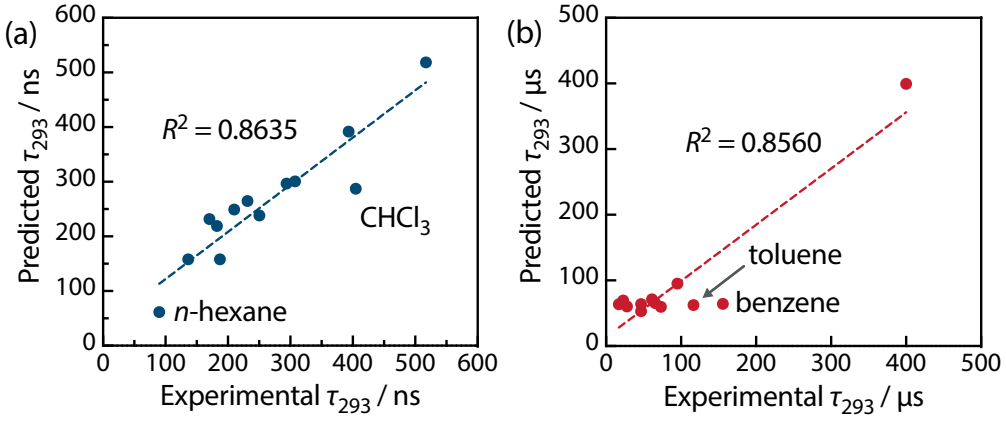

Figure 2.26 Correlation between the experimental and predicted lifetimes τ_{293} for (a) S-**DR1** and (b) S-**DR2d**.

The molecular volumes of singlet diradicaloids S-**DR1** and S-**DR2d** were computed at the (U)ωB97X-D/6-31G(d) level of theory. The obtained volumes were 303.44 and 497.04 cm^3 mol^{-1}, respectively, indicating that the S-**DR2d** with a larger molecular volume was more sensitive to the solvent viscosity during the ring-closing process.

2.3 Chapter Summary

Localized singlet diradicaloids are usually highly reactive and short-lived at ambient temperature due to a fast radical–radical coupling reaction. In this study, we applied the stretch effect, first proposed by our group in 2012, to a newly designed singlet diradicaloid with macrocyclic skeleton.

The photochemical denitrogenation of azoalkane **AZ2d** generated the kinetically stabilized diradicaloid S-**DR2d**. It exhibited a small carbon–carbon coupling reaction rate of 6.4×10^3 s^{-1} (155.9 μs), approximately 1000 times slower than that of the parent system without the macrocycle S-**DR1** (5×10^6 s^{-1}, 209 ns) at 293 K in benzene. Furthermore, the σ-bonded product **CP2d** was highly destabilized by the stretch effect, it decomposed immediately after exposure to air atmosphere, although the σ-bonded product with no-macrocyclic structure **CP1** was stable under air at room temperature. In addition, a significant dynamic solvent effect was observed in the intramolecular radical–radical coupling reactions. The lifetime of singlet diradicaloid S-**DR2d** showed the longest lifetime up to 400.2 μs in viscous glycerin triacetate (η = 23.00 cP) at 293 K. The theoretical and experimental studies demonstrated that the stretch effect and solvent viscosity play essential roles in retarding the σ-bond formation process, thus enabling a thorough examination of the nature of the singlet diradical and paving the way toward a deeper understanding of reactive intermediates.

2.4 Supplementary Materials

2.4.1 Experimental Section

All commercially available reagents were purchased from TCI, Wako, Sigma Aldrich or Oakwood Chemical and were used without further purification. Dry solvents for spectroscopy analysis were purchased from commercial suppliers. NMR spectra were recorded on a Bruker Ascend 400 (^{1}H NMR: 400 MHz, ^{13}C NMR: 100 MHz) spectrometer at 298 K and referenced to the residual solvent peak. Coupling constants (*J*) are denoted in Hz and chemical shifts (δ) in ppm. The abbreviations s, d, t, dd, dt, td and m stand for the resonance multiplicities singlet, doublet, triplet, doublet of doublets, doublet of triplets, triplet of doublets and multiplet, respectively. Mass spectrometric data were measured with Thermo Fisher Scientific LTQ Orbitrap XL. UV-vis spectra were recorded on a SHIMADZU UV-3600 Plus spectrometer. The spectra were collected at room temperature using a slit width of 1 nm with middle scan rate. The excitation source for sub-microsecond laser flash photolysis was a tunable Nd:YAG minilite laser at 355 nm. The monitoring system consisted of a 150 W xenon arc lamp as light source, a Unisoku MD200 monochromator detection and a photomultiplier. The temperature was controlled by Unisoku CoolSpek USP-203-B. Sub-nanosecond transient absorption measurements were conducted with Unisoku PicoTAS system in 2 mm cuvette. The excitation source was a passive Q-SWITCH microchip laser at 355 nm. Recycling chromatographic separation in GPC were performed by LC-9210, Japan Analytical Industry Co., Ltd. with chloroform as mobile phase.

E_a and log *A* of ring-closing processes of singlet diradicaloids were determined from Arrhenius plots, $\Delta H^{\ddagger}$, $\Delta S^{\ddagger}$ and $\Delta G^{\ddagger}_{293}$ were determined from Eyring plots, respectively, with lifetime of singlet diradicaloids at five temperatures, errors are standard errors obtained from regression analysis.

2.4.2 Synthetic Procedure

The synthetic procedure of azoalkane **AZ2d** from 3-bromoacetophenone **1** and methyl 3-bromobenzoate **2** is described below. Azoalkane **AZ1** was synthesized by same procedure of synthesis for compound **6** but started from acetophenone **1'** and methyl benzoate **2'**.

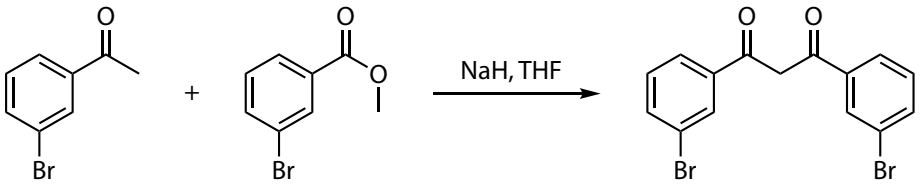

1 2 3

(i) A suspension of sodium hydride (4.97 g, 60%, 124.17 mmol, 2 equiv.) in dry THF (100 mL) was stirred at room temperature for 30 minutes in a side-arm round flask under nitrogen atmosphere. After cooling to 0°C, 3-bromoacetophenone (**1**, 8.00 mL, 60.29 mmol, 1 equiv.) and a solution of methyl 3-bromobenzoate (**2**, 12.71 g, 59.10 mmol, 1 equiv.) in THF (20 mL) were added to the stirred solution. The reaction mixture was stirred at 0°C for 5 h and at room temperature for additional 14.5 h. The reaction was quenched by pouring into a mixture of crashed ice and 1 mol L^{-1} hydrochloric acid solution. The suspension was filtered through Büchner funnel, and the organic product was washed with hexane to give **3** (19.58 g, 51.25 mmol, 87%) as white solid. **^{1}H NMR** (400 MHz, $CDCl_3$): δ = 8.12 (s, 2H), 7.91 (d, *J* = 7.83 Hz, 2H), 7.69 (d, *J* = 8.01 Hz, 2H), 7.38 (dd, *J* = 7.95, 7.89 Hz, 2H), 6.76 (s, 1H). **^{13}C NMR** (100 MHz, $CDCl_3$): δ = 184.41, 137.26, 135.49, 130.29, 130.25, 125.78, 123.02, 93.44. **HRMS (ESI)** calculated for $C_{15}H_{10}O_2Br_2Na$ $[M+Na]^+$ = 404.89193, found 404.89203.

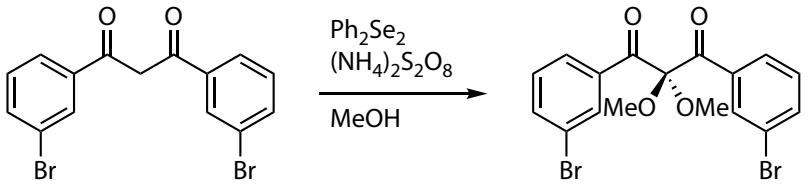

3 4

(ii) A two-neck flask equipped with a condenser was charged with **3** (22.23 g, 58.19 mmol, 1 equiv.), diphenyl diselenide (9.08 g, 29.09 mmol, 0.5 equiv.) and ammonium persulfate (26.55 g, 116.35 mmol, 2 equiv.) under nitrogen atmosphere. And the solids were mixed with methanol (220 mL). The reaction mixture was refluxed at 75°C for 3.5 h and then allowed to cool down to room temperature. Water was added to quench the reaction until all of the ammonium persulfate had dissolved, and the organic product was extracted with $CHCl_3$. The combined organic layers were dried over Na_2SO_4 and filtered. Removal of solvent under reduced pressure afforded **4** in a mixture as a dark orange oil, which was used for the next step without further

purification since **4** is labile in silica gel.

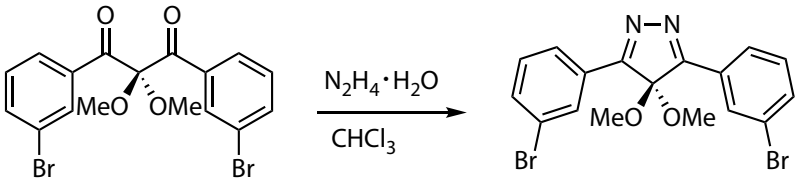

4 **5**

(iii) Hydrazine monohydrate (3.20 mL) was slowly added to the solution of **4** (10.49 g, crude) in $CHCl_3$ (100 mL) while stirring under nitrogen atmosphere. The reaction mixture was refluxed at 70°C for 16 h and saturated $NaHCO_3$ aqueous solution was added to quench the reaction at room temperature. After stirring at room temperature for 30 minutes, the resulting mixture was extracted with $CHCl_3$. The combined organic layers were washed with brine, dried over $MgSO_4$ and filtered. The solvent was removed *in vacuo*. The residue was purified by silica gel column chromatography (hexane/dichloromethane = 2:1) to give **5** (2.85 g, 6.01 mmol, 29% of 2 steps) as yellow solid. **^{1}H NMR** (400 MHz, $CDCl_3$): δ = 8.41 (s, 2H), 8.19 (d, *J* = 7.91 Hz, 2H), 7.70 (d, *J* = 8.09 Hz, 2H), 7.40 (dd, *J* = 8.00, 7.92 Hz, 2H), 3.07 (s, 6H). **^{13}C NMR** (100 MHz, $CDCl_3$): δ = 166.06, 135.48, 130.64, 130.50, 129.34, 126.32, 123.26, 117.08, 52.12. **HRMS (ESI)** calculated for $C_{17}H_{14}N_2O_2Br_2Na$ $[M+Na]^+$ = 460.92938, found 460.92923.

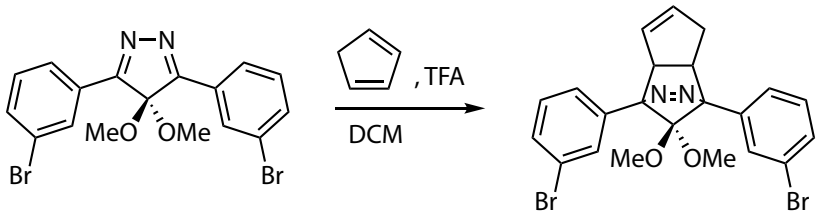

5 **6**

(iv) Under exclusion of light, a side-arm round flask was charged with the solution of **5** (3.01 g, 6.85 mmol, 1 equiv.) in CH_2Cl_2 (100 mL) and cyclopentadiene (11.53 mL, 137.80 mmol, 20 equiv.) under nitrogen atmosphere. The reaction mixture was cooled to 0°C and trifluoroacetic acid (0.10 mL, 1.34 mmol, 0.2 eq.) was added to the reaction mixture while stirring. After stirring at 0°C for additional 1.5 h, saturated $NaHCO_3$ aqueous solution was added for neutralization. The organic product was extracted by

CH_2Cl_2 and the combined organic layers were washed with brine, dried over $MgSO_4$ and filtered. The solvent was removed *in vacuo*. The residue was washed with hexane to give **6** (2.52 g, 5.01 mmol, 73%) as white solid. **^{1}H NMR** (400 MHz, $CDCl_3$): δ = 8.13 (s, 1H), 8.04 (s, 1H), 7.92 (d, *J* = 7.72 Hz, 1H), 7.82 (d, *J* = 7.72 Hz, 1H), 7.54 (t, *J* = 7.38 Hz, 2H), 7.34 (td, *J* = 7.96, 2.67 Hz, 2H), 5.61–5.56 (m, 1H), 5.51–5.46 (m, 1H), 4.15–4.09 (m, 1H), 3.70–3.62 (m, 1H), 3.00 (s, 3H), 2.71 (s, 3H), 2.41–2.38 (m, 1H), 2.34–2.15 (m, 1H). **^{13}C NMR** (100 MHz, $CDCl_3$): δ = 138.43, 138.25, 134.60, 131.79, 131.33, 131.18, 131.04, 130.07, 130.02, 127.27, 126.55, 126.12, 122.80, 122.73, 118.39, 94.00, 92.24, 57.26, 52.34, 51.99, 42.40, 32.16. **HRMS (ESI)** calculated for $C_{22}H_{20}N_2O_2Br_2Na$ $[M+Na]^+$ = 524.97837, found 524.97839.

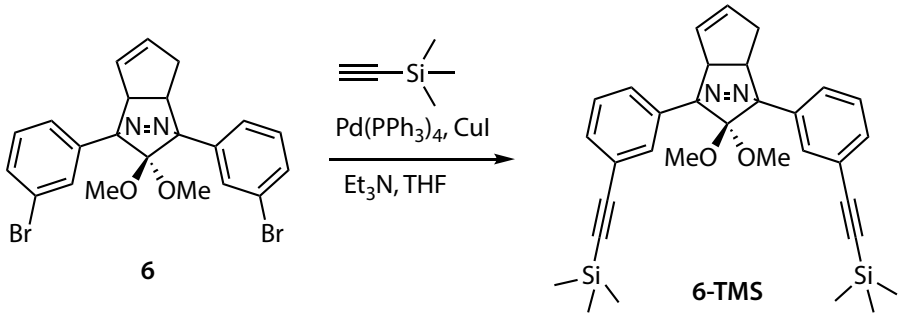

(v) Under exclusion of light, a side-arm round flask with a condenser was charged with **6** (0.76 g, 1.51 mmol, 1 equiv.), tetrakis(triphenylphosphine)palladium(0) (0.18 g, 0.16 mmol, 0.1 equiv.) and copper(I) iodide (0.04 g, 0.21 mmol, 0.1 equiv.) under nitrogen atmosphere. Anhydrous THF (20 mL), anhydrous triethylamine (5 mL) and trimethylsilylacetylene (2.25 mL, 16.26 mmol, 10 equiv.) were added into flask via a syringe. The reaction mixture was refluxed at 60°C for 43.5 h in the absence of light. After cooling to room temperature, the reaction mixture was filtered through a pad of celite and concentrated. The residue was redissolved in $CHCl_3$, organic layers were washed with saturated NH_4Cl aqueous solution and dried over Na_2SO_4. After filtering, the solvent was removed under reduced pressure. The residue was purified through a short silica gel column (hexane/ethyl acetate = 5:1) to afford **6-TMS** in mixture, hence **6-TMS** was directly used for the next step reaction.

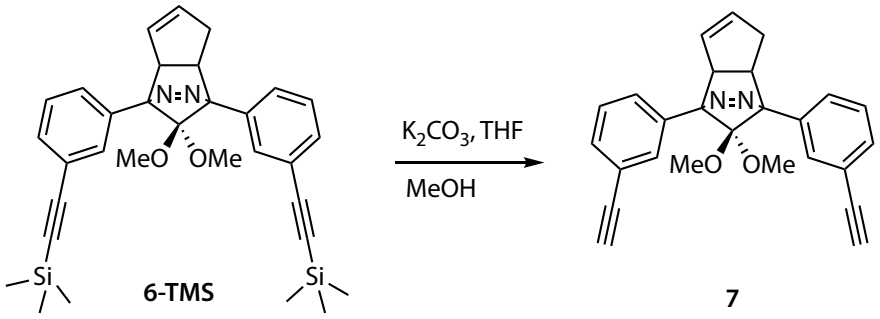

(vi) Under exclusion of light, the solution of **6-TMS** (4.23 g, mixture) in THF (50 mL), potassium carbonate (0.32 g) and methanol (90 mL) were charged into a round-bottom flask. The reaction mixture was stirred at room temperature for 16.5 h. After filtering through a pad of celite, the solvent was removed *in vacuo*. Water was added to the resulting crude and the organic product was extracted with ethyl acetate. The combined organic layers were washed with brine, dried over Na_2SO_4, filtered and concentrated. The residue was purified by silica gel column chromatography (hexane/ethyl acetate = 10:1) to give **7** (1.98 g, 5.01 mmol, 82% of 2 steps) as a white solid. **^{1}H NMR** (400 MHz, $CDCl_3$): δ = 8.10 (s, 1H), 8.02–7.97 (m, 2H), 7.91 (d, *J* = 7.58 Hz, 1H), 7.53 (dd, *J* = 6.89, 7.35 Hz, 2H), 7.43 (td, *J* = 7.81, 2.99 Hz, 2H), 5.61–5.55 (m, 1H), 5.51–5.46 (m, 1H), 4.18–4.12 (m, 1H), 3.74–3.65 (m, 1H), 3.11 (s, 2H), 2.98 (s, 3H), 2.69 (s, 3H), 2.41–2.30 (m, 1H), 2.25–2.14 (m, 1H). **^{13}C NMR** (100 MHz, $CDCl_3$): δ = 136.53, 136.35, 134.49, 132.23, 131.87, 131.71, 131.52, 129.42, 128.64, 128.53, 128.49, 126.27, 122.35, 122.30, 118.33, 94.08, 92.35, 83.71, 83.69, 57.12, 52.29, 52.24, 51.93, 51.90, 42.28, 32.18. **HRMS (ESI)** calculated for $C_{26}H_{22}N_2O_2Na$ $[M+Na]^+$ = 417.15735, found 417.15695.

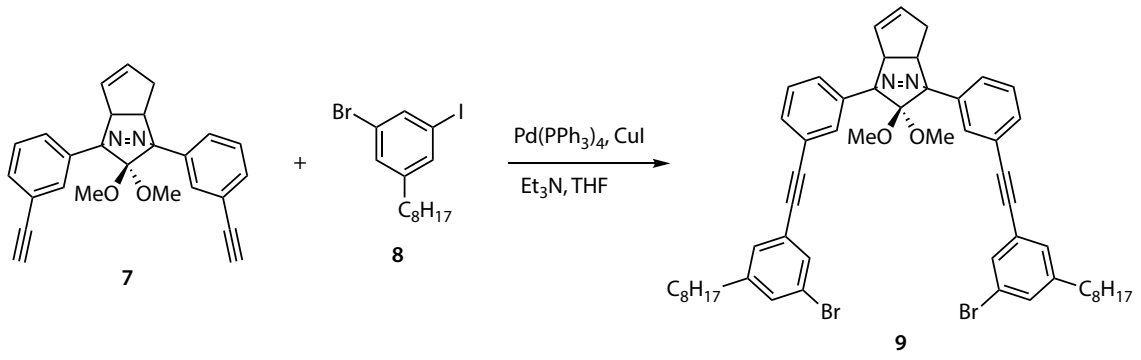

(vii) Under exclusion of light, a side-arm round flask with a condenser was charged with **7** (1.41 g, 3.57 mmol, 1 equiv.), tetrakis(triphenyl-

phosphine)palladium(0) (0.22 g, 0.19 mmol, 5% equiv.) and copper(I) iodide (0.06 g, 0.31 mmol, 0.1 equiv.) under nitrogen atmosphere. Anhydrous THF (36 mL), anhydrous triethylamine (13 mL) and 1-bromo-3-iodo-5-*n*-octylbenzene (**8**, 2.50 mL, 9.49 mmol, 2.5 equiv.) were added into flask via a syringe. The reaction mixture was refluxed at 60°C for 39.5 h in the absence of light. After cooling to room temperature, the reaction mixture was filtered through a pad of celite and concentrated. The residue was redissolved in $CHCl_3$, organic layers were sequentially washed with saturated NH_4Cl aqueous solution and water before dried over Na_2SO_4. After filtering, the solvent was removed under reduced pressure. The residue was purified by silica gel column chromatography (hexane/ethyl acetate = 10:1) to afford **9** (2.61 g, 2.82 mmol, 79%) as an orange oil. **^{1}H NMR** (400 MHz, $CDCl_3$): δ = 8.14 (s, 1H), 8.05 (s, 1H), 7.99 (d, *J* = 7.73 Hz, 1H), 7.91 (d, *J* = 8.19 Hz, 1H), 7.58–7.44 (m, 6H), 7.34–7.24 (m, 4H), 5.63–5.57 (m, 1H), 5.55–5.49 (m, 1H), 4.23–4.16 (m, 1H), 3.78–3.69 (m, 1H), 3.03 (s, 3H), 2.73 (s, 3H), 2.58 (t, *J* = 8.24 Hz, 4H), 2.45–2.33 (m, 1H), 2.29–2.18 (m, 1H), 1.68–1.55 (m, 4H), 1.40–1.20 (m, 20H), 0.89 (t, *J* = 7.37 Hz, 6H). **^{13}C NMR** (100 MHz, $CDCl_3$): δ = 145.19, 136.57, 136.39, 134.54, 131.84, 131.63, 131.57, 131.37, 131.20, 131.12, 130.33, 129.10, 128.65, 128.61, 128.35, 126.34, 124.83, 123.12, 123.08, 122.00, 118.37, 94.21, 92.47, 90.27, 90.25, 88.35, 88.32, 57.12, 52.28, 51.98, 42.28, 35.58, 32.25, 31.87, 31.10, 29.41, 29.21, 29.19, 22.67, 14.11. **HRMS (ESI)** calculated for $C_{54}H_{60}N_2O_2Br_2Na$ $[M+Na]^+$ = 951.28888, found 951.28933.

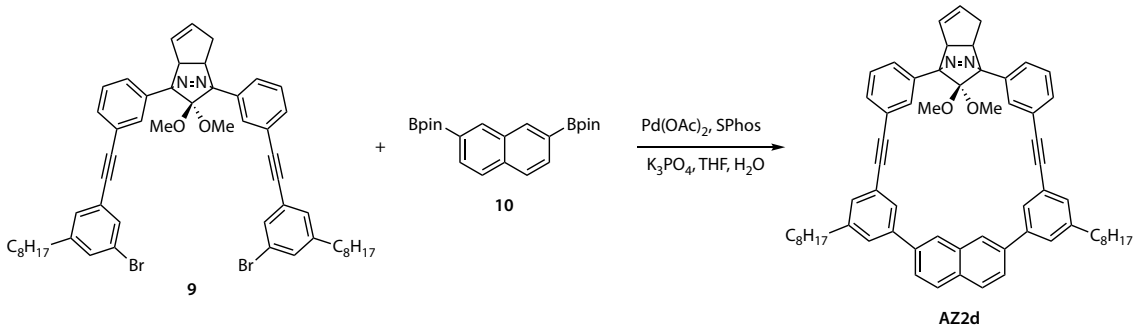

(viii) Under exclusion of light, **9** (660.0 mg, 0.71 mmol, 1 equiv.), palladium(II) acetate (34.2 mg, 0.15 mmol, 0.2 equiv.), **10** (269.1 mg, 0.71 mmol, 1 equiv.), potassium phosphate (603.4 mg, 2.84 mmol, 4 equiv.), 2-dicyclohexylphosphino-2',6'-dimethoxybiphenyl (**SPhos**, 117.2 mg, 0.29 mmol, 0.4 equiv.) were charged into a side-arm flask with a condenser.

Degassed THF (100 mL) and water (15 mL) were added into the flask under nitrogen atmosphere. The reaction mixture was refluxed at 80°C for 21 h in the absence of light. After cooling to room temperature, the reaction mixture was filtered through a pad of celite and concentrated. The residue was redissolved in $CHCl_3$, organic layers were washed with brine before and over Na_2SO_4. After filtering, the solvent was removed *in vacuo*. The residue was purified by silica gel column chromatography (hexane/dichloromethane = 1:2) to afford **AZ2d** (17.0 mg, 0.02 mmol, 2.8%) as a white solid. **^{1}H NMR** (400 MHz, C_6D_6): δ = 9.08 (d, *J* = 7.40 Hz, 2H), 8.27 (d, *J* = 5.16 Hz, 2H), 7.75 (d, *J* = 8.46 Hz, 2H), 7.72–7.65 (m, 4H), 7.63 (d, *J* = 8.17 Hz, 2H), 7.55 (s, 2H), 7.51 (s, 2H), 7.40 (d, *J* = 7.80 Hz, 1H), 7.31 (d, *J* = 8.08 Hz, 1H), 7.21–7.17 (m, 2H), 5.53–5.46 (m, 1H), 5.36–5.31 (m, 1H), 4.18–4.10 (m, 1H), 3.58–3.48 (m, 1H), 2.58 (s, 3H), 2.57 (t, *J* = 8.40 Hz, 4H), 2.32–2.21 (m, 1H), 2.14 (s, 3H), 2.14–2.05 (m, 1H), 1.66–1.53 (m, 4H), 1.36–1.20 (m, 20H), 0.96–0.85 (m, 6H). **^{13}C NMR** (400 MHz, $CDCl_3$): δ = 144.08, 141.21, 137.80, 137.34, 136.98, 136.92, 134.87, 134.61, 132.58, 132.35, 129.99, 129.93, 129.15, 128.65, 128.59, 128.54, 128.50, 126.90, 126.70, 120.50, 124.91, 124.80, 124.31, 119.52, 95.20, 93.70, 91.80, 90.88, 54.81, 52.15, 51.04, 41.13, 36.46, 32.35, 31.87, 29.95, 29.80, 29.71, 23.13, 14.40. **HRMS (ESI)** calculated for $C_{64}H_{66}N_2O_2Na$ $[M+Na]^+$ = 917.50165, found 917.50177.

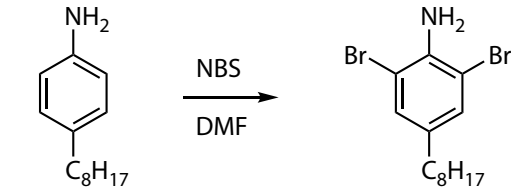

4-octylaniline **2,6-dibromo-4-octylaniline**

(ix) In a round-bottom flask, 4-*n*-octylaniline (5.00 mL, 21.87 mmol, 1 equiv.) was dissolved in *N*,*N*-dimethylformamide (20 mL) and iced at 0°C. The solution of *N*-bromosuccinimide (10.00 g, 56.19 mmol, 2.5 equiv.) in *N*,*N*-dimethyl-formamide (30 mL) was added into flask dropwise. The reaction mixture was stirred at 0°C for 30 minutes and at room temperature for additional 3 h. Then, water was added into the resulting mixture and the organic product was extracted with ethyl acetate. The combined organic layers were washed with saturated $Na_2S_2O_3$ aqueous solution, dried over $MgSO_4$ and filtered. Removal of solvent under reduced pressure gave 2,6-dibromo-4-*n*-octylaniline as a red solid in mixture (11.62 g), which was used

for next step without further purification.

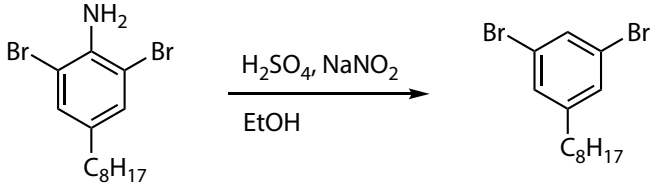

2,6-dibromo-4-octylaniline **1,3-dibromo-5-octylbenzene**

(x) A solution of 2,6-dibromo-4-*n*-octylaniline (11.62 g, crude) in ethanol (250 mL), concentrated sulfuric acid (30 mL) were charged into a side-arm flask with a condenser. Sodium nitrite (6.62 g) was slowly added into the mixture little by little while stirring. After refluxing at 70°C for 2 h, ice water was added to quench the reaction. The organic product was extracted by dichloromethane, and the organic layers were dried over Na_2SO_4, filtered and removed solvent under reduced pressure. The residue was purified by silica gel column chromatography (hexane only) to afford 1,3-dibromo-5-*n*-octylbenzene (4.80 g, 13.78 mmol, 63% of 2 steps) as a colorless liquid. **^{1}H NMR** (400 MHz, $CDCl_3$): δ = 7.48 (s, 1H), 7.25 (s, 2H), 2.54 (t, J = 7.63 Hz, 2H), 1.63–1.53 (m, 2H), 1.36–1.20 (m, 10H), 0.88 (t, J = 7.09 Hz, 3H). **HRMS (GC-EI)** calculated for $C_{14}H_{20}Br_2$ $[M]^+$ = 347.99118, found 347.99081.

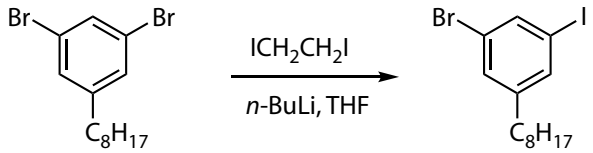

1,3-dibromo-5-octylbenzene **8**

(xi) At –78°C, a 2.3 M solution of *n*-BuLi in hexane (17.00 mL, 39.1 mmol, 1.1 equiv.) was added slowly to a solution of 1,3-dibromo-5-*n*-octylbenzene (12.14 g, 34.9 mmol, 1 equiv.) in THF (250 mL) via a syringe under nitrogen atmosphere. The reaction mixture was stirred at –78°C for 40 minutes, then a solution of 1,2-diiodoethane (11.83 g, 41.97 mmol, 1.2 equiv.) in THF (60 mL) was slowly added and the reaction mixture was allowed to warm to room temperature and stirred for additional 4 h. Then, solvent was removed *in vacuo*, and the residue was redissolved in diethyl ether. The solution was sequentially washed with saturated Na_2SO_3 aqueous solution, saturated $NaHCO_3$ aqueous solution and water before dried over Na_2SO_4 and

concentrated *in vacuo*. The crude was purified by silica gel column chromatography (hexane only) to provide **8** (11.72 g, 29.67 mmol, 85%) as a colorless liquid. **^{1}H NMR** (400 MHz, $CDCl_3$): δ = 7.66 (s, 1H), 7.45 (s, 1H), 7.28 (s, 1H), 2.51 (t, *J* = 8.09 Hz, 2H), 1.62–1.51 (m, 2H), 1.34–1.19 (m, 10H), 0.88 (t, *J* = 6.86 Hz, 3H). **HRMS (GC-EI)** calculated for $C_{14}H_{20}BrI$ $[M]^+$ = 393.97931, found 393.97853.

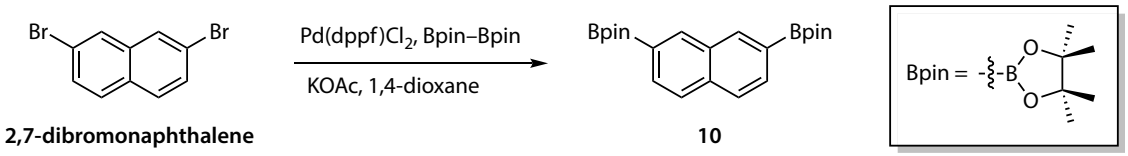

2,7-dibromonaphthalene **10**

(xii) A side-arm round flask with a condenser was charged with 2,7-dibromonaphthalene (1.23 g, 4.30 mmol, 1 equiv.), [1,1′-bis(diphenylphosphino)ferrocene]dichloropalladium(II) (0.16 g, 0.22 mmol, 5% equiv.), bis(pinacola-to)diboron (3.27g, 12.88 mmol, 3 equiv.), potassium acetate (2.54 g, 25.91 mmol, 6 equiv.) and 1,4-dioxane (10 mL) under nitrogen atmosphere. The reaction mixture was stirred at 75°C for 20 h. After cooling to room temperature, the mixture was filtered through a pad of celite and removed solvent *in vacuo*. The residue was purified by silica gel column chromatography (hexane/dichloromethane = 2:1) and gel permeation chromatography (chloroform only) to give **10** (1.44 g, 3.78 mmol, 88%) as a white solid. **^{1}H NMR** (400 MHz, $CDCl_3$): δ = 8.41 (s, 2H), 7.86 (d, *J* = 8.14 Hz, 2H), 7.80 (d, *J* = 8.14 Hz, 2H), 1.38 (s, 24H). **^{13}C NMR** (100 MHz, $CDCl_3$): δ = 137.11, 131.53, 126.78, 83.87, 25.02, 24.92. **HRMS (APCI)** calculated for $C_{22}H_{31}O_4B_2$ $[M+H]^+$ = 381.24030, found 381.24133.

2.4.3 Spectral Data

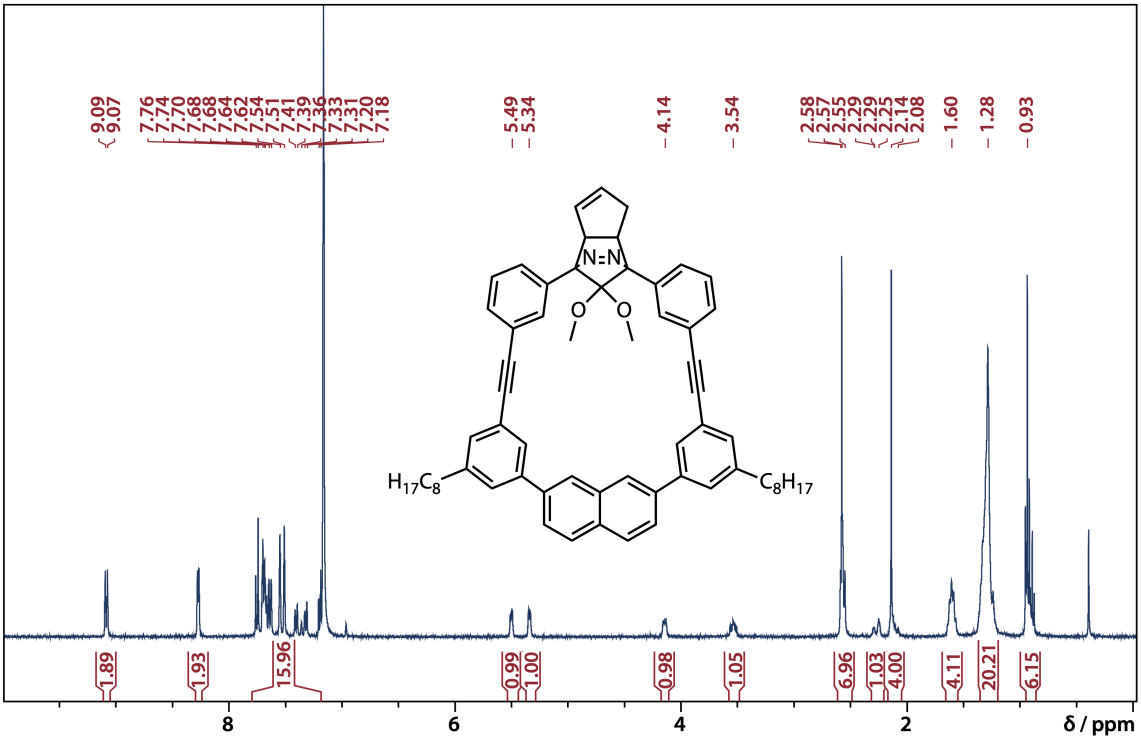

Figure S2.1 ^{1}H NMR spectrum of **AZ2d** (C_6D_6, 400 MHz).

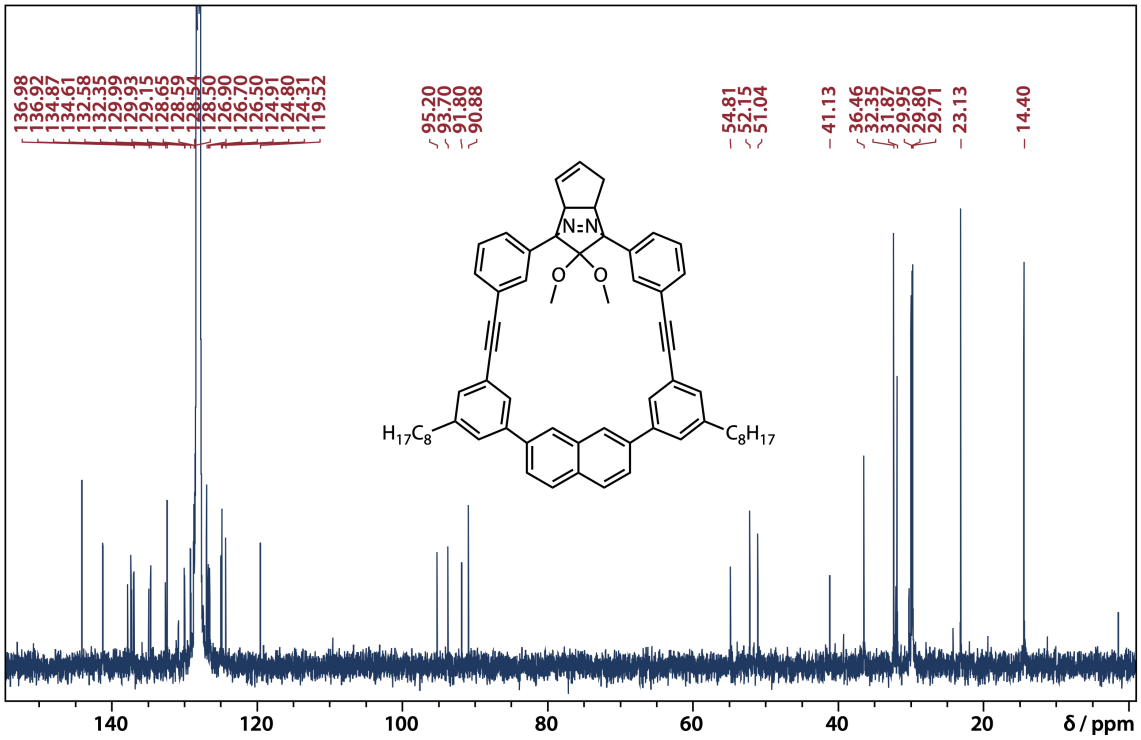

Figure S2.2 ^{13}C NMR spectrum of **AZ2d** (C_6D_6, 100 MHz).

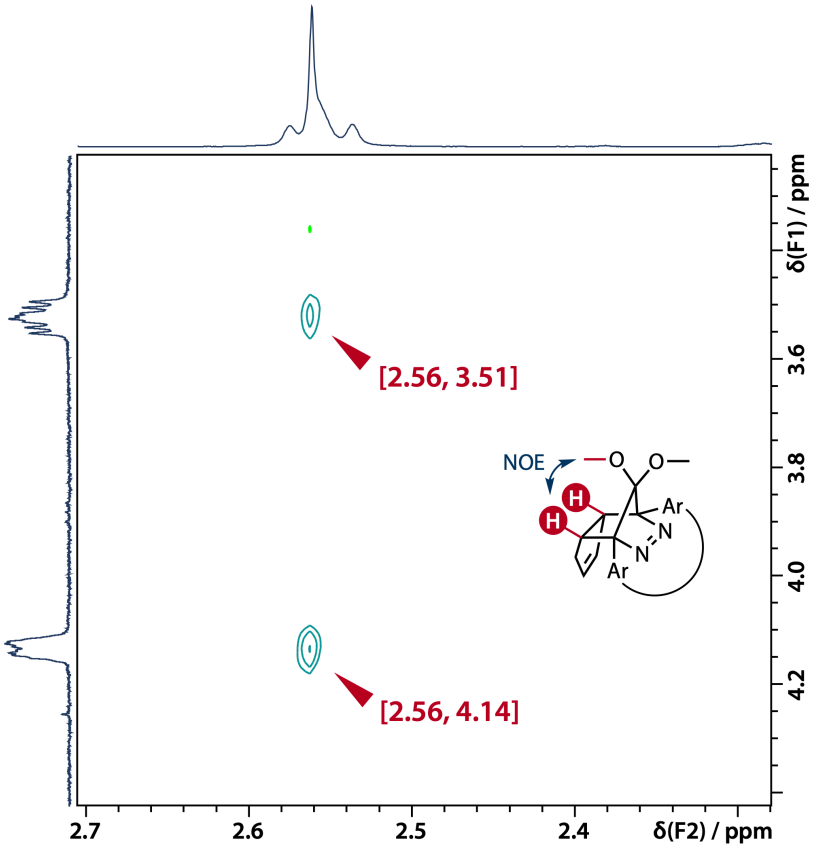

Figure S2.3 2D NOESY NMR spectrum of **AZ2d** (C_6D_6, 400 MHz).

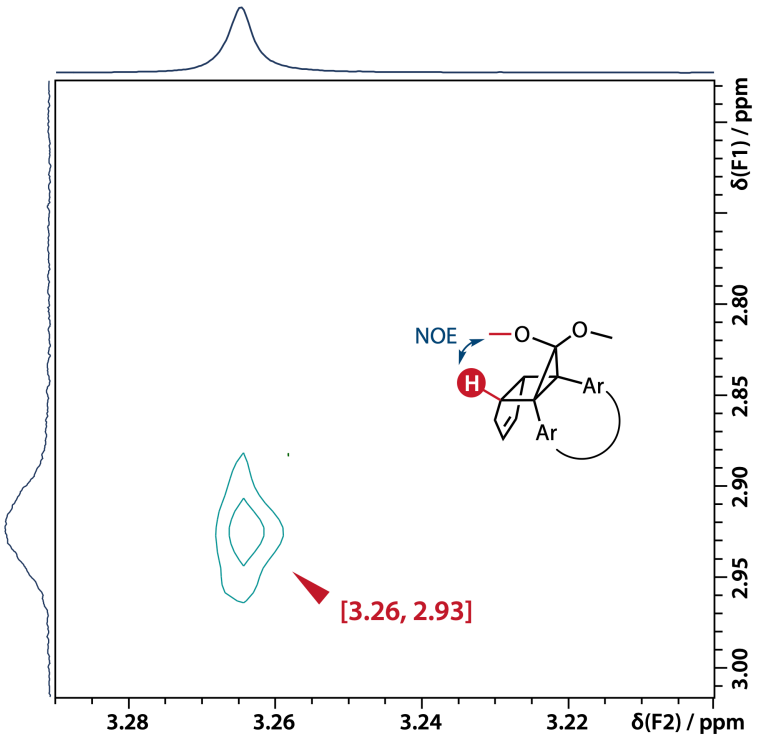

Figure S2.4 2D NOESY NMR spectrum of *trans*-**CP2d** (C_6D_6, 400 MHz).

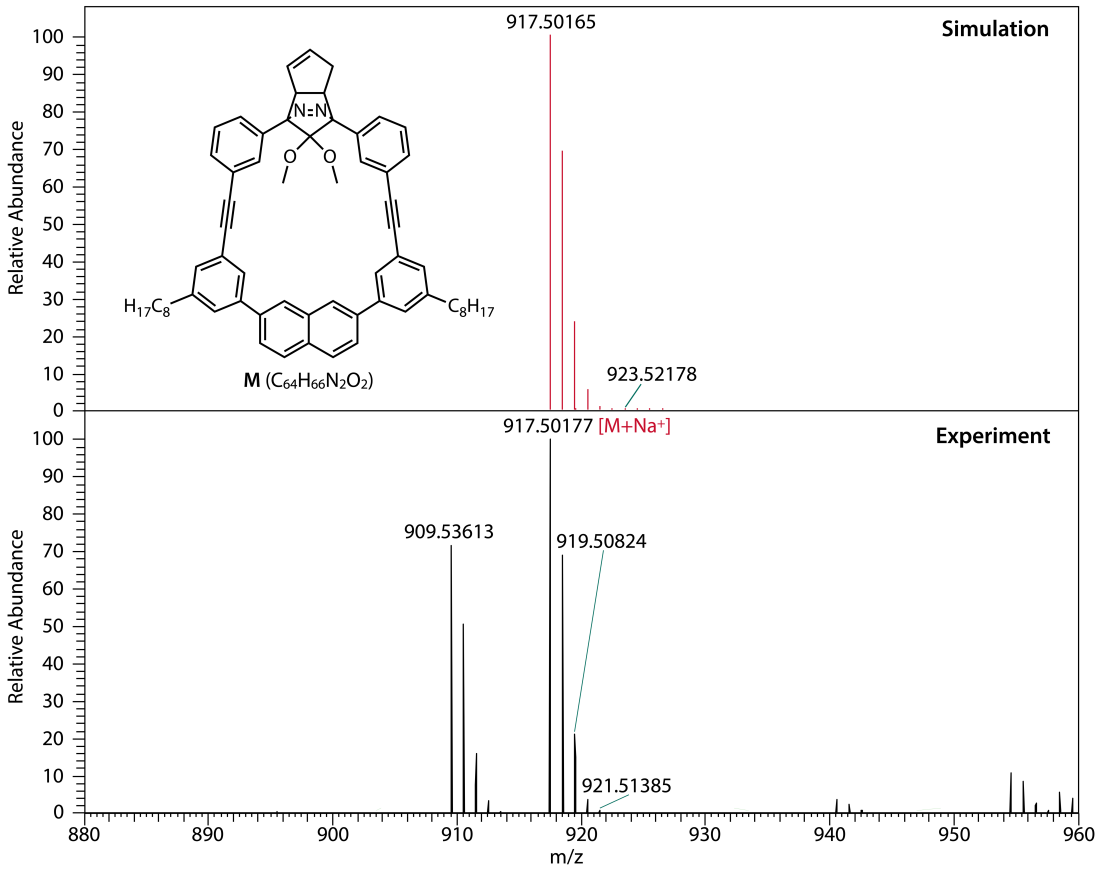

Figure S2.5 High resolution mass spectrum (ESI) of **AZ2d**.

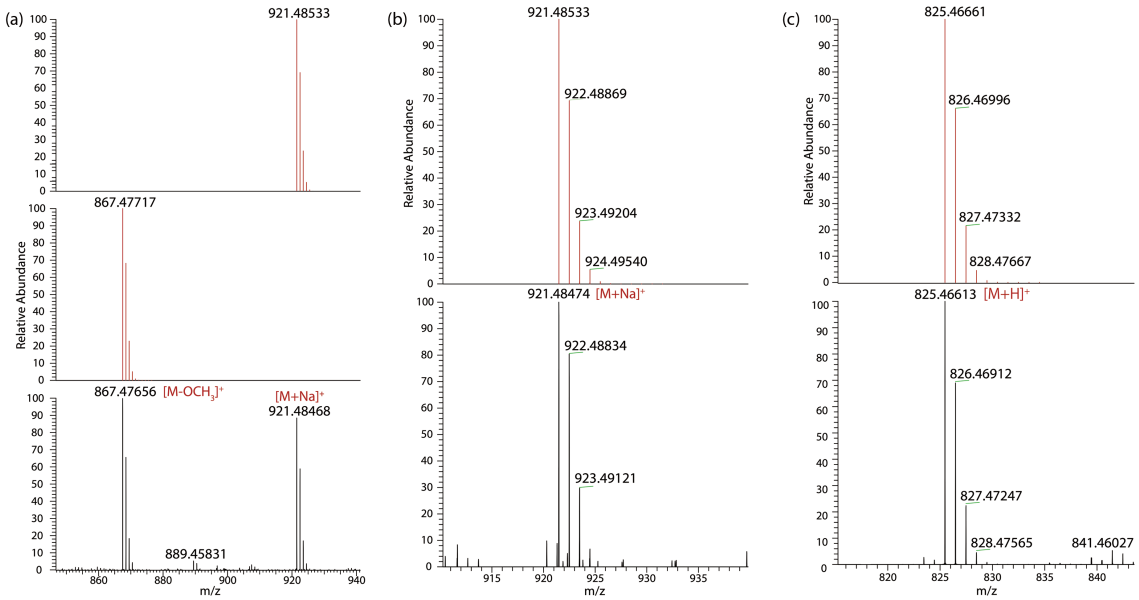

Figure S2.6 High resolution mass spectra of (a) **11** (ESI, found $[M–OCH_3]^+$ and $[M+Na]^+$), (b) **12** (ESI, found $[M+Na]^+$) and (c) **13** (APCI, found $[M+H]^+$).

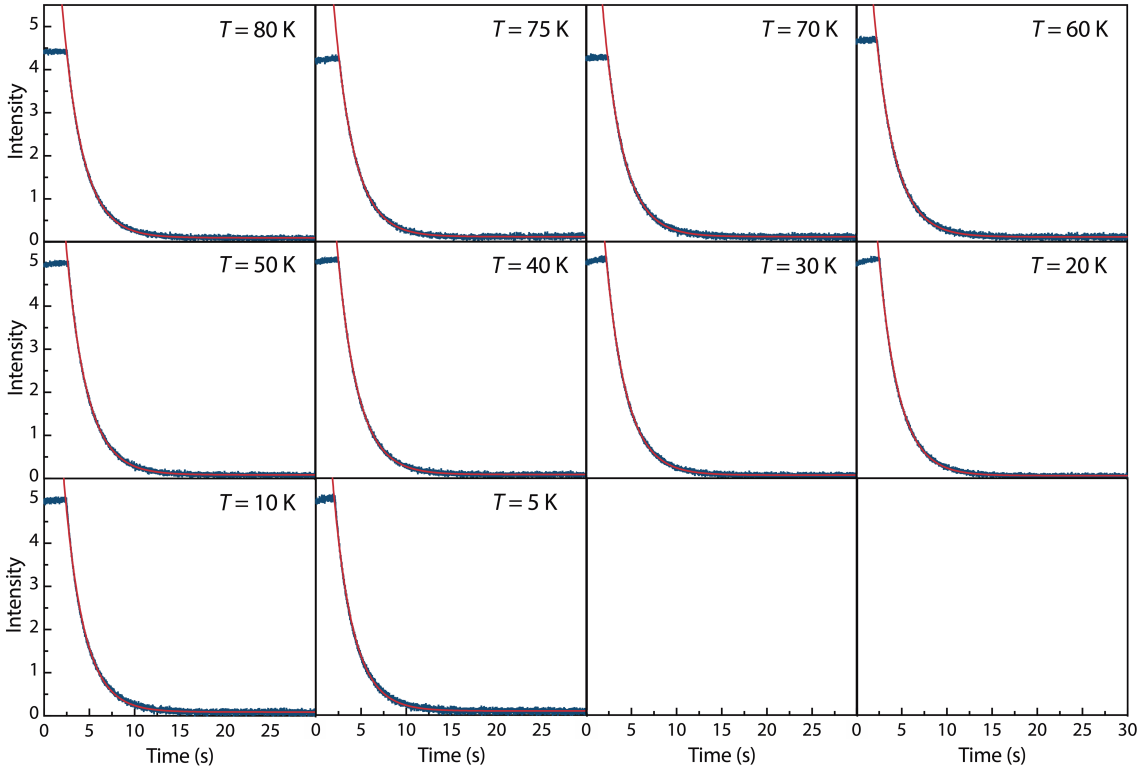

Figure S2.7 EPR time profile monitored at 1562 G at 5–80 K.

2.4.4 Time-Resolved Transient Absorption Spectroscopy

Table S2.1 Activation parameters (E_a, log A, $\Delta H^{\ddagger}$, $\Delta S^{\ddagger}$, $\Delta G^{\ddagger}_{293}$) of ring-closing processes for S-**DR1** determined by Arrhenius and Eyring plots.

Solvent	E_a / kJ mol^{-1}	log (A / s^{-1})	$\Delta H^{\ddagger}$ / kJ mol^{-1}	$\Delta S^{\ddagger}$ / J mol^{-1} K^{-1}	$\Delta G^{\ddagger}_{293}$ / kJ mol^{-1}
Triacetin	51.9 ± 1.5	15.5 ± 0.4	49.3 ± 1.5	42.4 ± 4.9	37.0 ± 1.5
$CHCl_3$	34.1 ± 1.1	12.5 ± 0.2	31.7 ± 1.1	–13.7 ± 3.1	35.8 ± 1.1
DMSO	40.2 ± 1.2	13.5 ± 0.2	37.6 ± 1.2	4.7 ± 2.8	36.2 ± 1.2
CH_2ClCH_2Cl	28.8 ± 1.2	11.7 ± 0.2	26.4 ± 1.2	–29.9 ± 4.0	35.2 ± 1.2
CH_2Cl_2	32.9 ± 0.2	12.4 ± 0.1	30.7 ± 0.2	–15.3 ± 0.8	35.1 ± 0.2
1,4-Dioxane	34.5 ± 1.0	12.7 ± 0.2	31.9 ± 1.0	–10.0 ± 3.3	34.8 ± 1.0
Acetone	37.8 ± 0.5	13.4 ± 0.1	35.4 ± 0.5	2.8 ± 1.9	34.6 ± 0.5
Benzene	30.5 ± 0.4	12.1 ± 0.1	28.0 ± 0.4	−21.5 ± 0.8	34.2 ± 0.8
CCl_4	33.1 ± 0.6	12.7 ± 0.1	30.7 ± 0.6	−11.2 ± 2.1	34.0 ± 0.6
EtOAc	32.7 ± 0.9	12.5 ± 0.2	30.3 ± 0.9	−14.0 ± 3.1	34.4 ± 0.9
Toluene	33.5 ± 1.0	12.7 ± 0.2	31.0 ± 1.1	−11.1 ± 3.6	34.3 ± 1.1
Ether	29.6 ± 0.5	12.1 ± 0.1	27.3 ± 0.5	−21.0 ± 1.8	33.4 ± 0.5
Hexane	29.3 ± 0.8	12.2 ± 0.2	26.9 ± 0.8	−18.7 ± 3.0	32.4 ± 0.8

Table S2.2 Activation parameters (E_a, log A, $\Delta H^{\ddagger}$, $\Delta S^{\ddagger}$, $\Delta G^{\ddagger}_{293}$) of ring-closing processes for S-**DR2d** determined by Arrhenius and Eyring plots.

Solvent	E_a / kJ mol^{-1}	log (A / s^{-1})	$\Delta H^{\ddagger}$ / kJ mol^{-1}	$\Delta S^{\ddagger}$ / J mol^{-1} K^{-1}	$\Delta G^{\ddagger}_{293}$ / kJ mol^{-1}
Triacetin	72.0 ± 0.9	16.2 ± 0.2	69.6 ± 0.9	57.5 ± 0.8	52.7 ± 0.9
Benzene	58.4 ± 1.1	14.2 ± 0.2	56.0 ± 1.1	18.1 ± 2.3	50.7 ± 1.1
Toluene	59.9 ± 2.0	14.6 ± 0.4	57.4 ± 2.0	26.5 ± 2.7	49.7 ± 2.0
EtOAc	54.8 ± 1.7	13.9 ± 0.3	52.4 ± 1.7	13.9 ± 2.9	48.3 ± 1.7
1,4-Dioxane	59.0 ± 1.1	14.7 ± 0.2	56.5 ± 1.1	28.4 ± 1.8	48.2 ± 1.1
Ether	52.3 ± 2.1	13.7 ± 0.4	49.9 ± 2.1	8.5 ± 3.2	47.5 ± 2.1
Acetone	57.2 ± 2.7	14.7 ± 0.5	54.8 ± 2.7	29.0 ± 4.3	46.3 ± 2.7

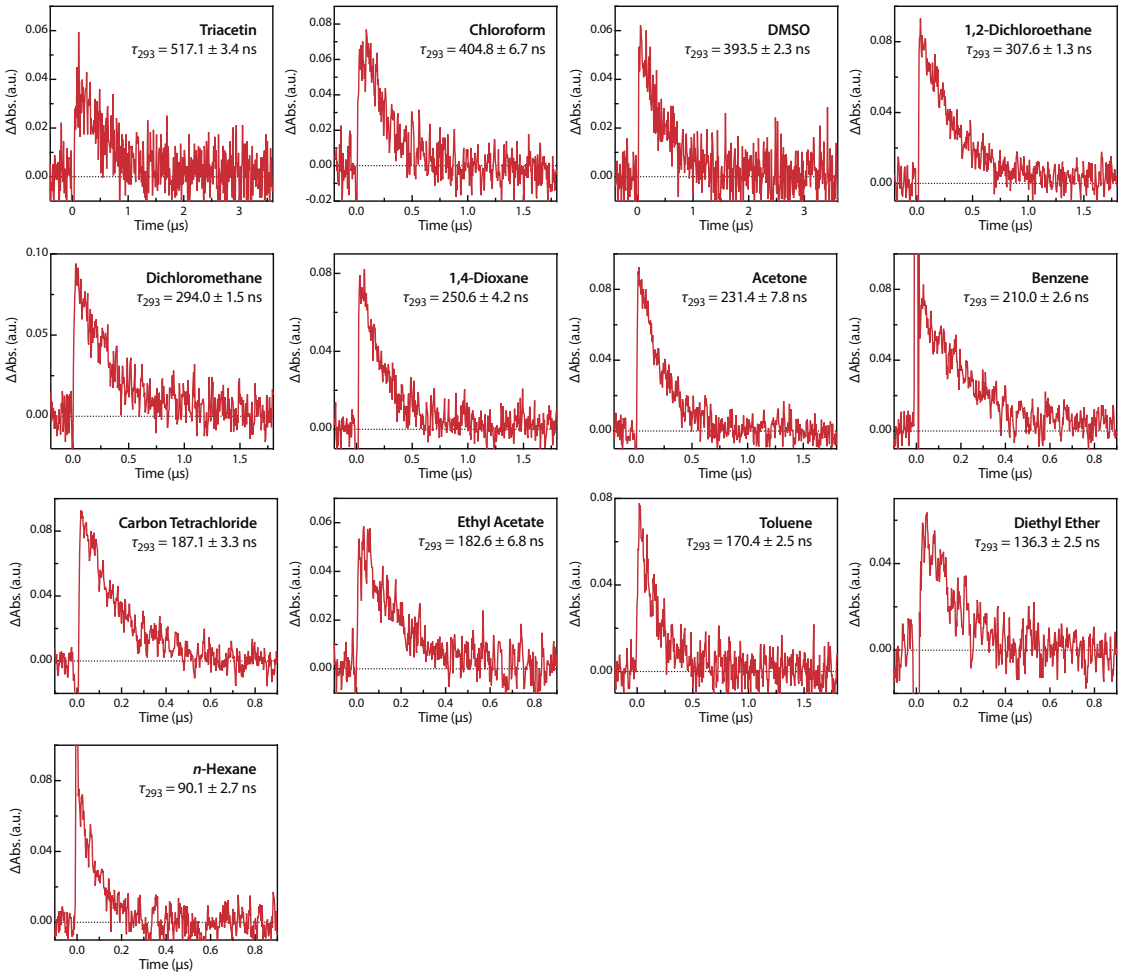

Figure S2.8 Decay profile monitored at 570−580 nm of S-**DR1** at 293 K in triacetin, chloroform, DMSO, 1,2-dichloroethane, dichloromethane, 1,4-dioxane, acetone, benzene, carbon tetrachloride, ethyl acetate, toluene, diethyl ether and *n*-hexane. Lifetime were calculated by fitting with single-exponential decay model.

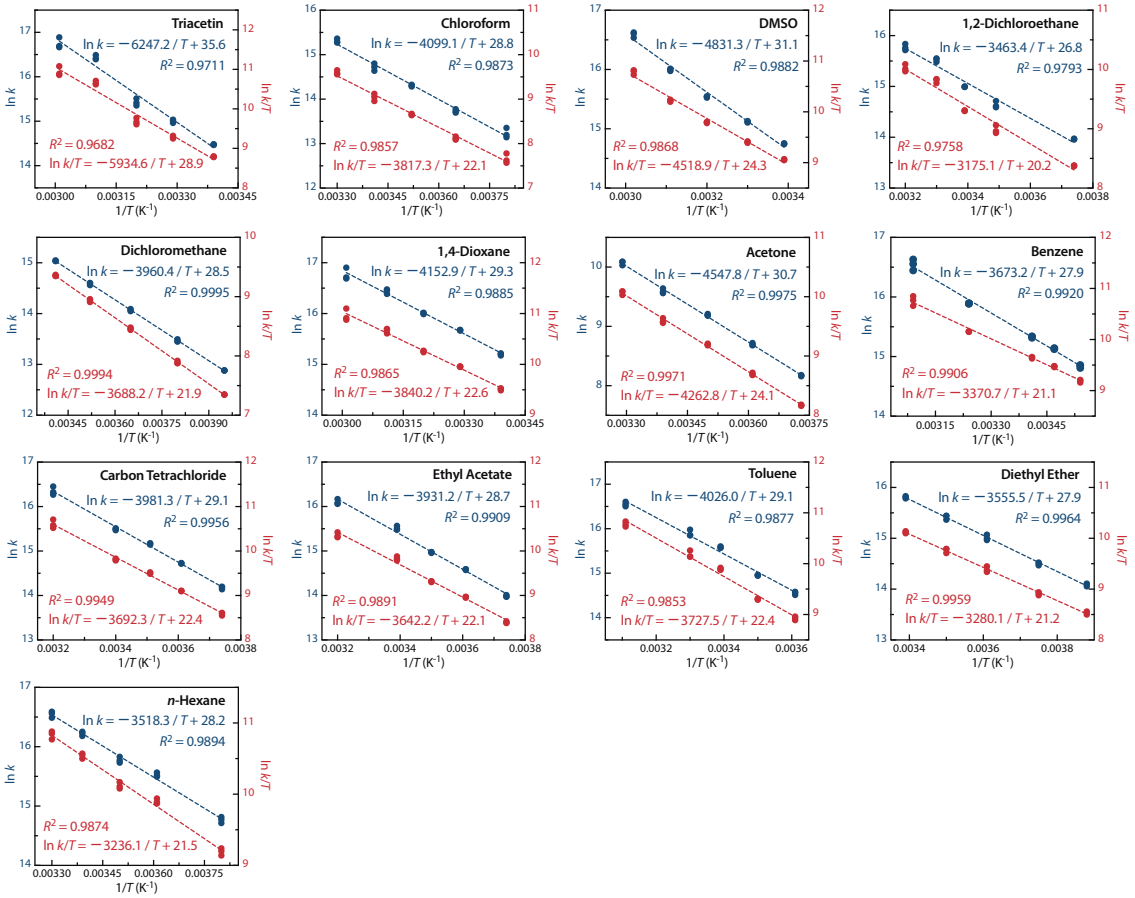

Figure S2.9 Arrhenius plots (left *y* axis, blue line) and Eyring plots (right *y* axis, red line) for the decay processes of S-**DR1** in triacetin, chloroform, DMSO, 1,2-dichloroethane, dichloromethane, 1,4-dioxane, acetone, benzene, carbon tetrachloride, ethyl acetate, toluene, diethyl ether and *n*-hexane.

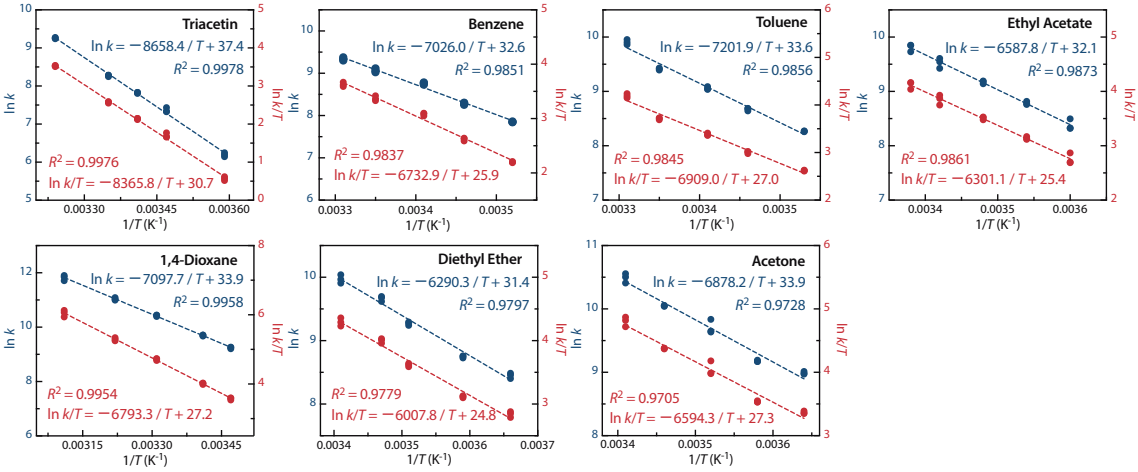

Figure S2.10 Arrhenius plots (left *y* axis, blue line) and Eyring plots (right *y* axis, red line) for the decay processes of S-**DR2d** in triacetin, benzene, toluene, ethyl acetate, 1,4-dioxane, diethyl ether and acetone.

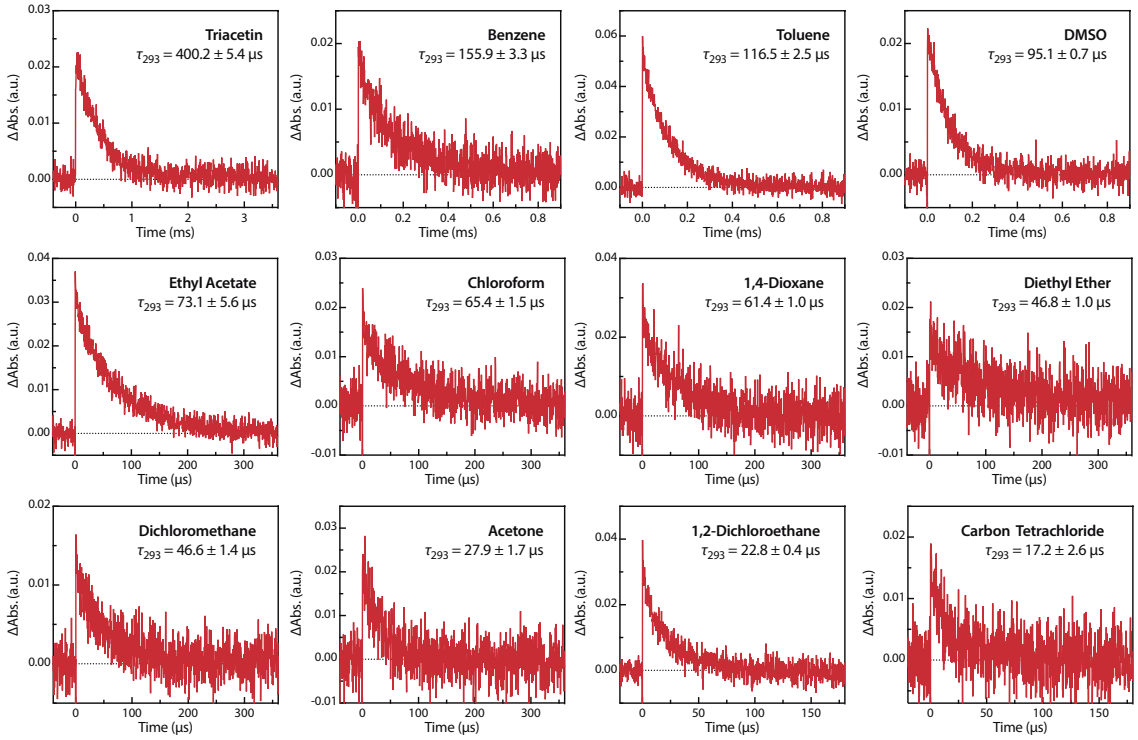

Figure S2.11 Decay profile monitored at 580 nm of S-**DR2d** at 293 K in triacetin, benzene, toluene, DMSO, ethyl acetate, chloroform, 1,4-dioxane, diethyl ether, dichloromethane, acetone, 1,2-dichloroethane and carbon tetrachloride. Lifetime were calculated by fitting with single-exponential decay model.

2.4.5 Computational Details

Quantum chemical computations in gas phase have been performed with the *Gaussian 16* (Revision. B.01) suite of programs. *GaussView 6.0.16*[46] was used for visualization.

Zero-filed splitting (*zfs*) parameters (*D* tensor and *E*/*D* ratio) calculation were performed with ORCA 5.0.3 program at B3LYP/EPR-II level of theory. In all *zfs* calculations, the resolution of identity and chain of spheres approximation[47,48] (*RIJCOSX*) and the automatic auxiliary basis sets[49] (*AutoAux*) were used. Demo calculations with B3LYP/EPR-III, BP86/EPR-II, BP86/EPR-III and CASSCF(2,2)/def2-SVP[50] level let to comparable results. The *D* tensor calculation included the spin-spin and the spin-orbit components (SSANDSO).

Energy profiles (Figure 2.10 and Figure 3.5, *vide infra*) were plotted with self-made program EnePro.[51] Computed UV-vis spectrum (Figure 2.23) was exported by self-made program uv.**Plotter**.[52] Absorption peaks assume

a Gaussian-type band shape, broadened using oscillator strength of the computed excited states (equation S1).

$$\varepsilon(\tilde{\nu}) = \sum_{i=1}^{n} \varepsilon_i(\tilde{\nu}) = \sum_{i=1}^{n} \left(\frac{\sqrt{\pi} \cdot e^2 \cdot N}{1000 \cdot \ln 10 \cdot c^2 \cdot m_e} \cdot \frac{f_i}{\sigma} \exp \left[-\left(\frac{\tilde{\nu} - \tilde{\nu}_i}{\sigma} \right)^2 \right] \right) \quad \text{(S1)}$$

where,

- ε is molar extinction coefficient in L mol^{-1} cm^{-1};
- e = 4.803204 × 10^{-10} esu, is the charge on the electron;
- N = 6.02214199 × 10^{23} mol^{-1}, is the Avogadro's number;
- c = 29979245800.0 cm s^{-1}, is the speed of light;
- m_e = 9.10938 × 10^{-31} kg, is the electron mass;
- f_i is the oscillator strength from TD-DFT output;
- σ is the standard deviation in wavenumbers, which related to the width of the simulated band. In this study, σ = 0.4 eV = 10^{-7}/3099.6 cm^{-1}.
- $\tilde{\nu}_i$ is the excitation energy (in wavenumber) corresponding to the electronic excitation of interest.

2.5 References

1 M. Abe and R. Akisaka, Is π-single bonding (C–π–C) possible? A challenge in organic chemistry, *Chem. Lett.*, **2017**, *46*, 1586–1592.

2 T. Nukazawa and T. Iwamoto, An isolable tetrasilicon analogue of a planar bicyclo[1.1.0]butane with π-type single-bonding character, *J. Am. Chem. Soc.*, **2020**, *142*, 9920–9924.

3 A. Rodriguez, R. A. Olsen, N. Ghaderi, D. Scheschkewitz, F. S. Tham, L. J. Mueller and G. Bertrand, Evidence for the coexistence of two bond-stretch isomers in solution, *Angew. Chem. Int. Ed.*, **2004**, *43*, 4880–4883.

4 P. Henke, T. Pankewitz, W. Klopper, F. Breher and H. Schnöckel, Snapshots of the Al–Al σ-bond formation starting from $\{AlR_2\}$ units: experimental and computational observations, *Angew. Chem. Int. Ed.*, **2009**, *48*, 8141–8145.

5 M. Abe, Diradicals, *Chem. Rev.*, **2013**, *113*, 7011–7088.

6 M. Abe, J. Ye and M. Mishima, The chemistry of localized singlet 1,3-diradicals (biradicals): from putative intermediates to persistent species and unusual molecules with a π-single bonded character, *Chem. Soc. Rev.*, **2012**, *41*, 3808–3820.

7 M. Abe, W. Adam and W. M. Nau, Photochemical generation and methanol trapping of localized 1,3 and 1,4 singlet diradicals derived from a spiroepoxy-substituted cyclopentane-1,3-diyl, *J. Am. Chem. Soc.*, **1998**, *120*, 11304–11310.

8 W. Adam, W. T. Borden, C. Burda, H. Foster, T. Heidenfelder, M. Heubes, D. A. Hrovat, F. Kita, S. B. Lewis, D. Scheutzow and J. Wirz, Transient spectroscopy of a derivative of 2,2-difluoro-1,3-diphenylcyclopentane-1,3-diyl – A persistent localized singlet 1,3-diradical, *J. Am. Chem. Soc.*, **1998**, *120*, 593–594.

9 M. Abe, W. Adam, T. Heidenfelder, W. M. Nau and X. Zhang, Intramolecular and intermolecular reactivity of localized singlet diradicals: the exceedingly long-lived 2,2-diethoxy-1,3-diphenyl-cyclopentane-1,3-diyl, *J. Am. Chem. Soc.*, **2000**, *122*, 2019–2026.

10 T. Nakagaki, T. Sakai, T. Mizuta, Y. Fujiwara and M. Abe, Kinetic stabilization and reactivity of p single-bonded species: effect of the alkoxy group on the lifetime of singlet 2,2-dialkoxy-1,3-

diphenyloctahydropentalene-1,3-diyls, *Chem. Eur. J.*, **2013**, *19*, 10395–10404.

11 J. Ye, Y. Fujiwara and M. Abe, Substituent effect on the energy barrier for σ-bond formation from π-single-bonded species, singlet 2,2-dialkoxycyclopentane-1,3-diyls, *Beilstein J. Org. Chem.*, **2013**, *9*, 925–933.

12 M. Abe, E. Kubo, K. Nozaki, T. Matsuo and T. Hayashi, An extremely long-lived singlet 4,4-dimethoxy-3,5-diphenylpyrazolidine-3,5-diyl derivative: a notable nitrogen-atom effect on intra- and intermolecular reactivity, *Angew. Chem. Int. Ed.*, **1006**, *45*, 7828–7831.

13 S. Yoshidomi, M. Mishima, S. Seyama, M. Abe, Y. Fujiwara and T. Ishibashi, Direct detection of a chemical equilibrium between a localized singlet diradical and its s-bonded species by time-resolved UV/Vis and IR spectroscopy, *Angew. Chem. Int. Ed.*, **2017**, *56*, 2984–2988.

14 S. Yoshidomi and M. Abe, 1,2-Diazacyclopentane-3,5-diyl diradicals: electronic structure and reactivity, *J. Am. Chem. Soc.*, **2019**, *141*, 3920–3933.

15 R. Akisaka and M. Abe, Bulky substituent effect on reactivity of localized singlet cyclopentane-1,3-diyl with π-single bonding (C–π–C) character, *Chem. Asian J.*, **2019**, *14*, 4223–4228.

16 M, Abe, H. Furunaga, D. Ma, L. Gagliardi and G. J. Bodwell, Stretch effects induced by molecular strain on weakening σ-bonds: molecular design of long-lived diradicals (biradicals), *J. Org. Chem.*, **2012**, *77*, 7612–7619.

17 Y. Harada, Z. Wang, S. Kumashiro, S. Hatano and M. Abe, Extremely long lived localized singlet diradicals in a macrocyclic structure: a case study on the stretch effect, *Chem. Eur. J.*, **2018**, *24*, 14808–14815.

18 J. Chai and M. Head-Gordon, Long-range corrected hybrid density functionals with damped atom–atom dispersion corrections, *Phys. Chem. Chem. Phys.*, **2008**, *10*, 6615–6620.

19 W. J. Hehre, R. Ditchfield and J. A. Pople, Self–consistent molecular orbital methods. XII. Further extensions of Gaussian–type basis sets for use in molecular orbital studies of organic molecules, *J. Chem.*

Phys., **1972**, *56*, 2257–2261.

20 P. C. Hariharan and J. A. Pople, The influence of polarization functions on molecular orbital hydrogenation energies, *Theor. Chim. Acta*, **1973**, *28*, 213–222.

21 *Gaussian 16, Revision B.01*, M. J. Frisch, G. W. Trucks, H. B. Schlegel, G. E. Scuseria, M. A. Robb, J. R. Cheeseman, G. Scalmani, V. Barone, G. A. Petersson, H. Nakatsuji, X. Li, M. Caricato, A. V. Marenich, J. Bloino, B. G. Janesko, R. Gomperts, B. Mennucci, H. P. Hratchian, J. V. Ortiz, A. F. Izmaylov, J. L. Sonnenberg, D. Williams-Young, F. Ding, F. Lipparini, F. Egidi, J. Goings, B. Peng, A. Petrone, T. Henderson, D. Ranasinghe, V. G. Zakrzewski, J. Gao, N. Rega, G. Zheng, W. Liang, M. Hada, M. Ehara, K. Toyota, R. Fukuda, J. Hasegawa, M. Ishida, T. Nakajima, Y. Honda, O. Kitao, H. Nakai, T. Vreven, K. Throssell, J. A. Montgomery, Jr., J. E. Peralta, F. Ogliaro, M. J. Bearpark, J. J. Heyd, E. N. Brothers, K. N. Kudin, V. N. Staroverov, T. A. Keith, R. Kobayashi, J. Normand, K. Raghavachari, A. P. Rendell, J. C. Burant, S. S. Iyengar, J. Tomasi, M. Cossi, J. M. Millam, M. Klene, C. Adamo, R. Cammi, J. W. Ochterski, R. L. Martin, K. Morokuma, O. Farkas, J. B. Foresman, and D. J. Fox, Gaussian, Inc., Wallingford CT, **2016**.

22 K. Yamaguchi, F. Jensen, A. Dorigo and K. N. Houk, A spin correction procedure for unrestricted Hartree-Fock and Møller-Plesset wavefunctions for singlet diradicals and polyradicals, *Chem. Phys. Lett.*, **1988**, *149*, 537–542.

23 B. O. Roos, P. R. Taylor and P. E. M. Siegbahn, A complete active space SCF method (CASSCF) using a density matrix formulated super-CI approach, *Chem. Phys.*, **1980**, *48*, 157–173.

24 A. D. Becke, Density-functional thermochemistry. III. The role of exact exchange, *J. Chem. Phys.*, **1993**, *98*, 5648–5652.

25 T. Yanai, D. P. Tew and N. C. Handy, A new hybrid exchange–correlation functional using the Coulomb-attenuating method (CAM-B3LYP), *Chem. Phys. Lett.*, **2004**, *393*, 51–57.

26 Y. Zhao and D. G. Truhlar, The M06 suite of density functionals for main group thermochemistry, thermochemical kinetics, noncovalent interactions, excited states, and transition elements: two new

functionals and systematic testing of four M06-class functionals and 12 other functionals, *Theor. Chem. Acc.*, **2008**, *120*, 215–241.
27 J. Chai and M. Head-Gordon, Systematic optimization of long-range corrected hybrid density functionals, *J. Chem. Phys.*, **2008**, *128*, 084106.
28 A. Austin, G. A. Petersson, M. J. Frisch, F. J. Dobek, G. Scalmani and K. Throssell, A density functional with spherical atom dispersion terms, *J. Chem. Theory Comput.*, **2012**, *8*, 4989–5007.
29 T. Nakagawa, K. Okamoto, H. Hanada and R. Katoh, Probing with randomly interleaved pulse train bridges the gap between ultrafast pump-probe and nanosecond flash photolysis, *Opt. Lett.*, **2016**, *41*, 1498–1501.
30 *Handbook of Photochemistry*, M. Montalti, A. Credi, L. Prodi and M. T. Gandolfi, CRC Press, Baco Raton, **2006**.
31 F. D. Coms and D. A. Dougherty, 1,3-Diphenyl-1,3-cyclopentanediyl: A remarkably stable localized biradical, *Tetrahedron Lett.*, **1988**, *29*, 3753–3756.
32 F. Neese, The ORCA program system, *Wiley Interdiscip. Rev.: Comput. Mol. Sci.*, **2012**, *2*, 73–78.
33 F. Neese, Software update: the ORCA program system, version 4.0, *Wiley Interdiscip. Rev.: Comput. Mol. Sci.*, **2018**, *8*, e1327.
34 A. D. Becke, Density-functional exchange-energy approximation with correct asymptotic behavior, *Phys. Rev. A*, **1998**, *38*, 3098–3100.
35 V. Barone, in *Recent Advances in Density Functional Methods*, *Part I*, ed. D. P. Chong, World Scientific Publ. Co., Singapore, **1996**.
36 M. J. Kamlet, J. M. Abboud and R. W. Taft, The solvatochromic comparison method. 6. The π* scale of solvent polarities, *J. Am. Chem. Soc.*, **1977**, *99*, 6027–6038.
37 C. Laurence, P. Nicolet, M. T. Dalati, J. M. Abboud and R. Notario, The empirical treatment of solvent-solute interactions: 15 years of π*, *J. Phys. Chem.*, **1994**, *98*, 5807–5816.
38 C. Reichardt, Solvatochromic dyes as solvent polarity indicators, *Chem. Rev.*, **1994**, *94*, 2319–2358.
39 C. Reichardt and T. Welton, *Solvents and Solvent Effects in Organic Chemistry*, Wiley-VCH, Weinheim, **2011**.

40 H. Sumi, Theory on reaction rates in nonthermalized steady states during conformational fluctuations in viscous solvents, *J. Phys. Chem.*, **1991**, *95*, 3334–3350.
41 T. Asano, H. Furuta and H. Sumi, Two-step mechanism in single-step isomerizations. Kinetics in a highly viscous liquid phase, *J. Am. Chem. Soc.*, **1994**, *116*, 5545–5550.
42 T. Asano, Kinetics in highly viscous solutions: dynamic solvent effects in 'slow' reactions, *Pure Appl. Chem.*, **1999**, *71*, 1691–1704.
43 R. M. Gulam, T. Takahashi and Y. Ohga, Dynamic solvent effects on the thermal isomerization of zinc dithizonate, *Phys. Chem. Chem. Phys*., **2009**, *11*, 5170–5174.
44 R. Akisaka, Y. Ohga and M. Abe, Dynamic solvent effects in radical–radical coupling reactions: an almost bottleable localised singlet diradical, *Phys. Chem. Chem. Phys.*, **2020**, *22*, 27949–27954.
45 J. C. M. Kistemaker, A. S. Lubbe, E. A. Bloemsma and B. L. Feringa, On the role of viscosity in the Eyring equation, *ChemPhysChem*, **2016**, *17*, 1819–1822.
46 R. Dennington, T. A. Keith and J. M. Millam, *GaussView*, *Version 6.0.16*, Semichem Inc., Shawnee Mission KS, **2016**.
47 R. Izask and F. Neese, An overlap fitted chain of spheres exchange method, *J. Chem. Phys*., **2011**, *135*, 144105.
48 F. Neese, F. Wennmohs, A. Hansen and U. Becker, Efficient, approximate and parallel Hartree–Fock and hybrid DFT calculations. A 'chain-of-spheres' algorithm for the Hartree–Fock exchange, *Chem. Phys*., **2009**, *356*, 98–109.
49 F. Weigend, Hartree–Fock exchange fitting basis sets for H to Rn, *J. Comput. Chem*., **2008**, *29*, 167–175.
50 A. Schäfer, H. Horn and R. Ahlrichs, Fully optimized contracted Gaussian basis sets for atoms Li to Kr, *J. Chem. Phys*., **1992**, *97*, 2571–2577.
51 Z. Wang, *EnePro*, v1.6.2, https://github.com/wongzit/EnePro, **2021**.
52 Z. Wang, *uv.Plotter*, v1.0.0, https://wongzit.github.io/program/uvplotter, **2022**.

Chapter 3.

SOMO–HOMO Conversion in Triplet Cyclopentane-1,3-Diyl Diradicals

3.1 Chapter Introduction

The ground state electronic configuration depends on the Pauli exclusion principle, Hund's rule and Aufbau principle. According to the Aufbau principle, in the ground state of a molecule (or atom), electrons fill the electronic shell of the lowest available energy, then fill the shell of higher energy. So, the singly occupied molecular orbitals (SOMO) are energetically higher than the doubly occupied molecular orbitals (DOMO). For example, in a triphenylmethyl radical (**TPM**, $Ph_3C\cdot$), which was reported by Gomberg in 1900[1], the SOMO contains one unpaired electron has higher orbital energy than the highest occupied molecular orbital (HOMO) (Figure 3.1a). Other derivatives like tris(2,4,6-trichlorophenyl)-methyl radicals (**TTM**) also follow the Aufbau principle, although its SOMO energy decreased due to the electron withdrawing chloro-substituents (Figure 3.1b).

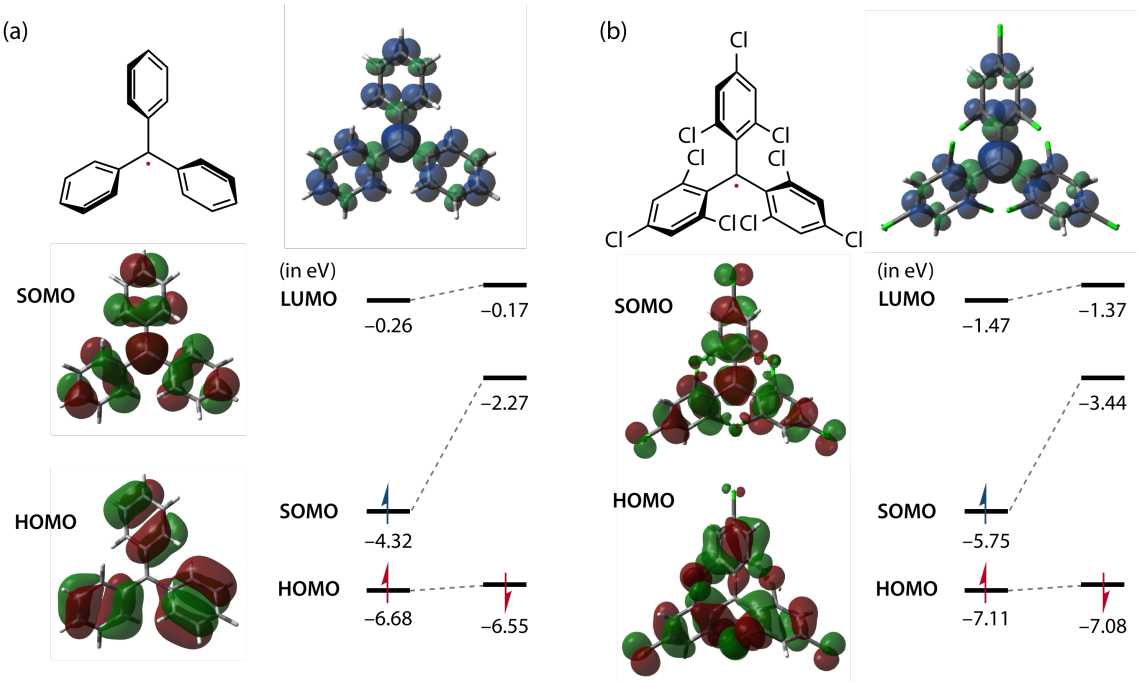

Figure 3.1 Chemical structures, spin density distributions and molecular orbitals diagrams of (a) **TPM** and (b) **TTM**, calculated at (U)B3LYP/6-31G(d) level of theory.

Triphenylamine (**TPA**, Ph_3N) has high HOMO energy as an electron donor. If **TPA** is introduced to one of the phenyl rings of **TTM**, where **TTM** act as an electron acceptor, the HOMO energy of **TPA** (donor) is higher than that of **TTM** (acceptor). Thus, the HOMO of **TPA** becomes the new HOMO

of the new molecule **TTM-TPA**. The HOMO energy of **TPA** is even higher than the SOMO energy of **TTM**. Since the SOMO and HOMO are at separate positions, there is no interaction between these two orbitals, and the change of HOMO does not affect the distribution and energy level of SOMO. Thus, a SOMO–HOMO converted-radical species could be generated (Figure 3.2).

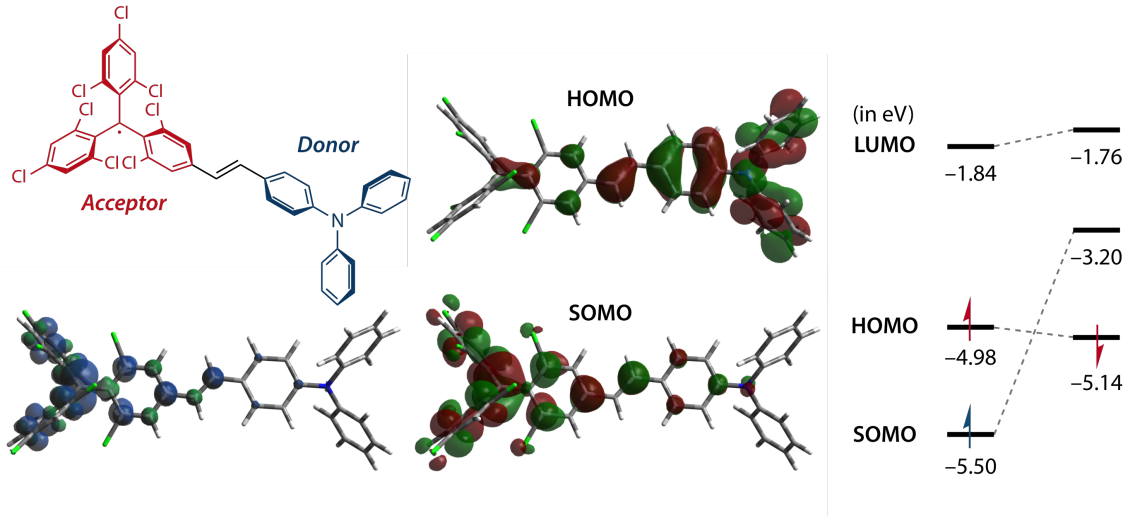

Figure 3.2 Chemical structure, spin density distribution and molecular orbitals diagram of **TTM-TPA**, calculated at (U)B3LYP/6-31G(d) level of theory.

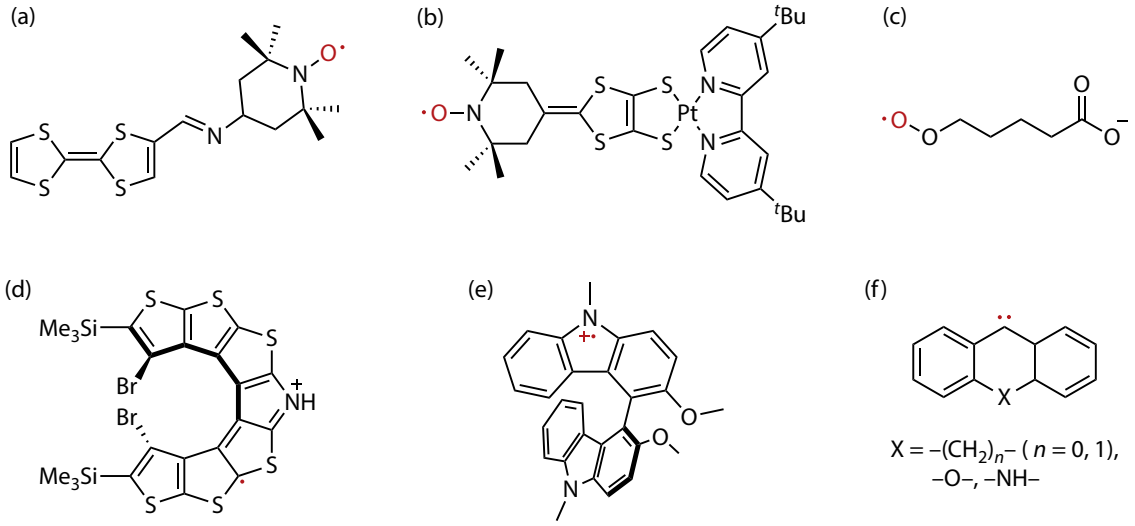

Scheme 3.1 Reported radical species with SOMO–HOMO conversion: (a) Aminoxyl radicals with spin-polarized donor, (b) organometallic complexes, (c) distonic radical anions, (d) Helicene-based radicals, (5) chiral bicarbazole-based radicals and (f) triplet carbenes.

The SOMO–HOMO-converted species have attracted significant concentration due to their unique electronic characteristics. They are expected to switch bond dissociation energy, generate high-spin oxidized species and emit light in the near-infrared region.[2] Recent years, SOMO–HOMO conversion has been reported in aminoxyl radicals, organometallic complexes, distonic radical anions, helicene-based radicals, etc (Scheme 3.1).[3–8] But there is no report on the SOMO–HOMO conversion in carbon-based (multi-)radicals. In this chapter, we provide an approach for molecular design of SOMO–HOMO converted carbon-based triplet diradicals by theoretical computations.

3.2 Results and Discussion

3.2.1 Molecular Orbitals of Triplet Cyclopentane-1,3-Diyl Diradicals

In chapter 2, we discussed the singlet diradicaloids S-**DR1** and S-**DR2c**. The triplet excited states of S-**DR1** and S-**DR2c** followed Aufbau principle. SOMO and SOMO–1 were higher in energies than those of HOMO (Figure 3.3). For T-**DR1**, the HOMO was located on the 1,3-diphenyl groups, which also significantly contribute to the SOMOs. On the other hand, the HOMO of T-**DR2c** was mainly located on the naphthyl moiety, and it did not show a contribution from diradical unit. As SOMOs and HOMO were separated in T-**DR2c**, the change of HOMO should have a negligible influence on SOMO (Figure 3.3b). Thus, SOMO–HOMO conversion could be achieved by modifying the energy level of SOMO (SOMO–1) or/and HOMO.

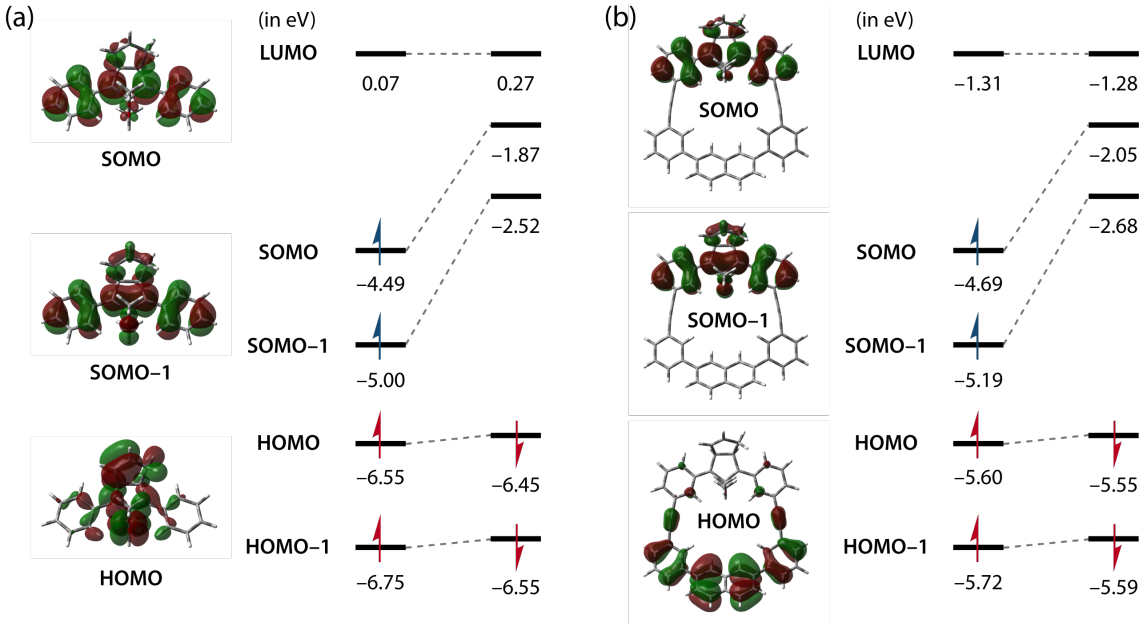

Figure 3.3 Molecular orbital diagrams of (a) T-**DR1** and (b) T-**DR2c** calculated at (U)B3LYP/6-31G(d) level of theory.

3.2.2 Molecular Design of SOMO–HOMO-Converted Triplet Diradicals

As discussed in *Section* 3.2.1, the molecular design of SOMO–HOMO-converted cyclopentane-1,3-diyl diradicals has two possible approaches: (1) decreasing SOMO (SOMO–1) energy or/and (2) increasing HOMO energy. The through-bond interaction between ψ_{TS}^{+} and σ_{CX}* could stabilize the SOMO–1 by introducing electron withdrawing groups like fluoro, alkoxyl,

etc. According to computations at (U)B3LYP/6-31G(d) level of theory using model molecules, the energy level of ψ_{TB}^{+} was stabilized to –5.36 eV, which was 0.28 eV lower than the ψ_{TS}^{+} without through-bond interaction (Figure 3.4). The ψ_{TB}^{-} was generated by the through-bond interaction between ψ_{TS}^{+} with σ_{CX} (X = H or CH_3) in type-II diradicals, and the energy of ψ_{TB}^{-} was destabilized to –4.45 eV, about 0.63 eV higher than the ψ_{TS}^{+}. On the other hand, the ψ_{TS}^{-} has no through-bond interaction with σ_{CX}/σ_{CX}* orbital, and its energy (~–4.60 eV) was almost the same in both type-I and type-II cases.

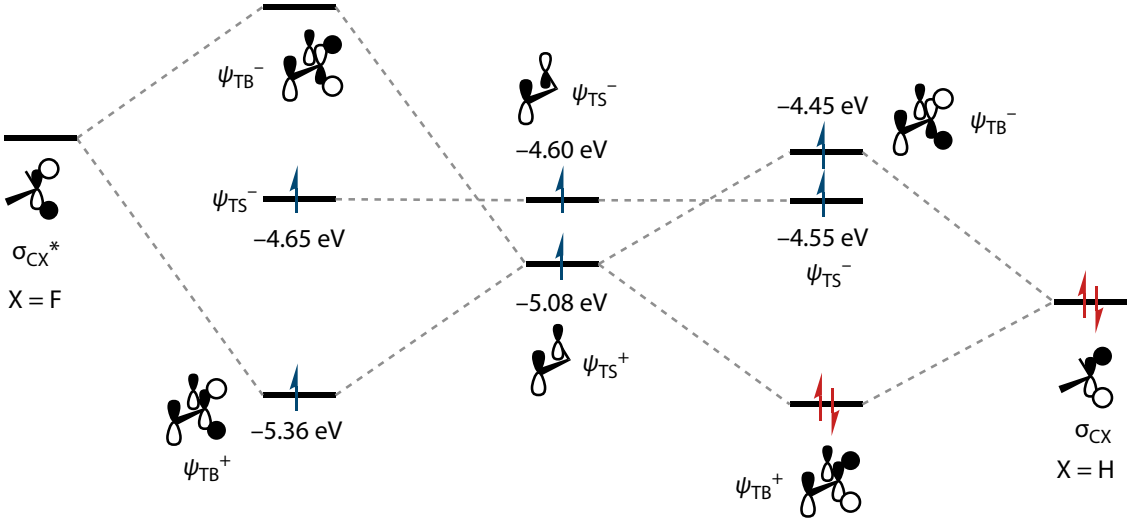

Figure 3.4 Effect of through-bond interaction on the orbital energy of ψ_{TS}^{+}. left: X = F; right: X = H. Orbital energies were computed from triplet 1,3-diphenylcyclopentane-1,3-diyl diradical, triplet 2,2-difluoro-1,3-diphenylcyclopentane-1,3-diyl diradical and triplet 1,4-diphenylbutane-1,4-diyl diradical at (U)B3LYP/6-31G(d) level of theory.

The lowest SOMO–1 energy that could be achieved by through-bond interaction was about –5.36 eV. Thus, a HOMO energy higher than –5.36 eV is necessary, and the HOMO should have little change on the SOMO. It is well-known that the HOMO energies increase with increasing π-conjugation. Thus, acenes could be introduced at the remote position to increase the HOMO energy (Figure 3.5). As we concluded from T-**DR2c**, the SOMOs and HOMO located at separated positions. Thus, introducing acene moiety should have no change on the SOMO energies.

The HOMO and LUMO energies of [*n*]acenes (*n* = 1–10) were computed at (R)B3LYP/6-31G(d) level of theory. As shown in Figure 3.5, the HOMO energies are higher than –5.36 eV when *n* is greater than 3 (anthracene). Based on the computational results, triplet cyclopentane-1,3-

diyl diradicals **DR3X** (X = H, F, Scheme 3.2) with anthracyl moiety at remote position were designed to investigate the SOMO–HOMO conversion.

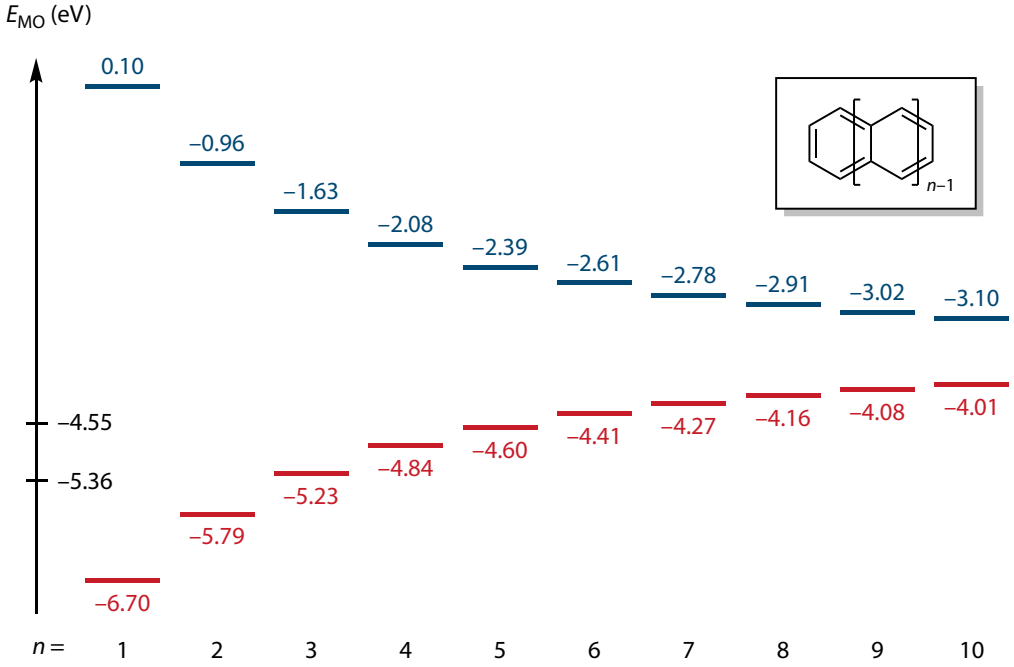

Figure 3.5 HOMO (red) and LUMO (blue) energies of [*n*]acenes (*n* = 1~10), calculated at (R)B3LYP/6-31G(d) level of theory.

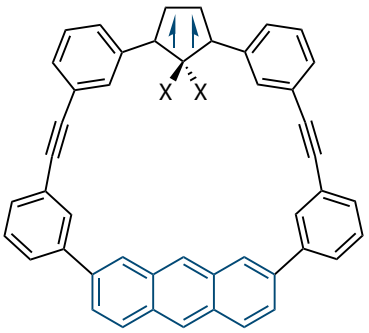

DR3H (X = H)
DR3F (X = F)

Scheme 3.2 Chemical structures of **DR3X**.

3.2.3 SOMO–HOMO Conversion in Macrocyclic Triplet Diradical

The dihydro- and difluoro-substituted **DR2X** (X = H, F) were computed to understand the substituent effect of fluoro groups. Intriguingly, the SOMO–HOMO conversion was not observed in both **DR2H** and **DR2F**, both triplet diradicals displayed conventional electronic configurations that followed the Aufbau principle (Figure 3.6). The HOMO energy was lower than the SOMOs by 1.03 and 0.94 eV in **DR2H**, and the energy differences decreased to 0.83 and 0.12 eV in **DR2F** due to the through-bond interaction stabilized SOMO–1 by fluoro-substituents.

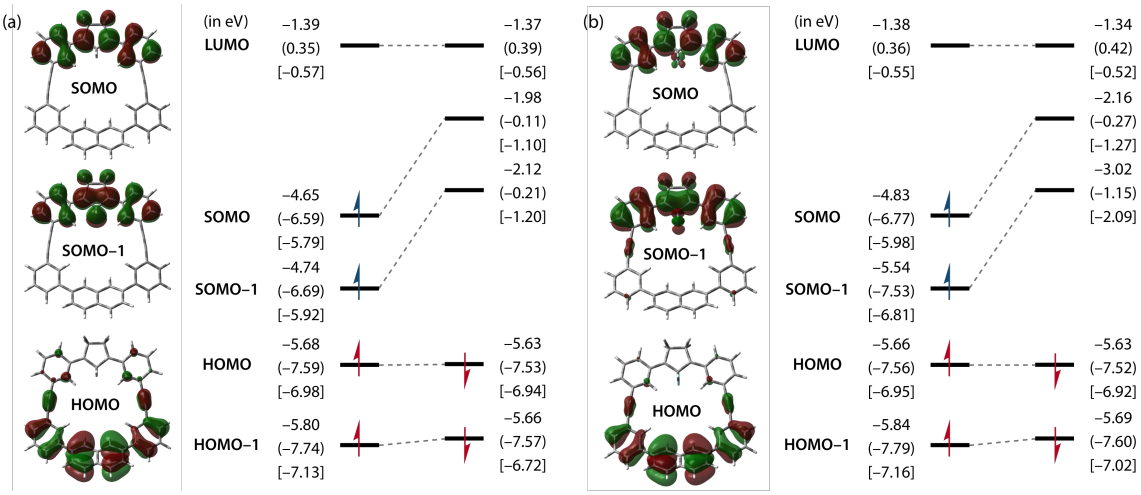

Figure 3.6 Molecular orbital diagrams of (a) **DR2H** and (b) **DR2F**. Molecular orbital energies were calculated at the unrestricted (U) B3LYP (ωB97X-D) [M06-2X] density functionals with 6-31G(d) basis set.

To confirm the through-bond interaction in **DR3X**, triplet 2,2-dihydro-cyclopentane-1,3-diyl diradical **DR3H** was computed at (U)B3LYP/6-31G(d) level of theory. The SOMO and SOMO–1 located at diradical unit, which showed similar orbital energy and distribution to those obtained in **DR2H** (Figure 3.7). As expected, **DR3H** followed Aufbau principle, and two SOMOs were higher in energy than the HOMO by 0.47 and 0.54 eV. The HOMO located at anthracyl moiety with minor extension to the adjacent phenyl rings, had no interaction with diradical unit. In the dihydro-substituted 1,3-diyls, the SOMO is destabilized by the through-bond interaction. The HOMO energy of **DR3H** increased to –5.21 eV, which was higher than the HOMO energy of **DR2H** by 0.47 eV, and even higher than the HOMO of a typical anthracene molecule (E_{HOMO} = –5.23 eV), probably due to the bent structure of anthracyl moiety in macrocyclic skeleton, the bending angle is 163.25°. Although the HOMO energy provided by anthracyl moiety was high, it was not enough to cross over the SOMO–1. Thus, SOMO–HOMO conversion was not confirmed in **DR3H**.

The triplet 2,2-difluoro-cyclopentane-1,3-diyl diradical **DR3F** showed similar molecular orbitals with **DR3H**: SOMOs at diradical unit and HOMO at anthracyl moiety (Figure 3.8). The SOMO–1 was stabilized by through-bond interaction of fluoro-substituents, which showed similar energies as those in **DR2F** (Figure 3.6b), while the HOMO is destabilized to –5.17 eV by the bent anthracyl moiety, which is higher than SOMO–1 by 0.37 eV, and

higher than the HOMO of **DR2F** by 0.45 eV. Thus, SOMO–HOMO conversion was achieved in **DR3F**.

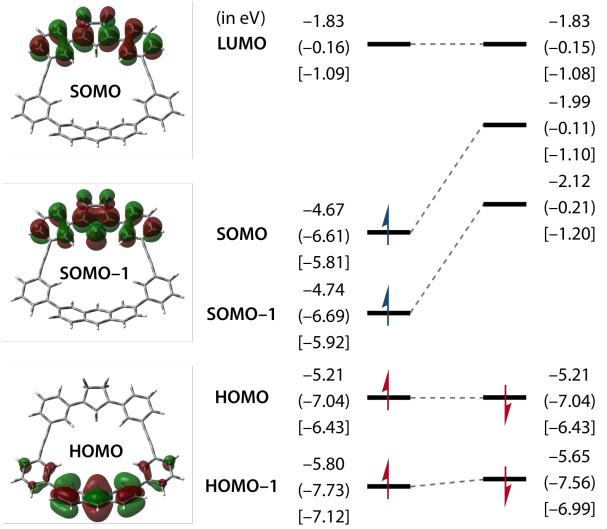

Figure 3.7 Molecular orbital diagram of **DR3H**. Molecular orbital energies were calculated at the unrestricted (U) B3LYP (ωB97X-D) [M06-2X] density functionals with 6-31G(d) basis set.

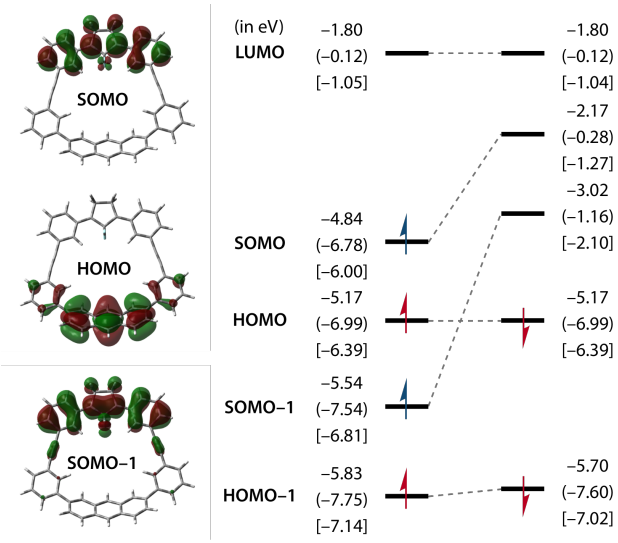

Figure 3.8 Molecular orbital diagram of **DR3F**. Molecular orbital energies were calculated at the unrestricted (U) B3LYP (ωB97X-D) [M06-2X] density functionals with 6-31G(d) basis set.

To confirm the density functional dependency on the SOMO–HOMO conversion, similar computations were conducted using different long-range correlated density functional theory (LC-DFT) functional, ωB97X-D and M06-2X with 6-31G(d) basis set. Although the absolute values for orbital

energy were different, the SOMO–HOMO conversion in **DR3F** was reproducible (Figure 3.8). The HOMO energy of **DR3F** was found to be higher than SOMO–1 by 0.37, 0.55, and 0.42 eV at the (U)B3LYP, (U)ωB97X-D, and (U)M06-2X functionals with 6-31G(d) basis set.

All computations of triplet diradicals were conducted with unrestricted (U) method, and the restricted open-shell (RO) method was also tested for the computation of the triplet state of **DR3F**. As a result, all the DOMOs were found to be lower in energy than SOMOs at (RO)B3LYP/6-31G(d) level of theory, and the total electronic energy was higher than that at (U)B3LYP/6-31G(d) level of theory by 14.2 kJ mol^{-1}.

3.2.4 Charged Species of SOMO–HOMO-Converted Triplet Diradical

The charged species (radical anion, radical cation, and dication) of SOMO–HOMO-converted **DR3F** were investigated to get a further understanding of the electronic configuration. The one-electron reduced anion **DR3F**$^{-}$, was optimized to a conventional radical anion at (U)B3LYP/6-31G+(d) level of theory. It is reported that the diffuse functions are important in predicting the properties of anionic species since the negative charge occupies the outer shell with broad orbitals. Upon one-electron reduction, the SOMO–1 of **DR3F** was doubly occupied by two electrons and became the HOMO of **DR3F**$^{-}$, while the SOMO of **DR3F** was still the SOMO of **DR3F**$^{-}$ (Figure 3.9).

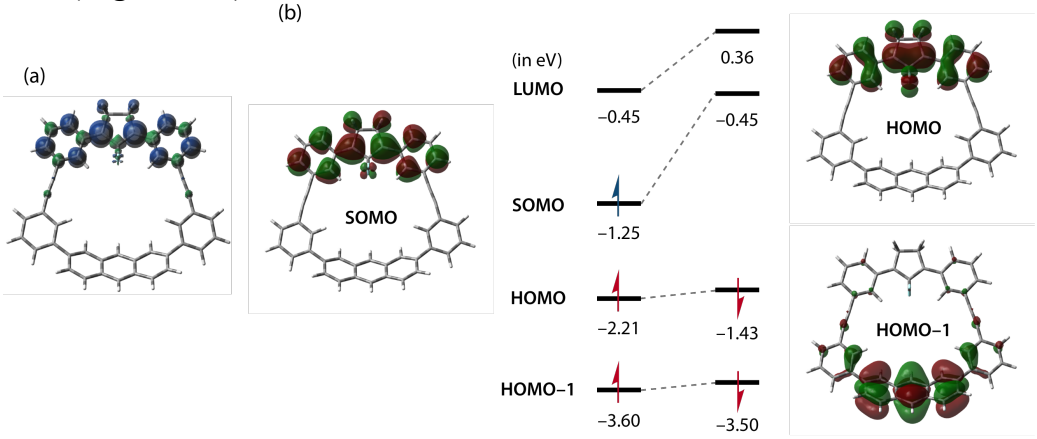

Figure 3.9 (a) Spin density map and (b) molecular orbital diagram of **DR3F**$^{-}$. Molecular orbital energies were calculated at the (U)B3LYP/6-31G+(d) level of theory.

The one-electron oxidized radical cation **DR3F**$^{+}$ was optimized to a SOMO–HOMO-converted radical cation (Figure 3.10). One electron in

SOMO of **DR3F** was removed, and the other electrons kept their original configuration, including the low-lying SOMO–1 of **DR3F**. Both diradical unit and anthracyl moiety contributed to the HOMO and LUMO. Spin density distribution of **DR3F**$^{+}$ indicated the unpaired electron localized at the diradical unit.

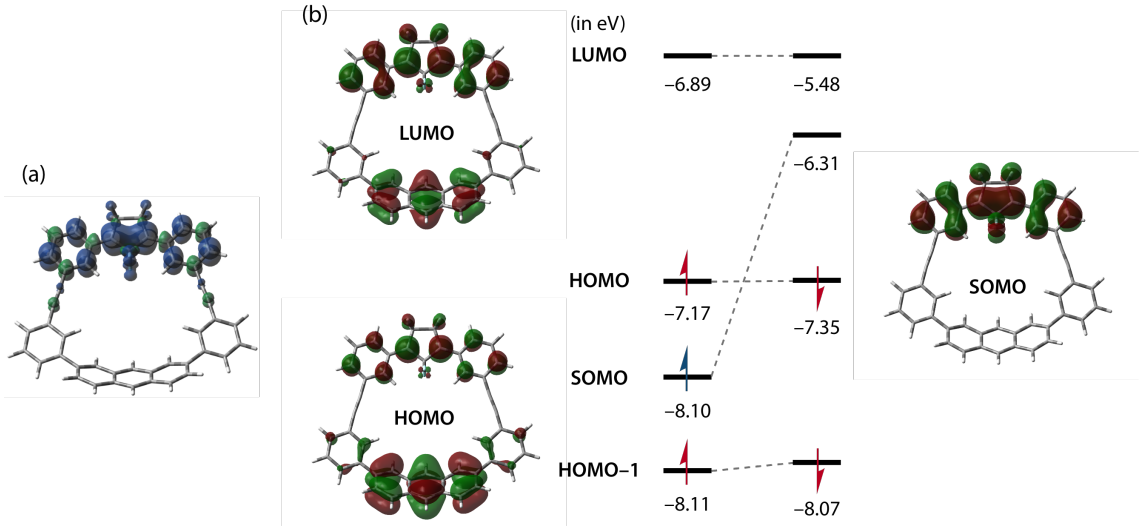

Figure 3.10 (a) Spin density map and (b) molecular orbital diagram of **DR3F**$^{+}$. Molecular orbital energies were calculated at the (U)B3LYP/6-31G(d) level of theory.

The two-electron oxidized dication, **DR3F**$^{2+}$ was found to be a triplet ground state diradical (Figure 3.11). A wavefunction instability was found in the computation at the spin-polarized open-shell singlet state with broken symmetry (BS) approach at unrestricted (U)B3LYP/6-31G(d) level of theory. In contrast, the closed-shell singlet state of **DR3F**$^{2+}$ was energetic highly liable than the triplet state (ΔE_{S-T} = 52.57 kJ mol^{-1}). The two SOMOs were located at diradical unit and anthracyl moiety separately, both of which were higher lying than the doubly occupied HOMO, which was located at the diphenylethynyl moiety. As indicated by two SOMOs, spin density map of **DR3F**$^{2+}$ clearly showed two separated parallel spins. The SOMOs in **DR3F**$^{2+}$ showed the same distribution as HOMO and SOMO–1 in **DR3F**, and the SOMO in **DR3F** became the LUMO of **DR3F**$^{2+}$.

3.2.5 SOMO–HOMO Conversion in Non-Cyclic Triplet Diradicals

HOMO energy of **DR3F** was increased to –5.17 eV, which was 0.06 eV higher than the HOMO of a typical anthracene molecule. The increased HOMO energy resulted in SOMO–HOMO conversion. As we found in

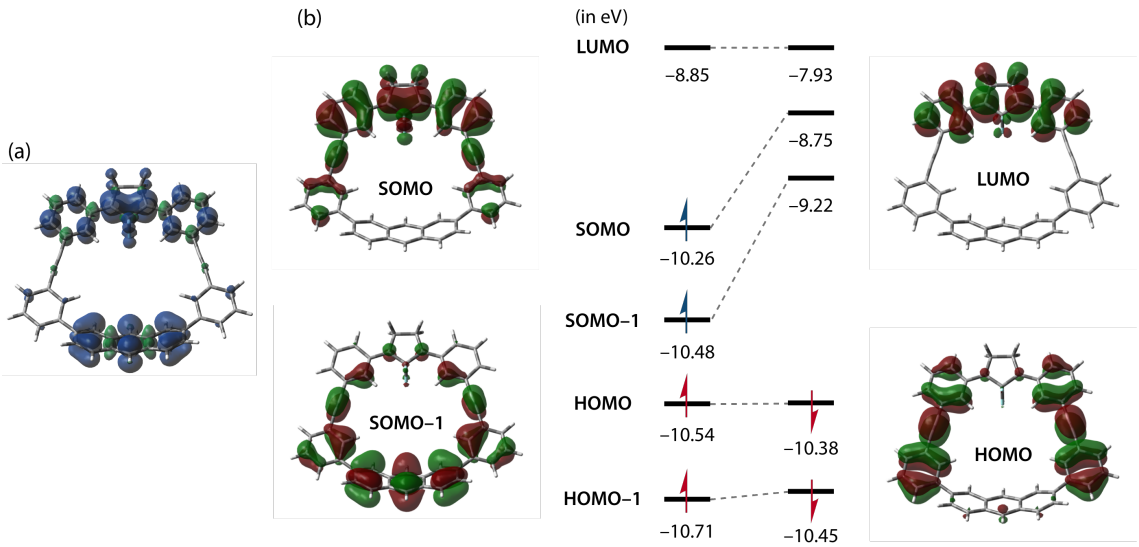

Figure 3.11 (a) Spin density map and (b) molecular orbital diagram of **DR3F**$^{2+}$. Molecular orbital energies were calculated at the (U)B3LYP/6-31G(d) level of theory.

DR3H, the anthracyl moiety was highly bent in macrocyclic skeleton, and the bending angle was 162.94° in **DR3F**. To investigate the effect of curved anthracyl moiety on SOMO–HOMO conversion, non-cyclic triplet 2,2-difluoro-cyclopentane-1,3-diyl diradical **DR4a** was computed.

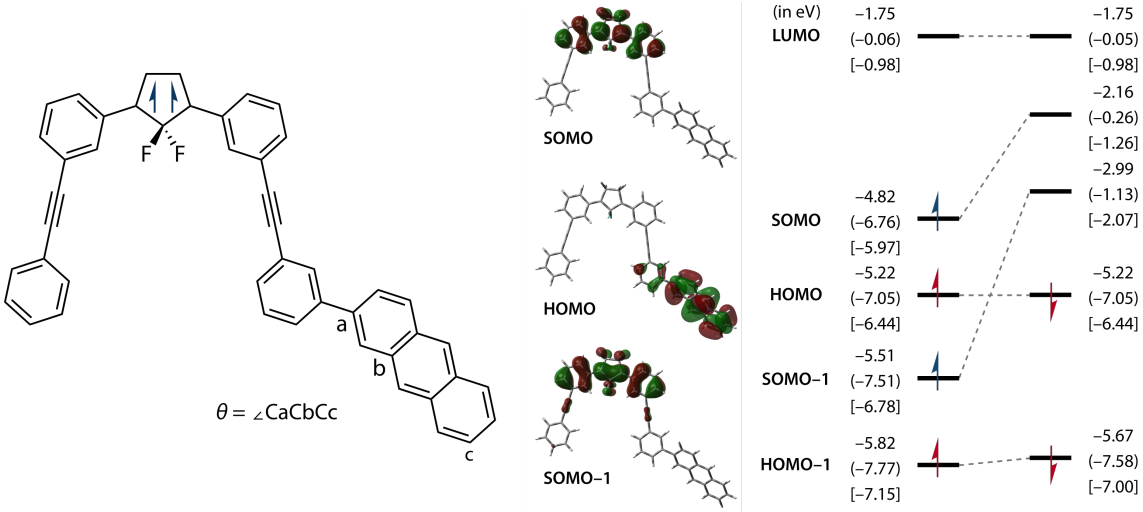

Figure 3.12 Chemical structure and molecular orbital diagram of **DR4a**. Molecular orbital energies were calculated at the unrestricted (U) B3LYP (ωB97X-D) [M06-2X] density functionals with 6-31G(d) basis set.

The anthracyl moiety in **DR4a** was nearly planar (θ = 179.78°), and the HOMO energy was very close to that of a typical anthracene molecule, indicating the HOMO was mainly located at anthracyl moiety. The SOMO–

HOMO conversion was confirmed in **DR4a** since the HOMO energy was lower than SOMO by 0.40 eV but higher than SOMO–1 by 0.29 eV (Figure 3.12). Thus, the HOMO energy of anthracene is high enough to cross over the SOMO–1 of triplet 2,2-difluoro-cyclopentane-1,3-diyl diradicals, although the curved anthracyl did increase the HOMO energy in **DR3F**.

Since the triple bonds in **DR3F** did not contribute to the SOMOs and HOMO, they should have no influence on the SOMO–HOMO conversion. Triplet diradical **DR4b** was computed to prove our prediction. As expected, SOMO–HOMO conversion was confirmed in **DR4b**, and the HOMO energy was 0.22 eV higher than that of SOMO–1 (Figure 3.13). The anthracyl moiety adapted a planar structure, similar to that in **DR4a**.

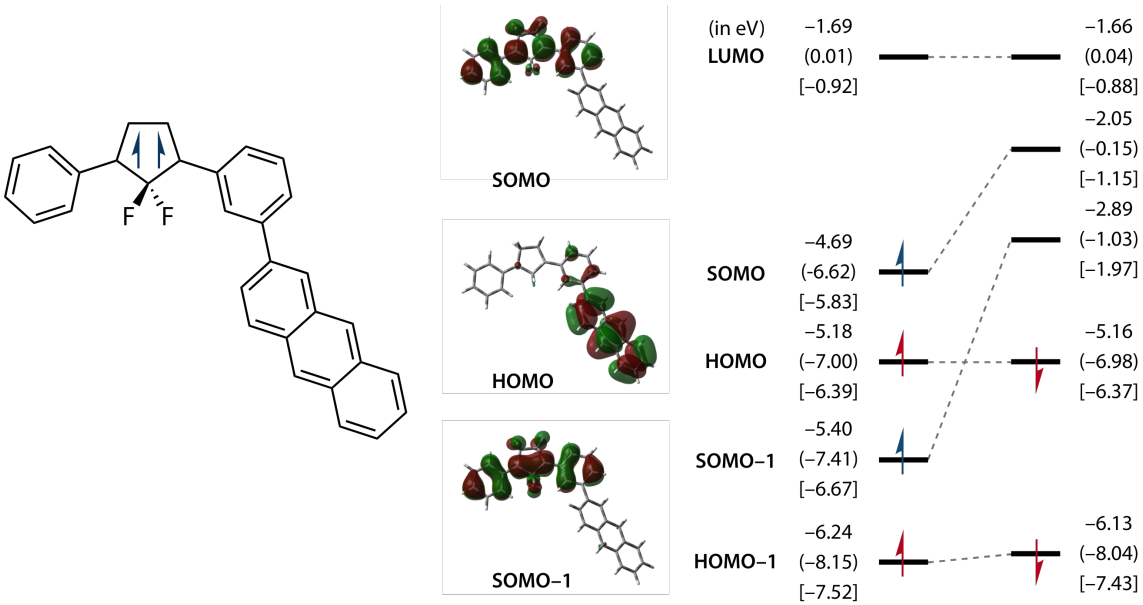

Figure 3.13 Chemical structure and molecular orbital diagram of **DR4b**. Molecular orbital energies were calculated at the unrestricted (U) B3LYP (ωB97X-D) [M06-2X] density functionals with 6-31G(d) basis set.

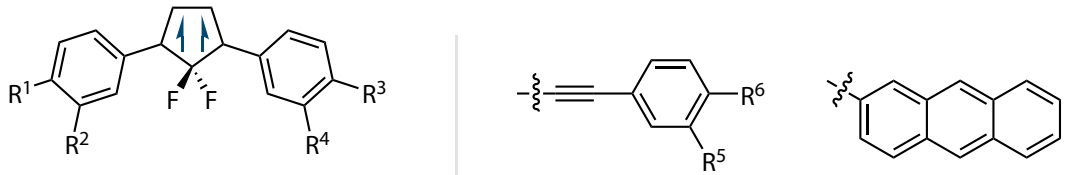

DR5a: $R^1 = R^3 = H$, $R^2 = Ar^1$, $R^4 = Ar^3$
DR5b: $R^2 = R^4 = H$, $R^1 = Ar^1$, $R^3 = Ar^2$
DR5c: $R^1 = R^2 = R^4 = H$, $R^3 = Ant$

Ar^1 ($R^5 = H$, $R^6 = H$)
Ar^2 ($R^5 = Ant$, $R^6 = H$)
Ar^3 ($R^5 = H$, $R^6 = Ant$)

Scheme 3.3 Chemical structures of **DR5a**–**c**.

The linkage type that decouples the π-conjugation between diradical unit and anthracyl moiety should influence the SOMO–HOMO conversion. To understand the effect of *meta*-linkage, triplet diradicals **DR5a**–**c** were computed at (U)B3LYP/6-31G(d) level of theory (Scheme 3.3).

For **DR5a**, the anthracyl moiety was connected at the *para*-position of the phenyl ring. The HOMO was confirmed in the phenylanthracyl moiety, with small delocalization to the triple bond, so the HOMO energy slightly increased compared with that of **DR4a** by 0.03 eV (Figure 3.14). On the other hand, changing of linkage pattern did not affect the SOMO and SOMO–1 distribution, and SOMO–HOMO conversion was observed in **DR5a**.

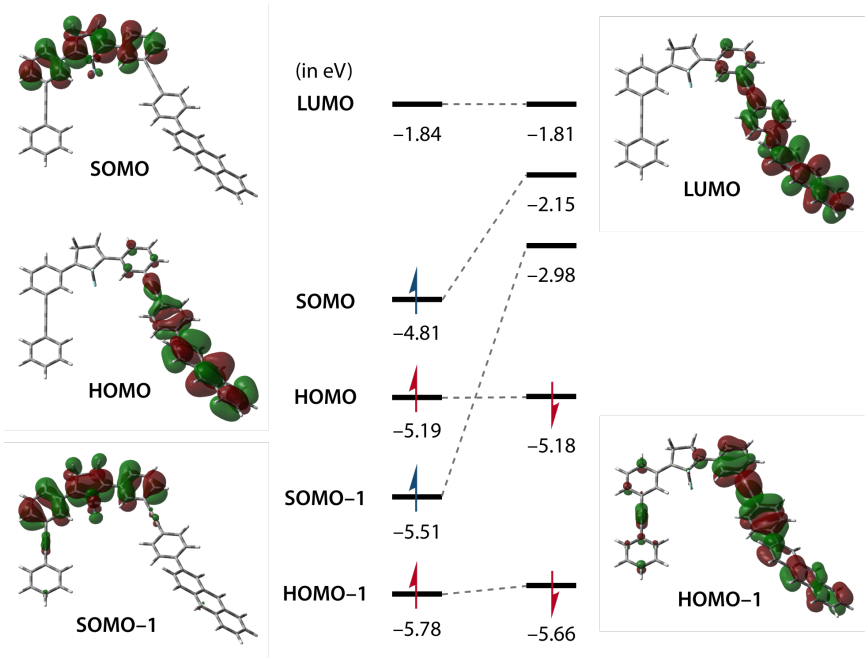

Figure 3.14 Molecular orbital diagram of **DR5a**. Molecular orbital energies were calculated at the (U)B3LYP/6-31G(d) level of theory.

In **DR5b**, the 2-(3-anthracylphenyl)-ethynyl unit is connected with 1,3-diphenyl rings at the *para*-position. The SOMO and SOMO–1 were highly destabilized by 0.22 and 0.40 eV, respectively, compared with those in **DR5a** (Figure 3.15). The destabilization is due to the increased π-conjugation to the ethynylphenyl unit. On the other hand, the HOMO was not changed compared with the typical anthracene molecule. Thus, the HOMO energy was lower than SOMO–1 by 0.14 eV, and **DR5b** adapted a conventional electronic configuration.

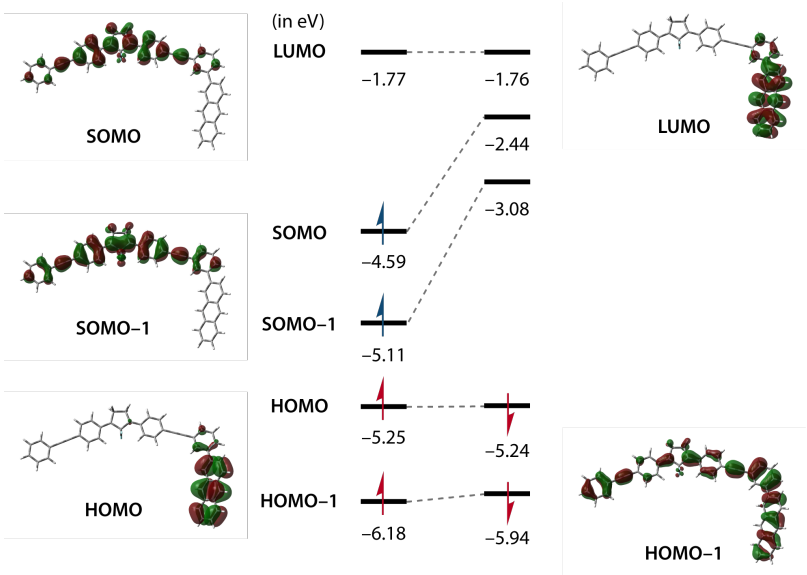

Figure 3.15 Molecular orbital diagram of **DR5b**. Molecular orbital energies were calculated at the (U)B3LYP/6-31G(d) level of theory.

A similar conclusion was confirmed in **DR5c** by removing the triple bonds in **DR5b**, in which the anthracyl moiety was directly connected at the *para*-position of 1,3-diphenyl rings. As the discussion about **DR4b**, the triple bonds had no influence on the SOMOs and HOMO. Thus, **DR5c** showed the same behavior as **DR5b**. The electronic configuration followed Aufbau principle (Figure 3.16).

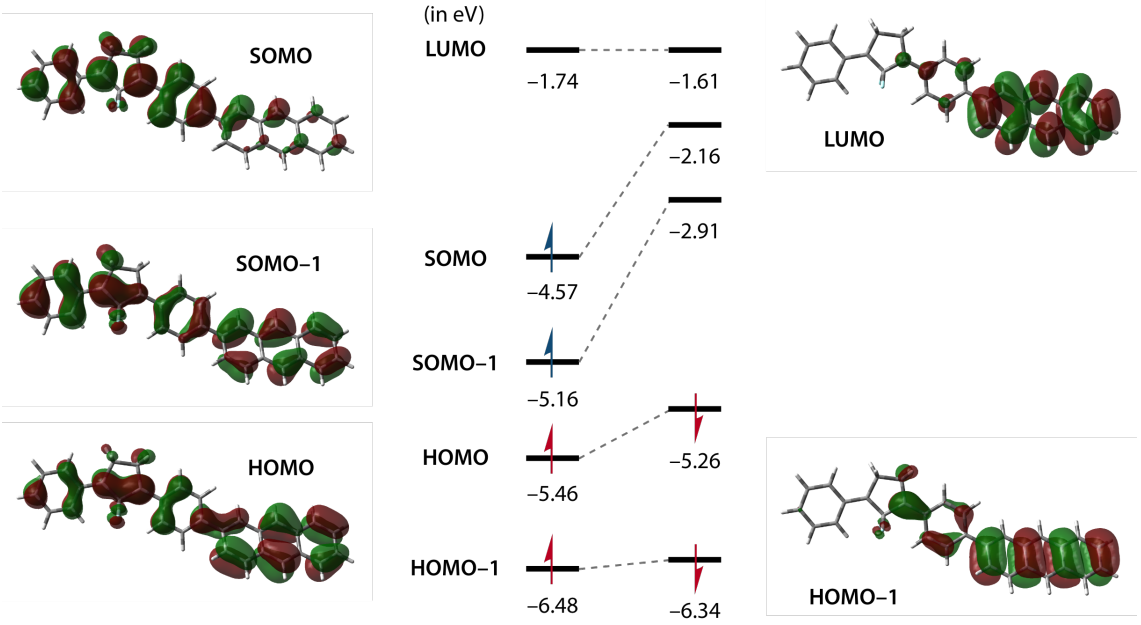

Figure 3.16 Molecular orbital diagram of **DR5c**. Molecular orbital energies were calculated at the (U)B3LYP/6-31G(d) level of theory.

The SOMO–HOMO-converted triplet diradicals discussed above have fluoro-substituents on the C2 position of cyclopentane ring. As we introduced in chapter 2, these type-I diradicals have singlet ground states, and the SOMO–HOMO conversion which observed by computational studies exists in their excited triplet states. Electron donating groups like hydrogen atom, alkyl groups at the C2 position are necessary for making triplet ground state diradicals. In that case, to achieve SOMO–HOMO conversion, we need to increase the HOMO energy higher than that of ψ_{TS}^{-} (E = –4.60 eV). Thus, triplet diradical **DR6** with hexacyl moiety (n = 6) at remote position were computed (Figure 3.17). The HOMO energy of hexacyl moiety increased to –4.41 eV, which was higher than SOMO and SOMO–1 by 0.09 and 0.20 eV, respectively. As expected, the diradical **DR6** has a triplet ground state (ΔE_{S-T} = 0.98 kJ mol^{-1}) due to the through-bond interaction by hydrogen atoms at the C2 position of cyclopentane ring.

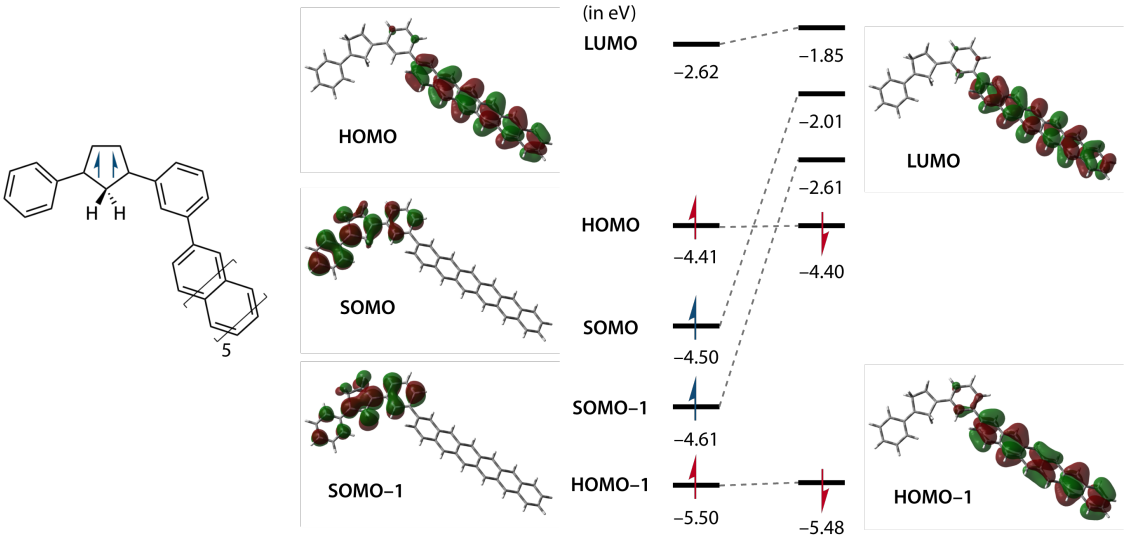

Figure 3.17 Chemical structure and molecular orbital diagram of **DR6**. Molecular orbital energies were calculated at the (U)B3LYP/6-31G(d) level of theory.

3.3 Chapter Summary

In this chapter, we provided an approach for the molecular design of SOMO–HOMO-converted triplet cyclopentane-1,3-diyl diradicals. Two factors were important for generating such non-Aufbau configured species: (1) decreasing the SOMO–1 energy by introducing difluoro-substituents at the C2 position; (2) increasing HOMO energy by introducing acene with high HOMO energy at remote position.

According to computations, singlet ground state diradicals **DR** displayed SOMO–HOMO conversion in their triplet excited states, with high HOMO energy in the anthracyl moiety and low-lying SOMO–1 due to stabilization through-bond interaction of fluoro-substituents. Such SOMO–HOMO-converted triplet diradicals showed different behavior on the charged species compared with conventional triplet diradicals: the one-electron oxidized cation, **DR3F**$^{+}$, also displayed SOMO–HOMO conversion, while the two-electron oxidized dication **DR3F**$^{2+}$ and one-electron reduced anion **DR3F**$^{-}$ followed Aufbau principle.

On the other hand, the dihydro- or naphthyl-substituted **DR** did not show SOMO–HOMO conversion due to the lower HOMO energies and/or higher SOMO–1 energies. SOMO–HOMO conversion vanished in *para*-linked derivatives **DR5b** and **DR5c** resulting from alteration in the conjugation pattern.

The triplet ground state diradicals **DR6** with higher HOMO energies by introducing hexacyl moieties were investigated. Although the through-bond interaction did not stabilize the SOMO–1 in **DR6**, the high-lying HOMO provided SOMO–HOMO conversion in its triplet ground state. The computational studies described in this chapter aim to provide a new method for creating carbon-based SOMO–HOMO-converted triplet diradicals.

3.4 Computational Details

Quantum chemical computations in gas phase have been performed with the *Gaussian 16* (Revision B.01) suite of programs. Molecular orbitals and spin density maps were visualized with an iso-surface value of 0.02 and 0.0015 a.u., respectively, using *GaussView 6.0.16* program.

The overlap integral $\boldsymbol{S}$ between α and β orbitals is used to evaluate the matching degree of corresponding spin orbital pairs, significant deviation from 1 indicates remarkable spin polarization. The overlap integral matrixes were computed with equation (S1) by Multiwfn 3.7 package[10] on Red Hat Enterprise Linux 8.3 platform.

$$S_{i,j}^{\alpha\beta} = \int \varphi_i^{\alpha}(\mathbf{r})\varphi_{\mathrm{j}}^{\beta}(\mathbf{r})\mathrm{d}\mathbf{r} \qquad \text{(S1)}$$

3.5 References

1 M. Gomberg, An instance of trivalent carbon: triphenylmethyl, *J. Am. Chem. Soc.*, **1900**, *22*, 757–771.

2 R. Murata, Z. Wang and M. Abe, Singly occupied molecular orbital–highest occupied molecular orbital (SOMO–HOMO) conversion, *Aust. J. Chem.*, **2021**, *74*, 827–837.

3 T. Sugimoto, S. Yamaga, M. Nakai, K. Ohmori, M. Tsujii, H. Nakatsuji, H. Fujita and J. Yamauchi, Intramolecular spin-spin exchange in cation radicals of tetrathiafulvalene derivatives substituted with imino pyrolidine- and piperidine-1-oxyls, *Chem. Lett.*, **1993**, *22*, 1361–1364.

4 T. Kusamoto, S. Kume and H. Nishihara, Realization of SOMO–HOMO level conversion for a tempo-dithiolate ligand by coordination to platinum(II), *J. Am. Chem. Soc.*, **2008**, *130*, 13844–13845.

5 G. Gryn'ova, D. L. Marshall, S. J. Blanksby and M. L. Coote, Switching radical stability by pH-induced orbital conversion, *Nat. Chem*., **2013**, *5*, 474–481.

6 Y. Wang, H. Zhang, M. Pink, A. Olankitwanit, S. Rajca and A. Rajca, Radical cation and neutral radical of aza-thia[7]helicene with SOMO–HOMO energy level inversion, *J. Am. Chem. Soc*., **2016**, *138*, 7298–7304.

7 S. Kasemthaveechok, L. Abella, M. Jean, M. Cordier, T. Roisnel, N. Vanthuyne, T. Guizouarn, O. Cador, J. Autschbach, J. Crassous and L. Favereau, Axially and helically chiral cationic radical bicarbazoles: SOMO–HOMO level inversion and chirality impact on the stability of mono- and diradical cations, *J. Am. Chem. Soc.*, **2020**, *142*, 20409–20418.

8 R. Murata, Z. Wang, Y. Miyazawa, I. Antol, S. Yamago and M. Abe, SOMO–HOMO conversion in triplet carbenes, *Org. Lett.*, **2021**, *23*, 4955–4959.

9 D. E. Woon and T. H. Dunning, Gaussian basis sets for use in correlated molecular calculations. III. The atoms aluminum through argon, *J. Chem. Phys.*, **1993**, *98*, 1358–1371.

10 T. Lu and F. Chen, Multiwfn: A multifunctional wavefunction

analyzer, *J. Comput. Chem.*, **2012**, *33*, 580–592. The program was directly download from Multiwfn homepage (http://sobereva.com/multiwfn/).

Chapter 4.

Summary and Outlook

Localized diradicals having two unpaired electrons are well-known chemical species in the denitrogenation of azoalkanes or bond homolysis reactions. Diradicals have two spin states, a singlet and a triplet. Due to the two electrons are ferromagnetically coupled, triplet diradicals show great potential for application to molecular magnetic materials. On the other hand, singlet diradicals are critical intermediates in the bond homolysis processes. Thus, elucidating their chemistry will provide a deeper understanding of the fundamental processes of bond-formation and bond-breaking processes. Recently, the non-linear optical properties and singlet-fission phenomenon were found in open-shell singlet species. So, singlet diradicals have attracted attention not only in fundamental chemical research but also in the field of materials science.

Singlet cyclopentane-1,3-diyl diradicaloids with bonding orbital in the highest occupied molecular orbital (HOMO) are promising candidates for carbon–carbon π-single bonding species. Such species possess an extremely small HOMO–LUMO gap, showing unique chemical properties such as high redox activity and non-linear optical properties. Generally, the localized singlet diradicaloids having π-single bonding character are highly reactive species that give the corresponding σ-bonding compounds. The short-lived character hampers experimental investigations of their nature. In the past two decades, continued efforts have been devoted to stabilizing such highly reactive species. By introducing phenyl rings to the radical carbon atoms, singlet diradicaloids could be thermodynamically stabilized by electron delocalization. On the other hand, the kinetic stabilization of singlet diradicaloids has been achieved by introducing bulky groups to destabilize the transition states and products of intramolecular radical–radical coupling reactions.

In chapter 2, we implemented the approach of “stretch effect” for cyclopentane-1,3-diyl diradicaloids to access kinetically stabilized singlet diradicaloids. The stretch effect induced by macrocyclic skeleton can suppress the bond-formation process by pulling the two radical carbon atoms into the opposite direction against the bond-formation. Thus, the transition states **TS** and σ-bonded products **CP** are supposed to be destabilized, and singlet diradicaloid S-**DR** could be kinetically stabilized. To this end, a macrocyclic structure was designed to generate the long-lived singlet diradicaloid, enabling the experimental investigation of the singlet

diradicaloid with π-single bonding character.

Quantum chemical computations were conducted for the molecular design of long-lived singlet diradicaloid with "stretch effect". The kinetically stabilized diradicaloid S-**DR2d** was generated by the photochemical denitrogenation of azoalkane **AZ2d** to exhibit a small carbon–carbon coupling reaction rate of 6.4×10^3 s^{-1} (155.9 μs), approximately 1000 times slower than that of the parent system without the macrocycle S-**DR1** (5×10^6 s^{-1}, 209 ns) at 293 K in benzene. In addition, a significant dynamic solvent effect was observed in the intramolecular radical–radical coupling reactions. The lifetime of singlet diradicaloid S-**DR2d** showed the longest lifetime up to 400.2 μs in viscous glycerin triacetate (η = 23.00 cP) at 293 K. Furthermore, the stretch effect highly destabilized the σ-bonded product *trans*-**CP2**, it decomposed immediately after exposure to air atmosphere, although the σ-bonded product with no-macrocyclic structure *trans*-**CP1** was stable under air at room temperature. The theoretical and experimental studies demonstrated that the stretch effect and solvent viscosity play important roles in retarding the σ-bond formation process, thus enabling a thorough examination of the nature of the singlet diradical and paving the way toward a deeper understanding of reactive intermediates.

The research results in chapter 2 encourage further experiments on S-**DR2d**. Since the solvent viscosity strongly affects the lifetime of S-**DR2d**, it is expected that S-**DR2d** may have a longer lifetime in the solvent with higher viscosity, such as ionic liquids. And, it is considered that the atomic movement of S-**DR2d** could be inhibited in the solid state, so it is worth to check the lifetime of S-**DR2d** in solid polymer like PMMA. Furthermore, the molecular design of longer-lived singlet diradicaloids than S-**DR2d** is important to create π-single bonded species since the lifetime of S-**DR2d** is still in microsecond order.

In chapter 3, we focused on the triplet diradicals. According to the Aufbau principle, singly occupied molecular orbitals (SOMOs) are energetically higher lying than the highest doubly occupied molecular orbital (HOMO) in the electronic ground state of radicals. However, in the last decade, SOMO–HOMO energy-converted species have been reported in a limited group of radicals, such as distonic anion radicals and nitroxides. This unusual electronic configuration plays an important role in switch bond dissociation energy, generation of high-spin species in the low oxidation state,

and light emission in the near-infrared region.

The singlet cyclopentane-1,3-diyl diradicaloids were discussed in chapter 2, the HOMO and SOMOs of these diradicaloids located at separated positions. Thus, it is possible to generate SOMO–HOMO-converted diradicals by increasing HOMO energy and/or decreasing SOMO/SOMO–1 energies. In this study, SOMO–HOMO conversion was found in triplet 2,2-difluorocyclopentane-1,3-diyl diradical **DR3F** by theoretical computations containing the anthracyl unit at the remote position. The SOMO–HOMO conversion vanished in dihydro-substituted **DR3H** or naphthyl-substituted **DR2F** triplet diradicals, indicating that the high HOMO energy in the anthracyl moiety and the low-lying SOMO–1 due to the fluoro-substituent effect were the keys to the SOMO–HOMO conversion phenomenon. Furthermore, the cation radical which was generated through the one-electron oxidation of neutral diradical was found to be a SOMO–HOMO-converted monoradical, and the dication was a diradical with triplet ground state according to computations. These theoretical studies provided an approach for the molecular design of SOMO–HOMO-converted species. The exciting computational results about SOMO–HOMO-converted triplet diradical **DR6** request further experimental research.

Acknowledgment

The research studies discussed in this dissertation have been carried out under the direction of Prof. Dr. Manabu Abe at the Research Group of Reaction Organic Chemistry, Department of Chemistry, Graduate School of Science, Hiroshima University, from October 2017 to September 2022.

I am deeply indebted to my supervisor Prof. Dr. Manabu Abe, who made this work possible. His guidance, advice, and support not only on the research study but also in my daily life carried me through these years. Also, as an international student, I would like to express my appreciation to Prof. Dr. Manabu Abe for accepting me to join his laboratory, although I had no experience in organic chemistry before I came to Japan.

I am also thankful to Dr. Sayaka Hatano and Dr. Ryukichi Takagi from the Research Group of Reaction Organic Chemistry for their valuable discussions and continuous support to this research.

Many thanks to Mr. Yuta Harada, who helped me finished the necessary procedure for living in Japan and taught me the basics of organic synthesis. I could not finish my first column chromatography without his help.

I would like to extend my sincere thanks to all the members of the Research Group of Reaction Organic Chemistry. Special thanks to Dr. Jianfei Xue, Dr. Shohei Yoshidomi, Dr. Rikuo Akisaka, Mr. Norito Kadowaki, Mr. Ayato Yamada, Mr. Hai Dang Nguyen, Ms. Ryoko Oyama, Ms. Chika Yoshidomi (Tanabe), Ms. Aina Miyahara, Mr. Miyu Sasaki, Mr. Yuki Miyazawa, Ms. Ma-aya Takano, Mr. Kazunori Okamoto, Mr. Masaya Matsui, Mr. Kentaro Sugikawa, Mr. Ryo Murata, Mr. Takuma Miyamura, Ms. Yui Okihara, Ms. Ayaka Itasaka, Mr. Ryuei Hayashi, for their support of my daily life in these years.

Thanks should also go to Dr. Tatsuo Nakagawa and Dr. Sohshi Yabumoto from UNISOKU Co., Ltd. for providing sub-nanosecond transient absorption measurements.

I would like to acknowledge the valuable support offered by Mrs. Tomoko Amimoto from Natural Science Center for Basic Research and Development (N-BARD), Hiroshima University, for providing high-resolution mass spectrometer measurements.

My mother, Mrs. Wei Zhang, has always been supporting my life over these years and encouraged me to be a better person.

Lastly, I am grateful to the ages, for the joys and sorrows in the world, and its tolerance.

Nothing but enthusiasm brightens up the endless years.

Zhe WANG
Research group of Reaction Organic Chemistry,
Department of Chemistry,
Graduate School of Science,
Hiroshima University,
Higashi-hiroshima, Japan.
September 2022

公表論文

Impact of the macrocyclic structure and dynamic solvent effect on the reactivity of a localised singlet diradicaloid with π-single bonding character.

Zhe Wang, Rikuo Akisaka, Sohshi Yabumoto, Tatsuo Nakagawa, Sayaka Hatano and Manabu Abe.

Chem. Sci., **2021**, 12(2), 613–625.

DOI: 10.1039/d0sc05311b

SOMO–HOMO Conversion in Triplet Cyclopentane-1,3-diyl Diradicals.

Zhe Wang, Ryo Murata and Manabu Abe.

ACS Omega, **2021**, 6(35), 22773–22779.

DOI: 10.1021/acsomega.1c03125

参考論文

Extremely Long Lived Localized Singlet Diradicals in a Macrocyclic Structure: A Case Study on the Stretch Effect.

Yuta Harada, Zhe Wang, Shunsuke Kumashiro, Sayaka Hatano and Manabu Abe.

Chem. Eur. J., **2018**, 24(55), 14808–14815.

DOI: 10.1002/chem.201803076

1,3-Diradicals Embedded in Curved Paraphenylene Units: Singlet versus Triplet State and In-plane Aromaticity.

Yuki Miyazawa, Zhe Wang, Misaki Matsumoto, Sayaka Hatano, Ivana Antol, Eiichi Kayahara, Shigeru Yamago and Manabu Abe.

J. Am. Chem. Soc., **2021**, 143(19), 7426–7439.

DOI: 10.1021/jacs.1c01329

SOMO–HOMO Conversion in Triplet Carbenes.

Ryo Murata, Zhe Wang, Yuki Miyazawa, Ivana Antol, Shigeru Yamago and Manabu Abe.

Org. Lett., **2021**, 23(13), 4955–4959.

DOI: 10.1021/acs.orglett.1c01137

Long-lived localised singlet diradicaloids with carbon–carbon π-single bonding (C–π–C).

Zhe Wang, Pinky Yadav and Manabu Abe.

Chem. Commun., **2021**, 57(86), 11301–11309.

DOI: 10.1039/d1cc04581d

Singly Occupied Molecular Orbital–Highest Occupied Molecular Orbital (SOMO–HOMO) Conversion.

Ryo Murata, Zhe Wang and Manabu Abe.

Aust. J. Chem., **2021**, 74(12), 827–837.

DOI: 10.1071/ch21186

New Insights into Bond Homolysis Process and Discovery of Novel Bonding System (C–π–C) by Generating Long-lived Singlet Diradicals.

Manabu Abe, Zhe Wang and Rikuo Akisaka.

AsiaChem, **2021**, 2(1), 32–41.

DOI: 10.51167/acm00020.51167/acm00021

Impacts of Solvent and Alkyl Chain Length on the Lifetime of Singlet Cyclopentane-1,3-diyl Diradicaloids with π-Single Bonding.

Qian Liu, Zhe Wang and Manabu Abe.

J. Org. Chem., **2022**, 87(3), 1858–1866.

DOI: 10.1021/acs.joc.1c02895